Synthesis and application of CeO_2 nanoparticles as catalyst for oxidative bromination

Dissertation

zur Erlangung des akademischen Grades
„Doktor der Naturwissenschaften“
im Promotionsfach Chemie

am Fachbereich Chemie, Pharmazie, Geographie und Geowissenschaften der
Johannes Gutenberg-Universität in Mainz

Olga Jegel geb. Beilmann
geboren in Nishnij Tagil
Mainz, 2022

Dekan: XXX

1.Berichterstatter: XXX

2.Berichterstatter: XXX

Prüfungsvorsitz: XXX

Datum der mündlichen Prüfung: _____

Declaration

The presented dissertation was prepared between Januar 2019 and Dezember 2021 under the direction of XXX at the department of chemistry of the Johannes Gutenberg-University Mainz.

I hereby declare that I, Olga Jegel, wrote the presented dissertation independently and without outside help. All used references and resources are completely indicated.

Erklärung

Die vorliegende Arbeit wurde in der Zeit Januar 2019 bis Dezember 2021 unter der Betreuung von XXX am Department Chemie der Johannes Gutenberg-Universität durchgeführt.

Hiermit erkläre ich, Olga Jegel, dass die vorliegende Arbeit selbstständig verfasst und keine anderen als die angegeben Quellen und Hilfsmittel verwendet wurden. Alle Ausführungen, die wörtlich oder sinngemäß aus anderen Quellen übernommen wurden, sind als solche gekennzeichnet.

Mainz, _____ _____

(Ort, Datum) (Unterschrift)

Für meine Familie

„Laufe nicht der Vergangenheit nach und
verliere dich nicht in der Zukunft.
Die Vergangenheit ist nicht mehr.
Die Zukunft ist noch nicht gekommen.
Das Leben ist hier und jetzt.“

Buddha

I. Acknowledgements

First of all, I would like to thank my supervisor **XXX**, for his support and helpful discussions on difficult issues during my time in his working group.

My sincere thanks goes to **XXX** for his cooperation and help at the beginning of my PhD.

I would like to thank **XXX**, **XXX**, **XXX** and **XXX**, who were also part of the catalysis sub-working group and for all the helpful discussions we had over the last years.

Especially I thank **XXX**, **XXX** and **XXX** for the great and uncomplicated cooperation on common projects.

I express my graduate to **XXX**, **XXX**, **XXX** and **XXX** for measuring of PXRDs.

Thanks to **XXX** for measuring my NMR experiments and the helpful discussion of the results.

Of course, I would also like to thank all my cooperation partners, especially **XXX** for performing bioassays**,** and **XXX** for examining the biofilms using AFM. Without your professional support all this would not have been possible!

A special thank goes to **XXX** for managing everything. You can always be counted on!

Great appreciation to our **"Durak crew"** with its establishment of "Durak of the month" has gained even more importance. From that point on, the game was no longer just about having fun!

Many thanks to **XXX** and her group, who were successfully integrated into our "Durak crew".

I express my gratitude to **XXX**, **XXX**, **XXX**, **XXX**, **XXX** and **XXX**, who had an open ear not only for scientific but also for private conversations.

I thank **XXX**, **XXX**, **XXX**, **XXX**, **XXX**, **XXX** and **XXX** for the friendly working atmosphere. I enjoyed being part of this wonderful group!

Finally, I am most grateful for my parents **XXX** and **XXX**, and of course, for my husband **XXX**, who supported me for 9 years during all my studies. Also a thank goes to my friends, who also gave me other thoughts besides chemistry.

II. List of Publications

Olga Jegel, XXX, XXX, XXX, XXX, XXX, XXX, XXX, XXX ,XXX and XXX, Morphology regulated oxidative bromination of thymol with CeO_{2-x} nanocrystal enzyme mimics, 2022, in preparation

XXX, XXX, XXX, XXX, **Olga Jegel**, XXX, XXX, XXX, XXX, XXX, XXX, Generalized synthesis of $NaCrO_2$ particles for high-rate sodium ion batteries prepared by microfluidic synthesis in segmented flow, *Dalton Transactions*, submitted

XXX, **Olga Jegel**, XXX, XXX, XXX, XXX, XXX, XXX, XXX, XXX, XXX, XXX, XXX, XXX and XXX, Large-Scale Synthesis of CeO2 Nanoparticles by Automated Segmented Flow for Nanocomposites Repelling Pseudomonas Aeruginosa PA14 Biofilms, 2022, in preparation

XXX, **Olga Jegel**, XXX, XXX, XXX, XXX, XXX, XXX, *Nanoscale*, 2021, submitted

Olga Jegel, XXX, XXX, XXX, XXX, XXX, XXX, XXX, XXX, XXX, XXX, XXX, Transparent Polycarbonate Coated with CeO_2 Nanozymes Repel Pseudomonas aeruginosa PA14 Biofilms, *Nanoscale*, 2022, 14, 86-98. (DOI: doi.org/10.1039/D1NR03320D)

III. Abstract

In recent years, the so-called "nanozymes" have come to the forefront of research. These are nanomaterials that have the property of mimicking enzymes. In this dissertation, ceria nanoparticles are presented as such an enzyme mimic. Cerium oxide can mimic the enzyme vanadium bromoperoxidase in the presence of bromide and hydrogen peroxide by oxidative bromination. In this work, various syntheses of ceria nanoparticles and their potential applications are discussed. In addition, oxidative bromination with CeO_2 as catalyst and the factors that promote it are examined in more detail.

In the first chapter, it was investigated if doping with the lanthanides praseodymium and terbium can increase the catalytic activity of the ceria nanoparticles. For this purpose, a mechanochemical synthesis was established in a planetary ball mill by a simple metathesis reaction. Thereby the catalytic activity could be increased almost twofold by doping and was found to be dependent on various factors such as zeta-potential and specific BET surface area. Likewise, Raman and ESR spectroscopy demonstrated that the incorporation of the trivalent cation creates oxygen vacancies, which also have an important effect on the catalysis rate.

Another project consisted of analyzing different morphologies of ceria nanoparticles for their catalytic activity. For this purpose, oxidative bromination was carried out and evaluated based on the bromination of thymol using NMR spectroscopy. This showed a clear difference between the different morphologies with respect to catalytic activity. Here, as well, it was demonstrated that influences such as zeta potential and specific BET surface area have an important effect on catalysis. In addition, Raman spectroscopy showed that the ceria nanoparticles with the different morphologies degraded the substrate hydrogen peroxide after a short time on the particle surface, which significantly slowed down the catalysis.

Furthermore, as an application, polycarbonate plates were coated with functionalized CeO_2 nanoparticles. For better adhesion of the particles, a polar surface was created with the help of oxygen plasma. A homogeneous coating of functionalized ceria nanoparticles was used to create a nanozyme. The task of the nanozyme is to brominate signal molecules of bacteria using oxidative halogenation to inhibit biofilm growth. As a result, the altered signal molecules are no longer recognized by the bacteria, the communication is interrupted, and

the biofilm growth is stops. Subsequent bioassays with the Gram-negative bacterium *Pseudomonas aeruginosa* showed an inhibition of 75% of the biofilm growth after polycarbonate coating with CeO_2 nanoparticles in contrast to pristine polycarbonate plates.

IV. Zusammenfassung

In den letzten Jahren sind sogenannte „nanozymes“ in den Vordergrund der Forschung gerückt. Dabei handelt es sich um Nanomaterialien, welche die Eigenschaft besitzen, Enzyme nachzuahmen. In der vorliegenden Dissertation werden Ceroxid-Nanopartikel als solches Enzymmimetikum vorgestellt. Ceroxid ist in der Lage, in Anwesenheit von Bromid und Wasserstoffperoxid, durch oxidative Bromierung das Enzym Vanadium-Bromoperoxidase nachzuahmen. In der Arbeit wird auf unterschiedliche Synthesen von Ceroxid-Nanopartikel und ihre möglichen Anwendungen eingegangen. Zusätzlich wird die oxidativen Bromierung genauer untersucht und welche Faktoren diese begünstigen.

Zum anderen wurde untersucht, ob durch eine Dotierung mit den Lanthanoiden Praseodym und Terbium die katalytische Aktivität erhöht werden kann. Dafür wurde durch eine einfache Metathesereaktion, eine mechanochemische Synthese in einer Planetenkugelmühle etabliert. Die katalytische Aktivität konnte durch die Dotierung um fast das Doppelte erhöht werden. Es wurde festgestellt, dass die katalytische Aktivität von Faktoren wie Zeta-Potential und der BET-Oberfläche abhängig ist. Ebenfalls konnte mittels Raman- und ESR-Spektroskopie nachgewiesen werden, dass durch den Einbau des dreiwertigen Kations Sauerstoff-Fehlstellen entstehen, die ebenfalls einen wichtigen Einfluss auf die Katalysegeschwindigkeit haben.

Ein anderes Projekt bestand darin, unterschiedliche Morphologien von Ceroxid-Nanopartikeln auf ihre katalytische Aktivität zu untersuchen. Dafür wurde die oxidative Bromierung anhand der Bromierung von 2-Isopropyl-5-Methylphenol (Thymol) mittels NMR-Spektroskopie durchgeführt und ausgewertet. Dabei erwies sich ein deutlicher Unterschied zwischen den unterschiedlichen Morphologien bezüglich der katalytischen Aktivität. Auch hier zeigte sich, dass Einflüsse wie Zeta-Potential und BET-Oberfläche einen wichtigen Einfluss auf die Katalyse haben. Zusätzlich konnte mittels Raman-Spektroskopie gezeigt werden, dass die Ceroxid-Nanopartikel mit den unterschiedlichen Morphologien das Substrat Wasserstoffperoxid nach bereits kurzer Zeit an der Partikeloberfläche abbauten, was die Katalyse deutlich verlangsamte.

Als Anwendung wurden Polycarbonat-Plättchen mit funktionalisierten CeO_2-Nanopartikeln beschichtet. Für eine bessere Haftung der Partikel wurde mit Hilfe von Sauerstoff-Plasma eine polare Oberfläche geschaffen. Eine homogene Beschichtung aus funktionalisierten

Ceroxid-Nanopartikeln wurde verwendet, um ein Nanoenzym zu schaffen. Die Aufgabe des Nanoenzyms besteht darin, mit Hilfe der oxidativen Halogenierung Signalmoleküle der Bakterien zu bromieren, um das Biofilmwachstum zu inhibieren. Dadurch wird das veränderte Signalmolekül von den Bakterien nicht mehr erkannt und die Kommunikation wird unterbrochen, wodurch das Wachstum des Biofilms verringert wird. Anschließende Biotests, mit dem grammnegativen Bakterium *Pseudomonas aeruginosa*, zeigten nach der Beschichtung mit CeO_2-Nanopartikeln im Gegensatz zu reinen Polycarbonat-Plättchen eine Inhibierung des Biofilmwachstums um 75%.

V. General Remarks

The following is a short overview of the structure and content of this thesis. First, a theoretical background is explained and followed by an explanation of the motivation with the scientific goals. Each chapter is introduced by an author contribution and a short summary. References and associated supporting information are attached at the end of each chapter.

Chapter 3 of the thesis is in preparation for a publication. Chapter 4 is currently under revision in *Nanoscale* and chapter 5 has been already published in *Nanoscale* on November 17, 2021. The graphic design, numbering and formatting of the original publication have been adapted to this thesis.

The graphics were originally created with Matlab R2017b, CorelDRAW 2021 and PowerPoint. The data were analyzed, plotted and fitting with Matlab R2017b, OriginPro 8 or Excel. NMR spectra were analyzed with MestreNova, while chemical structures and schemes were prepared with ChemDraw 20.1.1. XPS data were analyzed and plotted with CasaXPS.

VI. Table of Contents

1 Theoretical Background

1.1. Nanoparticles

Nanoparticles are objects defined by their size of 1-100 nm.[1] These can be composed out of metals, metal oxides, or polymer nanoparticles. The characteristic of nanoparticles is their high specific surface area, because smaller particles have a larger surface area in relation to their volume. As a result, the surface has more contact with the surrounding and can react more efficiently with it.[2] Considerable attention is paid to nanoparticles in application areas such as solar cells[3], biomedicine[4], fuel cells[5], and catalysis[6]. Different models exist describing the nucleation and the growth of nanoparticles such as the LaMer[7] mechanism, Ostwald ripening[8], Finke-Watzky two step mechanism[9], and intraparticle growth[10]. Subsequently, only the LaMer model, which describes the mechanism of monodispersed nanoparticles, will be discussed in more detail.

1.1.1. LaMer model

The LaMer mechanism was created in 1950 by Victor LaMer und explains the growth of a crystal by separating it in two stages: the nucleation and the growth.[7] Originally, this process was associated with the synthesis of monodispersed sulfur sols from the decomposition of sodium thiosulfate. The LaMer model shows the formation of colloidal particles in three portions, as schematically shown in Figure 1.1. The hypothetical curve displays the concentration of the solute versus the time of the whole reaction process. In the first step (I), the concentration of the monomers increase continuously till the system becomes supersaturated. When a certain concentration is reached, which is between the minimum concentration C_{min} and the critical concentration C_{max}, a spontaneous nucleation starts (II). The nucleation rate is now high enough that nuclei of equal size are formed in the solution (III).[11–13]

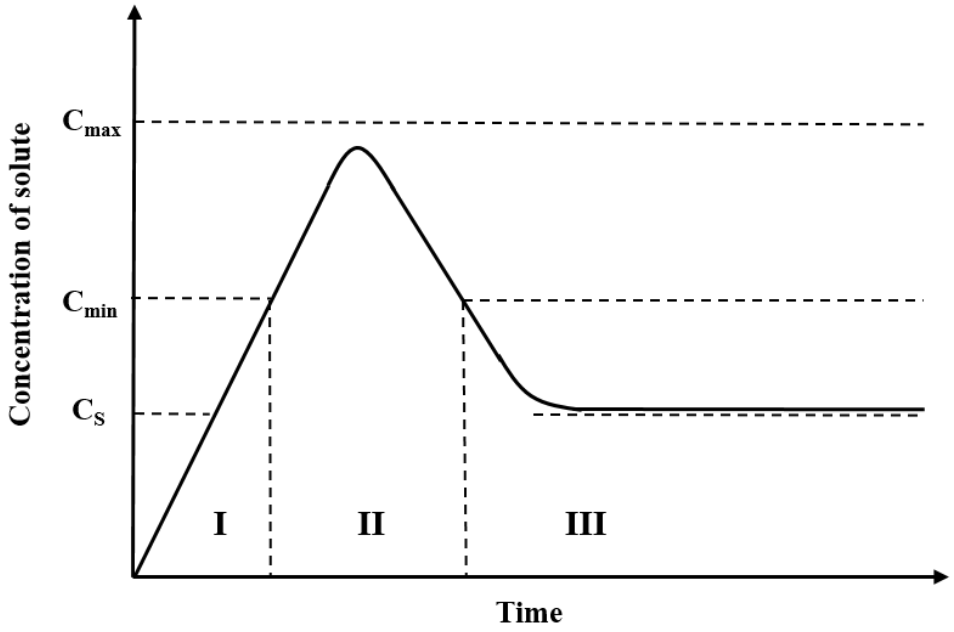

Figure 1.1. LaMer diagram: separation of nucleation and growth of nanoparticles. (I) Linear increase of the concentration (pre-nucleation), (II) Nucleation of particles, (III) Diffusion-controlled growth of the particles. [7]

1.2. Oxidative Halogenation

Oxidative halogenation (i.e., chlorination, bromination, or iodination) of organic molecules is of great importance in chemistry, whether as specifically designed precursors in materials chemistry, as industrial chemicals, or as biologically active compounds.[14] In classical chemical synthesis in the laboratory, toxic chemicals such as chlorine gas[15], bromine[16] or N-iodosuccinimide[17] are often used for this purpose. Regarding this disadvantage, a biomimetic approach has come to the attention in the last few years, which represent a catalytic process to yield halogenated products. In nature, a great number of enzymes are already known to exhibit the ability of halogenation. First discovered halogenation enzyme in the 1960s was the heme (iron-containing porphyrin) chloroperoxidase from the terrestrial fungus *Caldariomyces fumago*.[18] Later, enzymes containing other metals centers such as vanadium haloperoxidase or flavin-dependent, enzymes with non-metal centers, were identified. Figure 1.2 depicts the named enzymes.

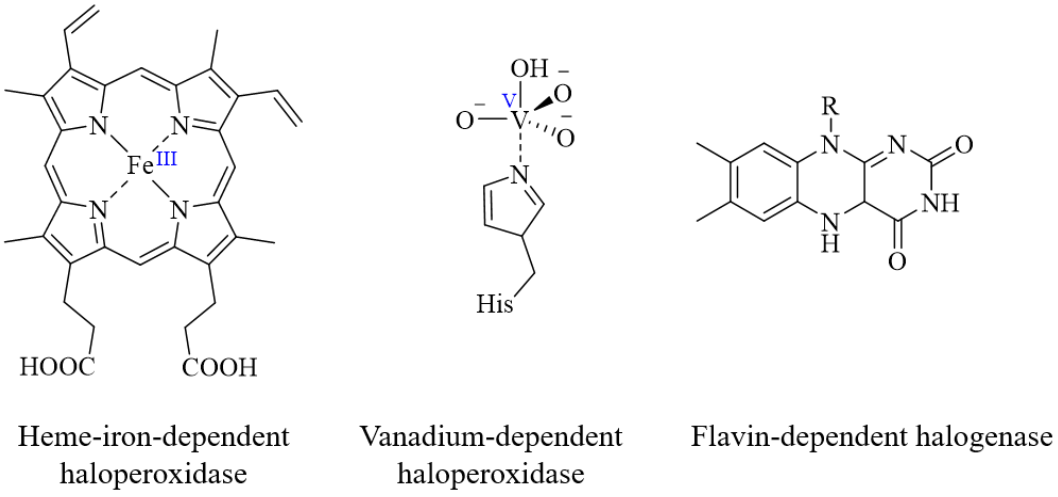

Heme-iron-dependent haloperoxidase | Vanadium-dependent haloperoxidase | Flavin-dependent halogenase

Figure 1.2. Structure of the enzymes heme iron-dependent haloperoxidase, vanadium-dependent haloperoxidase and flavin-dependent halogenase. [18,19]

Heme- and vanadium enzymes are classified as haloperoxidases because of their requirement for peroxide (mostly H_2O_2). Halogenases, in contrast, depend on the availability of oxygen (O_2). General equations for the reaction of a haloperoxidase and halogenase are presented below.

$$R\text{-}H + H_2O_2 + X^- + H^+ \xrightarrow[\text{"HOX"}]{\text{Haloperoxidase}} R\text{-}X + 2\ H_2O \qquad (1.1)$$

$$R\text{-}H + O_2 + X^- + H^+ \xrightarrow[\text{"HOX"}]{\text{Halogenase}} R\text{-}X + 2\ H_2O \qquad (1.2)$$

The equations (1.1) and (1.2) describes the reaction forming hypohalous acid (HOX) as an intermediate product, where the oxidation occurs on the halide. The agent is very reactive and can be used for halogenation of organic compounds in the form of electrophilic substitution. Another possibility is that the peroxide is bound to the metal center and the oxidation of the halide occurs at the enzyme center. Here, the metal center is optionally involved in the reaction as in the case of the heme-enzyme. In this process, Fe^{3+} is oxidized to Fe^{4+}. In the case of vanadium haloperoxidase the oxidation state of the vanadium (+V) does not change during the reaction. It only ensures a better stabilization of the oxidized halide "X^+".[18,19]

In the following, only the class of haloperoxidases will be discussed in more detail.

1.2.1. Vanadium haloperoxidase

Vanadium haloperoxidases are typically found in marine environments, where all substrates such as halides and peroxides are present. The first discovered vanadium haloperoxidase (V-HPO) was vanadium bromoperoxidase (V-BPO), which was isolated from the marine brown alga *Ascophyllum nodosum*.[20] Since that, three different types of vanadium-dependent haloperoxidases were found in nature: vanadium bromoperoxidase (V-BPO), vanadium chloroperoxidase (V-CPO) and vanadium iodoperoxidase (V-IPO). For this, V-CPO is preferably obtained from fungi and marine-derived bacteria and is able to oxidize chloride, bromide and iodide. V-BPO is found in marina algae and can oxidize only bromide and iodide.[18] V-IOP is only able to oxidize iodide and can be obtained from the brown alga *Laminaria digitata*.[21] The exact mechanism hasn't been properly elucidated to this point. So, Figure 1.3 shows the presumed mechanism of oxidative halogination for vanadium haloperoxidase.

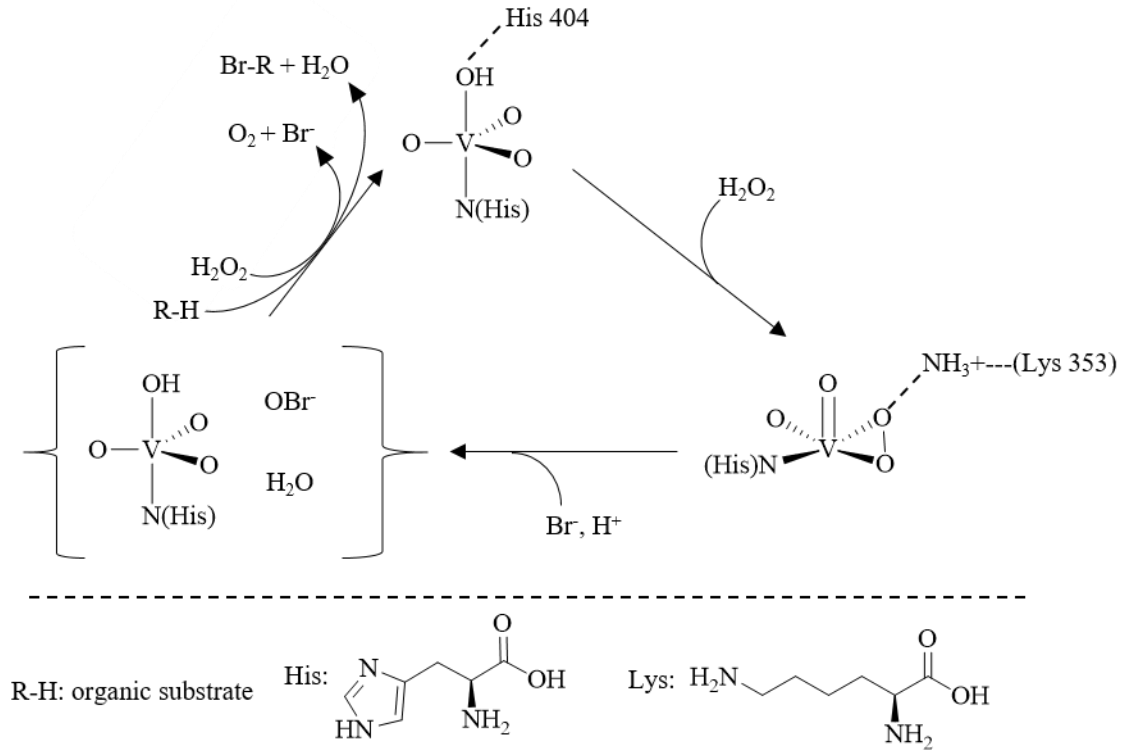

Figure 1.3. Proposed mechanism of oxidative bromination for vanadium-haloperoxidase.[18]

The reaction starts with the coordination of H_2O_2 at the vanadium (+V) state to form a stable peroxovanadate intermediate, whereby water is eliminated. In the next step, the oxygen-oxygen bond is cleaved by a nucleophilic attack by the bromide anion and the hypohalite (OBr^-) is formed. In order for a hypohalous acid (HOX) to be produced from the hypohalite, a proton is separated from the water. Now the hypohalous acid can react with the organic component and brominate it oxidatively[18,22,23] However, a singlet oxygen, which is also referred to as reactive oxygen species (=ROS) can be produced as a co-reaction.

1.3. Biofouling

Biofilms are cooperating microbial communities[24] adhered to non-living and living surfaces[25] and occur on food systems[26], hospital settings[27], and marine environment[25]. They are found in everyday life and may have positive or negative effects. One of the negative effects is that biofouling is associated with high costs and can negatively impact environments. For example, the annual consumption of fuel in shipping with antifouling paints could potentially save up to $60 billion and reduce additionally emissions of tons for carbon dioxide and sulfur dioxide per annum.[28] But also in the healthcare sector, biofilms produce many problems that can cause serious bacterial infections, which might result in fatalities for organisms.[29] However, there are also some positive effects of biofilms. They play an important role in the field of biofilm reactors, biosensors, or in water treatments.[30]

The formation of a biofilm starts with the settlement of organic molecules such as extracellular polysaccharides, structural proteins, and nucleic acids on the surface (Figure 1.4: I) Now these can proliferate on the surface (Figure 1.4: II). Bacteria can slowly colonize and multiply on this nutrient medium, forming a protective slime layer consisting of extracellular polymeric substances (EPS).

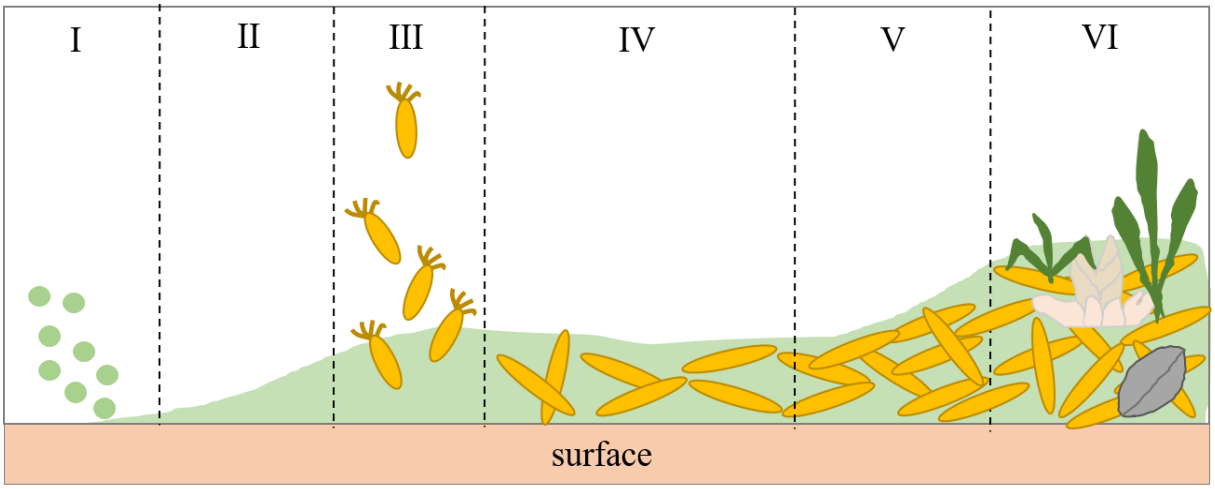

Figure 1.4. Biofilm formation on marine surfaces. (I) Settlement of organic molecules. (II) Formation of extracellular polymeric substances (EPS). (III) Reversible adsorption of bacteria. (IV) Bacterial proliferation, irreversible attachment of bacteria. (V) Growth and division of bacteria, biofilm formation. (VI) Attachment of other organisms to biofilm. [33]

The biofilm starts growing and more and more bacteria settle in microcolonies by cell-to-cell communication (quorum sensing). (Figure 1.4: III+IV) When the biofilm reaches the right mass, planktonic microorganisms spread in the environment to start a new cycle of biofilm formation.[31,32] (Figure 1.4 V+VI).

1.3.1. Quorum Sensing

It was supposed for a long time for bacteria being individual cells acting alone. Now, we know these organisms are capable of microbial social behavior.[34] A difference is drawn between the communication of gram-negative and gram-positive bacteria. In the following, the cell-density-dependent regulatory mechanism for the communication (quorum sensing (QS)) of gram-negative bacteria will be explained in more detail.[35] The process is based on the production, release and detection of so-called autoinducers (AI). Autoinducers are small molecules, and each bacterium has its own characteristic signal molecule(s). Two important groups of AI are presented by acylated homeserine lactone (AHL) and tetrahydroxytetrahydrofurane (THMF) (Figure 1.5).[36]

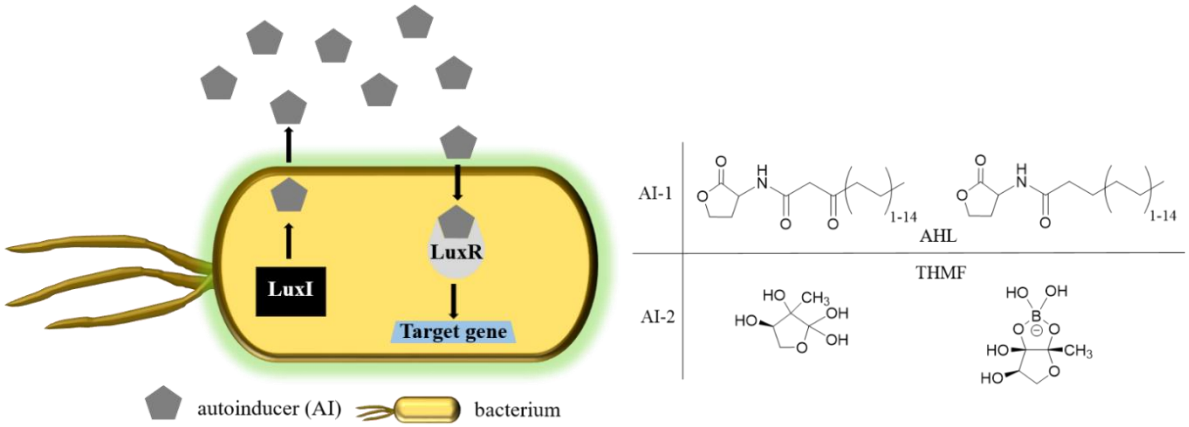

Figure 1.5. Illustration of the quorum sensing process in the gram-negative bacterium *Vibrio fischeri* on the left side. AHL autoinducers (grey sign) are produced by LuxI (black box) and are detected by LuxR (grey sign). Examples of main autoinducer (AI-1 & AI-2) of gram-positive & -negative bacteria are depicted on the right side. AI-1 is the supergroup of acyl-homoserine lactones (AHL) and AI-2 of tetrahydroxytetrahydrofurane (THMF). [37–40]

The cycle of the communication starts by the production of the AI by the protein LuxI, which is produced by the synthase gene (luxI) in the bacterium. The cell-population density is determined by the concentration of the AI, which means: the cell population density increases with increasing AI concentration. When a critical threshold concentration of AI is

reached, it is bound by the protein LuxR, which is a transcriptional regulator and turn activates the transcription of its target genes.[41–43] In the case of the bacterium *Vibrio fischeri*, the genes produce proteins which together create the enzyme luciferase. Luciferase catalyzes a redox reaction that produces blue-green light (bioluminescence). The concentration of the AI can therefore be inferred from the strength of the light. The simplified illustration for the quorum sensing cycle for the gram-negative bacterium *Vibrio fischeri* is presented in Figure 1.5. However, there are also bacteria that have multiple protein circuits for different autoinducers.[38]

1.3.2. Quorum Quenching

There is a great interest in interrupting the communication between the bacteria to prevent their group behavior. A phenomenon that permits this is quorum quenching (QQ). The concept of QQ is the antagonistic phenomenon of QS, which interrupt the cell-to-cell communication between the bacteria by sequestering and degrading signaling molecules.[37] In nature, enzymes exist that are capable quorum quenching. One of the earliest found enzymes was vanadium bromoperoxidase (V-BPO) extracted from the red algea *Delisea pulchra*.[40] V-BPO can brominate the signal molecule in the presence of H_2O_2 and a halide.[44] Figure 1.6 demonstrate the bromination and degradation of an AHL signal molecule by V-BPO in presence of bromide and hydrogen peroxide.

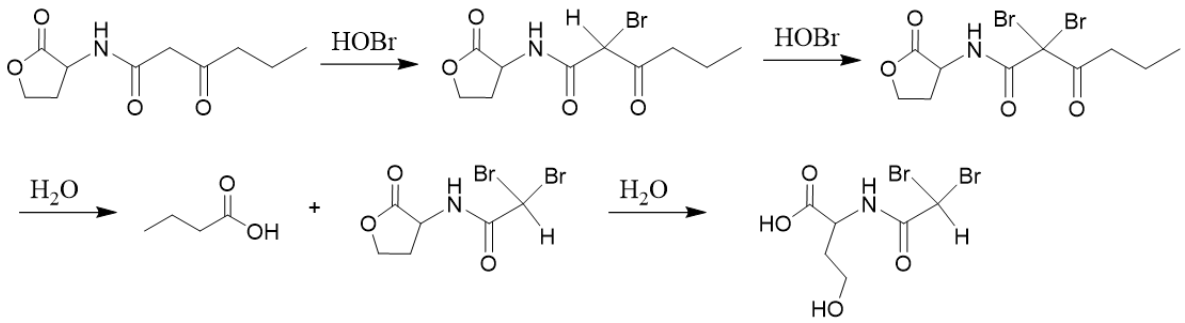

Figure 1.6. Mechanism of oxidative bromination and subsequent hydrolysis of an AI of the AHL group.[18]

By modification of the signal molecule, the cell-to-cell communication of the bacteria is interrupted and the colonization and thus the biofilm formation is stopped.

1.3.3. Biocides

Biocides is a collective designation for chemical substances used to control harmful plants and animals. The classification is split into further subcategories such as fungicide against fungi[45], herbicides against plants, or molluscicides against molluscs such as snails[46]. However, the significant problem with the utilization of biocides is the damage to other living organisms and not only to the specific targeted organism. Therefore, it is important in the application of biocides that it is completely harmless to humans and other living organisms in nature.[47] Biocides can behave by different mechanisms, distinguishing between chemical reaction, and ionic or physical interaction.[48] They are used, for example in air-conditioning technology, paints for ships[49] and facades[50], and wood preservatives[51].

A common chemical substance that has been used in paints in ship hulls as an antifouling reagent since 1960 is tributyltin (TBT). However, with time it has been revealed that this is a hazardous method of coating, as the compound leaches and enters the seawater. The increased concentration of tin in water has a serious effect on the organisms and can lead to symptoms of poisoning or even death. Finally, TBT has been banned from use as a biocide in marine paints since 2003 and has not been authorized to be marked as a biocide in the EU since 2006. The resulting market gap brought copper and copper salts to the fore as an antifouling reagent.[52] The most active copper species is cuprous oxide (Cu_2O) and copper. However, copper has also turned out to leach and endanger the growth of various aquatic organisms like some marine algae, calms, or sea breams. [49] The toxicity of copper occurs through several mechanisms (Figure 1.7).

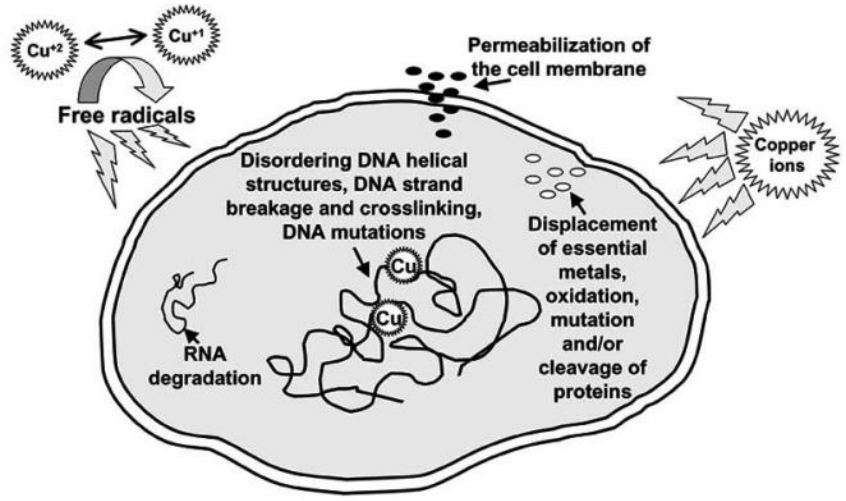

Figure 1.7. Schematic illustration of the mechanisms of toxicity of copper to microorganisms. [53]

Copper can mediate a cell membrane damage. Consequently, the mobile cellular solutes, such as potassium ions, leaks out of the cell and leads to death. However, when copper-ions (Cu^{2+}) enters the interior of the cell, it binds to the DNA helical structures through its specific affinity by crosslinking within and between the DNA strands. This leads to mutation of the cell. [53]

It is known that copper can generate radicals through a Fenton reaction.[54] This results in the formation of so-called reactive oxygen species (=ROS). These free radicals are responsible for the destruction of RNA strands in the cell. [53]

1.4. Haloperoxidase Mimetics

Enzymes are essential to the metabolism of all living organisms. For economic applications, these are biocatalysts that control biochemical reactions in organisms without being altered themselves. However, the disadvantage of enzymes is their hard handling and high manufacturing cost. Consequently, so-called nanozymes became the focus of research in recent years, which refer to nanomaterials with enzyme mimicking activities.[55] Nanozymes offer several benefits such as higher catalytic stability, ease of modification, and lower manufacturing cost.[56] Previously, it was reported that various nanoparticles composed of metals or metal oxides mimic functions of various enzymes: i) Fe_3O_4 [57], CuO[58], and carbon nanodots for peroxidase[59], ii) MnO_2[60] and Co_3O_4[61] for catalase, and iii) V_2O_5[62] and CeO_2[63] for haloperoxidase.[64]

The first results for mimicking haloperoxidase with V_2O_5 nanowires were obtained by *Natalio et al.* (2012) with vanadium (+V) as active centrum. The nanowires showed strong biocidal activity against *Staphylococcus aureus* and *Escherichia coli* and a prevention of biofilm growth on surfaces coated with paints containing V_2O_5 nanowires exposed to seawater was observed.[62] However, the main disadvantage of using V_2O_5 is the critical classification to the REACH criteria because of the fact that it is carcinogenic, mutagenic, and teratogenic.[65] *Hergert et al.* identified the nanozyme in the form of CeO_2 nanoparticles with a haloperoxidase like-activity that has no analogous disadvantage. The advantage of CeO_2 is that it can switch between the oxidation states Ce^{3+} and Ce^{4+}due to tis preferable redox potential. This results in a non-stoichiometric fluorite structure with oxygen vacancies ($CeO_{2-\delta}$).[66] This make ceria an attractive candidate for catalysis.

The oxygen storage capacity, stability, and activity of CeO_2 can be improved by doping of various elements. By doping with a trivalent element (M^{3+}), Ce^{4+} positions are replaced, and more oxygen vacancies are created. This facilitates the diffusion of oxygen deficiencies and consequently increase the catalytic activity.[67]

1.5. Haloperoxidase Assay

Haloperoxidase activity of nanoparticles can be detected photometrically using a dye assay. In this assay, the dye phenol red (PR, phenolsulfonphthalein) is brominated fourfold to bromphenol blue (3′,3″,5′,5″-tetrabromophenolsulfonphthalein) in the presence of H_2O_2 and the halide Br^- in aqueous solution. The absorption maximum of PR is at 434 nm and the maximum of Br_4PR is at 592 nm. Because the absorption maxima are far apart, the time course of the reaction can be followed photometrically. [68]

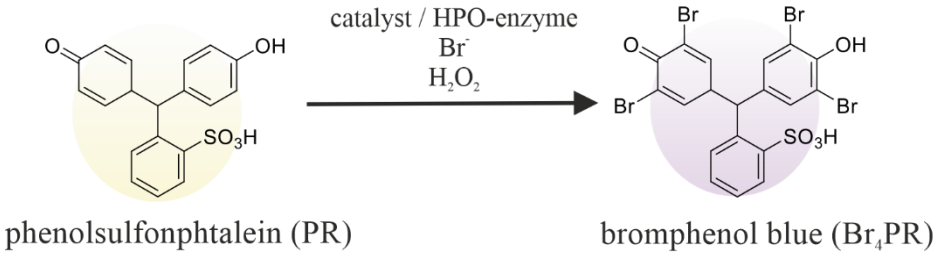

Figure 1.8. Reaction of the oxidative bromination of phenolsulfonphthalein (PR) to bromphenol blue (Br_4PR).[68]

1.6. Cerium oxide

Cerium is the most abundant element of the lanthanides with an occurrence of~$4.3 \cdot 10^{-3}$% in the earth's crust, comparable in abundance with copper.[69] Ceria has a stable cubic fluorite ($Fm\bar{3}m$) crystal structure, which is composed of a face centered cubic (fcc) package of Ce cations. All tetrahedral gaps are occupied by oxygen anions. Thus, one cerium cation is enclosed by eight oxygen anion, and each oxygen anion by four cerium cations (Figure 1.9).[70,71]

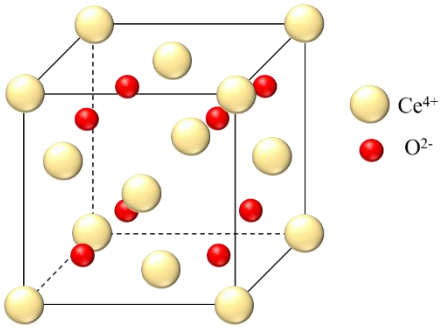

Figure 1.9. Fluorite unit cell of CeO_2.[70]

Cerium can be represented in the oxidation states +3 and +4. Due to its high reduction potential ($E_0(Ce^{3+}/Ce^{4+})$=+1.72 V)[72] in aqueous medium, the significant catalytic activity by ceria is attributed to its "oxygen storage capacity": oxygen is liberated by reducing Ce^{4+} to Ce^{3+} and being reabsorbed during reoxidation of Ce^{3+} to Ce^{4+}.[73] However, the exact mechanism is complex and has not yet been investigated in detail.

Other important benefits of CeO_2 are its low solubility and low acute toxicity. [74]

CeO_2 lends its use to a wide variety of applications: as an important promoter in the automotive three way catalysts (TWCs), as a component in solid oxide fuel cells (SOFCs), and as catalyst for organic transformations.[75,76]

1.7. Mechanochemistry

Mechanochemistry defines the chemical reactions that are initiated by mechanical energy at room temperature. It has recently attracted a significant interest because of its advantages, such as being a solution-free, energy saving, high-productivity and low-temperature process.[77] This type of process can be achieved with a planetary ball mill (Figure 1.10A), which provides a convenient option for up-scaling, synthesis of nanoparticles[78] or amorphous compounds.[79] Initially, the material is transferred to a corundum beaker - if necessary, a dispersion medium can be added. Additionally, balls with a high degree of hardness, like zirconium oxide or tungsten carbide, are added to the beaker. The mechanism of milling is displayed in Figure 1.10B.

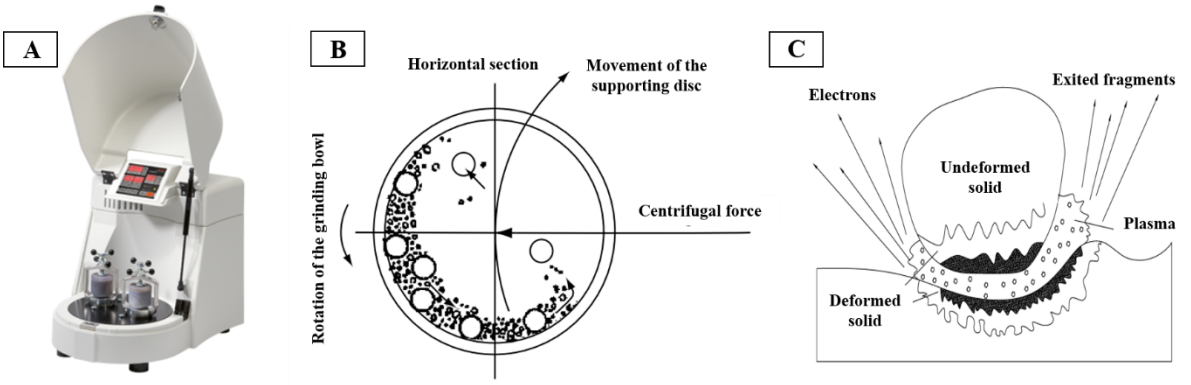

Figure 1.10. a) A picture of a planetary ball mill from Fritsch used in this work.[80] b) Working principle of ball milling process of a planetary ball mill.[81] c) Schema of the magma-plasma model, which shows the process occurring during mechanochemical activation.[82]

The beaker rotates on a plate and around its own axis, where centrifugal force is produced. The mechanical energy results from collisions between the balls and between balls and walls, which are responsible for grinding of the material. During grinding, the movement of the balls depend on few parameters like the revolution speed (up to several 100 rpm) and/ or the filling ratio of the jar. [81]

The so-called magma-plasma model was discovered by *Thiessen et al*. in 1967 to describe the process between an undeformed and deformed solid.[83] The model reveals that local temperatures of more than 1000 K can be achieved. This induces an exited state, and the resulting amount of energy can transform the material into a plasmonic state characterized by formation and ejection of electrons, photons, and excited fragments (Figure 1.10C).[82]

1.8. References

1. S. Hasan, A Review on Nanoparticles: Their Synthesis and Types. *Res. J. Recent Sci.* 2015. **4**, 9–11.
2. P. Holister, J.-W. Weener, C. R. Vas, T. Harper, Technology White Papers nr. 3 Nanoparticles, (available at www.cientifica.com).
3. D. Kishore Kumar, J. Kříž, N. Bennett, B. Chen, H. Upadhayaya, K. R. Reddy, V. Sadhu, Functionalized metal oxide nanoparticles for efficient dye-sensitized solar cells (DSSCs): A review. *Mater. Sci. Energy Technol.* 2020. **3**, 472–481.
4. Q. A. Pankhurst, J. Connolly, S. K. Jones, J. Dobson, Applications of magnetic nanoparticles in biomedicine. *J. Phys. D. Appl. Phys.* 2003. **36**, R167.
5. K. Y. Chan, J. Ding, J. Ren, S. Cheng, K. Y. Tsang, Supported mixed metal nanoparticles as electrocatalysts in low temperature fuel cells. *J. Mater. Chem.* 2004. **14**, 505–516.
6. J. B. Sambur, P. Chen, Approaches to single-nanoparticle catalysis. *Annu. Rev. Phys. Chem.* 2014. **65**, 395–422.
7. V. K. Lamer, R. H. Dinegar, Theory, Production and Mechanism of Formation of Monodispersed Hydrosols. *J. Am. Chem. Soc.* 1950. **72**, 4847–4854.
8. A. Stabel, R. Heinz, F. C. De Schryver, J. P. Rabe, Ostwald Ripening of Two-Dimensional Crystals at the Solid-Liquid Interface. *J. Phys. Chem*. 1995. **99**, 505–507.
9. L. Bentea, M. A. Watzky, R. G. Finke, Sigmoidal Nucleation and Growth Curves Across Nature Fit by the Finke-Watzky Model of Slow Continuous Nucleation and Autocatalytic Growth: Explicit Formulas for the Lag and Growth Times Plus Other Key Insights. *J. Phys. Chem. C*. 2017. **121**, 5302–5312.
10. X. Peng, L. Manna, W. Yang, J. Wickham, E. Scher, A. Kadavanich, A. P. Alivisatos, Shape control of CdSe nanocrystals. *Nat.* . 2000. **404**, 59–61.
11. C. B. Whitehead, S. Özkar, R. G. Finke, LaMer's 1950 Model for Particle Formation of Instantaneous Nucleation and Diffusion-Controlled Growth: A Historical Look at the Model's Origins, Assumptions, Equations, and Underlying Sulfur Sol Formation Kinetics Data. *Chem. Mater.* 2019. **31**, 7116–7132.
12. K. Rajan, I. Roppolo, A. Chiappone, S. Bocchini, D. Perrone, A. Chiolerio, Silver nanoparticle ink technology: State of the art. *Nanotechnol. Sci. Appl.* 2016. **9**,1-13.
13. N. T. K. Thanh, N. Maclean, S. Mahiddine, Mechanisms of Nucleation and Growth of Nanoparticles in Solution. *Chem. Rev.* 2014. **114**, 7610–7630.
14. A. Podgoršek, M. Zupan, J. Iskra, Oxidative Halogenierungen mit umweltschonenden Oxidationsmitteln: Sauerstoff und Wasserstoffperoxid. *Angew. Chemie*. 2009. **121**, 8576–8603.
15. G. A. Olah, Electrophilic methane conversion. *Acc. Chem. Res.* 2002. **20**, 422–428.
16. K. Pilgram, M. Zupan, R. Skiles, Bromination of 2,1,3-benzothiadiazoles. *J. Heterocycl. Chem.* 1970. **7**, 629–633.
17. K. Tanemura, T. Suzuki, Y. Nishida, K. Satsumabayashi, T. Horaguchi, Halogenation of Aromatic Compounds by N-chloro-, N-bromo-, and N-iodosuccinimide. 2003. **32**, 932–933.
18. A. Butler, M. Sandy, Mechanistic considerations of halogenating enzymes. *Nature*. 2009. **460**, 848–854.

19. M. C. Andorfer, J. C. Lewis, Understanding and Improving the Activity of Flavin-Dependent Halogenases via Random and Targeted Mutagenesis. 2018. **87**, 159–185.

20. A. Butler, Vanadium haloperoxidases. *Curr. Opin. Chem. Biol.* 1998. **2**, 279–285.

21. J. B. Fournier, E. Rebuffet, L. Delage, R. Grijol, L. Meslet-Cladière, J. Rzonca, P. Potin, G. Michel, M. Czjzek, C. Leblanc, The vanadium iodoperoxidase from the marine Flavobacteriaceae species Zobellia galactanivorans reveals novel molecular and evolutionary features of halide specificity in the vanadium haloperoxidase enzyme family. *Appl. Environ. Microbiol.* 2014. **80**, 7561–7573.

22. G. Zampella, P. Fantucci, V. L. Pecoraro, L. De Gioia, Reactivity of Peroxo Forms of the Vanadium Haloperoxidase Cofactor. A DFT Investigation. *J. Am. Chem. Soc.* 2004. **127**, 953–960.

23. A. V. Fejzagić, J. Gebauer, N. Huwa, T. Classen, Halogenating enzymes for active agent synthesis: First steps are done and many have to follow. *Molecules*. 2019. **24**, 4008.

24. S. K. Yadav, S. Sanyal, Biofilms: The Good and the Bad. *Biofilms Hum. Dis. Treat. Control*. 2019, 13–26.

25. S. Kavitha, V. Raghavan, Isolation and characterization of marine biofilm forming bacteria from a ship's hull. *Front. Biol.* 2018. **13**, 208–214.

26. L. V. Poulsen, Microbial Biofilm in Food Processing. *LWT - Food Sci. Technol.* 1999. **32**, 321–326.

27. P. Tenke, B. Kovacs, M. Jäckel, E. Nagy, The role of biofilm infection in urology. *World J. Urol.* 2006. **24**, 13–20.

28. M. Salta, J. A. Wharton, P. Stoodley, S. P. Dennington, L. R. Goodes, S. Werwinski, U. Mart, R. J. K. Wood, K. R. Stokes, Designing biomimetic antifouling surfaces. *Philos. Trans. R. Soc. A Math. Phys. Eng. Sci.* 2010. **368**, 4729–4754.

29. L. Hall-Stoodley, J. W. Costerton, P. Stoodley, Bacterial biofilms: from the Natural environment to infectious diseases. *Nat. Rev. Microbiol*. 2004. **2**, 95–108.

30. Sunil Kumar, Niharika Chandra, Leena Singh, Muhammad Zaffar Hashmi, Ajit Varma, *Biofilms in Human Diseases: Treatment and Control*

31. R. Vasudevan, Biofilms: Microbial Cities of Scientific Significance. *J. Microbiol. Exp.* 2014, **1**, 84-98.

32. H.-C. Flemming, Why Microorganisms Live in Biofilms and the Problem of Biofouling. *Mar. Ind. Biofouling*. 2009, 3–12.

33. M. Toyofuku, T. Inaba, T. Kiyokawa, N. Obana, Y. Yawata, N. Nomura, Environmental factors that shape biofilm formation. *Biosci. Biotechnol. Biochem.* 2016. **80**, 7–12.

34. M. E. Davey, G. A. O'toole, Microbial Biofilms: from Ecology to Molecular Genetics. *Microbiol. Mol. Biol. Rev.* 2000. **64**, 867.

35. C. M. Waters, B. L. Bassler, QUORUM SENSING: Cell-to-Cell Communication in Bacteria. *Annual Review of Cell and Development Biology*. 2005. **21**, 319–346.

36. L. Zhang, S. Li, X. Liu, Z. Wang, M. Jiang, R. Wang, L. Xie, Q. Liu, X. Xie, D. Shang, M. Li, Z. Wei, Y. Wang, C. Fan, Z. Q. Luo, X. Shen, Sensing of autoinducer-2 by functionally distinct receptors in prokaryotes. *Nat. Commun.* 2020. **11**, 1–13.

37. O. Kareb, M. Aïder, Quorum Sensing Circuits in the Communicating Mechanisms of

Bacteria and Its Implication in the Biosynthesis of Bacteriocins by Lactic Acid Bacteria: a Review. *Probiotics Antimicrob. Proteins*. 2020. **12**, 5–17.

38. N. J. Tobias, J. Brehm, D. Kresovic, S. Brameyer, H. B. Bode, R. Heermann, New Vocabulary for Bacterial Communication. *ChemBioChem*. 2020. **21**, 759–768.

39. T. J. Tavender, N. M. Halliday, K. R. Hardie, K. Winzer, LuxS-independent formation of AI-2 from ribulose-5-phosphate. *BMC Microbiol.* 2008. **8**, 1–8.

40. M. Sandy, J. N. Carter-Franklin, J. D. Martin, A. Butler, Vanadium bromoperoxidase from Delisea pulchra: enzyme-catalyzed formation of bromofuranone and attendant disruption of quorum sensing. *Chem. Commun.* 2011. **47**, 12086–12088.

41. Y. H. Li, X. Tian, Quorum Sensing and Bacterial Social Interactions in Biofilms. *Sensors*. 2012. **12**, 2519–2538.

42. M. B. Miller, B. L. Bassler, Quorum Sensing in Bacteria. *Front. Microbiol*. 2003. **55**, 165–199.

43. M. Schuster, D. Joseph Sexton, S. P. Diggle, E. Peter Greenberg, Acyl-homoserine lactone quorum sensing: from evolution to application. *Annu. Rev. Microbiol.* 2013. **67**, 43–63.

44. M. Syrpas, E. Ruysbergh, L. Blommaert, B. Vanelslander, K. Sabbe, W. Vyverman, N. De Kimpe, S. Mangelinckx, Haloperoxidase Mediated Quorum Quenching by Nitzschia cf pellucida: Study of the Metabolization of N-Acyl Homoserine Lactones by a Benthic Diatom. *Mar. Drugs.* 2014. **12**, 352–367.

45. P. E. Russell, A century of fungicide evolution. *J. Agric. Sci.* 2005. **143**, 11–25.

46. H. I. Hussein, A. Kamel, M. Abou-Zeid, Abdel-Khalek, H. El-Sebae, M. A. Saleh, Uscharin, the most potent molluscicidal compound tested against land snails. *J. Chem. Ecol*. 1994. **20**, 135–140.

47. W. Legrum, *Toxikologie der Biozide.*

48. S. P. Denyer, G. S. A. B. Stewart, Mechanisms of action of disinfectants. *Int. Biodeterior. Biodegradation*. 1998. **41**, 261–268.

49. R. De Nys, J. Guenther, The impact and control of biofouling in marine finfish aquaculture. *Adv. Mar. Antifouling Coatings Technol.* 2009, 177–221.

50. U. Schoknecht, J. Gruycheva, H. Mathies, H. Bergmann, M. Burkhardt, Leaching of biocides used in façade coatings under laboratory test conditions. *Environ. Sci. Technol.* 2009. **43**, 9321–9328.

51. C. C. Borges, G. H. D. Tonoli, T. M. Cruz, P. J. Duarte, T. A. Junqueira, Nanoparticles-Based Wood Preservatives: next generation of wood protection? *CERNE*. 2018. **24**, 397–407.

52. S. Brooks, M. Waldock, The use of copper as a biocide in marine antifouling paints. *Adv. Mar. Antifouling Coatings Technol.* 2009, 492–521.

53. G. Borkow, J. Gabbay, Copper as a Biocidal Tool. *Curr. Med. Chem.* 2005. **12**, 2163–2175.

54. M. Shi, H. S. Kwon, Z. Peng, A. Elder, H. Yang, Effects of surface chemistry on the generation of reactive oxygen species by copper nanoparticles. *ACS Nano*. 2012. **6**, 2157–2164.

55. H. Wang, K. Wan, X. Shi, H. Wang, K. Wan, X. Shi, Recent Advances in Nanozyme Research. *Adv. Mater*. 2019. **31**, 1805368.

56. D. Jiang, D. Ni, Z. T. Rosenkrans, P. Huang, X. Yan, W. Cai, Nanozyme: new horizons for

responsive biomedical applications. *Chem. Soc. Rev.* 2019. **48**, 3683–3704.

57. H. Wei, E. Wang, Fe3O4 Magnetic Nanoparticles as Peroxidase Mimetics and Their Applications in H2O2 and Glucose Detection. *Anal. Chem.* 2008. **80**, 2250–2254.

58. W. Chen, J. Chen, Y. Bin Feng, L. Hong, Q. Y. Chen, L. F. Wu, X. H. Lin, X. H. Xia, Peroxidase-like activity of water-soluble cupric oxide nanoparticles and its analytical application for detection of hydrogen peroxide and glucose. *Analyst*. 2012. **137**, 1706–1712.

59. W. Shi, Q. Wang, Y. Long, Z. Cheng, S. Chen, H. Zheng, Y. Huang, Carbon nanodots as peroxidase mimetics and their applications to glucose detection. *Chem. Commun.* 2011. **47**, 6695–6697.

60. R. T. Rasheed, S. D. Al-Algawi, R. M. N., Synthesis and Catalase Mimic Activity of MnO2 Nano Powder Prepared by Hydrothermal Process. *J. Univ. BABYLON Pure Appl. Sci.* 2019. **27**, 228–237.

61. J. Mu, L. Zhang, M. Zhao, Y. Wang, Co3O4 nanoparticles as an efficient catalase mimic: Properties, mechanism and its electrocatalytic sensing application for hydrogen peroxide. *J. Mol. Catal. A Chem.* 2013. **378**, 30–37.

62. F. Natalio, R. André, A. F. Hartog, B. Stoll, K. P. Jochum, R. Wever, W. Tremel, Vanadium pentoxide nanoparticles mimic vanadium haloperoxidases and thwart biofilm formation. *Nat. Nanotechnol. 2012 78*. 2012. **7**, 530–535.

63. K. Herget, P. Hubach, S. Pusch, P. Deglmann, H. Götz, T. E. Gorelik, ya A. Gural, F. Pfitzner, T. Link, S. Schenk, M. Panthöfer, V. Ksenofontov, U. Kolb, T. Opatz, R. André, W. Tremel, K. Herget, T. E. Gorelik, I. A. Gural, F. Pfitzner, M. Panthöfer, V. Ksenofontov, U. Kolb, W. Tremel, P. Hubach, R. André, S. Pusch, T. Opatz, P. Deglmann, S. Schenk, H. Götz, T. Link, Haloperoxidase Mimicry by CeO2−x Nanorods Combats Biofouling. *Adv. Mater.* 2017. **29**, 1603823.

64. T. Kang, Y. G. Kim, D. Kim, T. Hyeon, Inorganic nanoparticles with enzyme-mimetic activities for biomedical applications. *Coord. Chem. Rev.* 2020. **403**, 213092.

65. F. L. Assem, L. S. Levy, A Review of Current Toxicological Concerns on Vanadium Pentoxide and Other Vanadium Compounds: Gaps in Knowledge and Directions for Future Research. *Journal of Toxicology and Environmental Health* 2009. **12**, 289–306.

66. C. T. Campbell, C. H. F. Peden, Oxygen vacancies and catalysis on ceria surfaces. *Science.* 2005. **309**, 713–714.

67. K. Singh, K. Kumar, S. Srivastava, A. Chowdhury, Effect of rare-earth doping in CeO2 matrix: Correlations with structure, catalytic and visible light photocatalytic properties. *Ceram. Int.* 2017. **43**, 17041–17047.

68. K. Herget, P. Hubach, S. Pusch, P. Deglmann, H. Götz, T. E. Gorelik, I. A. Gural'skiy, F. Pfitzner, T. Link, S. Schenk, M. Panthöfer, V. Ksenofontov, U. Kolb, T. Opatz, R. André, W. Tremel, Haloperoxidase Mimicry by CeO_{2-x} Nanorods Combats Biofouling. *Adv. Mater.* 2017. **29**, 1603823.

69. Rare Earth Elements—Critical Resources for High Technology | USGS Fact Sheet 087-02, (available at https://pubs.usgs.gov/fs/2002/fs087-02/).

70. R. Schmitt, A. Nenning, O. Kraynis, R. Korobko, A. I. Frenkel, I. Lubomirsky, S. M. Haile, J. L. M. Rupp, A review of defect structure and chemistry in ceria and its solid solutions. *Chem. Soc. Rev.* 2020. **49**, 554–592.

71. C. Janiak, H.-J. Meyer, D. Gudat, P. Kurz, *Riedel Moderne Anorganische Chemie* (De Gruyter).

72. J. T. Dahle, Y. Arai, Environmental geochemistry of cerium: Applications and toxicology of cerium oxide nanoparticles. *Int. J. Environ. Res. Public Health*. 2015. **12**, 1253–1278.

73. S. L. Swartz, Catalysis by Ceria and Related Materials Edited. *J. Am. Chem. Soc*. 2002. **124**, 12923–12924.

74. M. Kumari, S. P. Singh, S. Chinde, M. F. Rahman, M. Mahboob, P. Grover, Toxicity study of cerium oxide nanoparticles in human neuroblastoma cells. *Int. J. Toxicol.* 2014. **33**, 86–97.

75. T. Montini, M. Melchionna, M. Monai, P. Fornasiero, Fundamentals and Catalytic Applications of CeO2-Based Materials. *Chem. Rev.* 2016. **116**, 5987–6041.

76. L. Li, B. Zhu, J. Zhang, C. Yan, Y. Wu, Electrical properties of nanocube CeO2 in advanced solid oxide fuel cells. *Int. J. Hydrogen Energy*. 2018. **43**, 12909–12916.

77. S. Mateti, M. Mathesh, Z. Liu, T. Tao, T. Ramireddy, A. M. Glushenkov, W. Yang, Y. I. Chen, Mechanochemistry: A force in disguise and conditional effects towards chemical reactions. *Chem. Commun.* 2021. **57**, 1080–1092.

78. J. E. Muñoz, J. Cervantes, R. Esparza, G. Rosas, Iron nanoparticles produced by high-energy ball milling. *J. Nanoparticle Res.* 2007. **9**, 945–950.

79. S. Leukel, M. Panthöfer, M. Mondeshki, G. Kieslich, Y. Wu, N. Krautwurst, W. Tremel, Mechanochemical Access to Defect-Stabilized Amorphous Calcium Carbonate. *Chem. Mater*. 2018. **30**, 6040–6052.

80. Planeten-Mikromühle PULVERISETTE 7 classic line / Beschreibung , (available at https://www.fritsch.de/probenaufbereitung/ueberblick/details/produkt/pulverisette-7-classic-line/).

81. V. Baheti, R. Abbasi, J. Militky, Ball milling of jute fibre wastes to prepare nanocellulose. *World J. Eng.* 2012. **9**, 45–50.

82. I. Tole, K. Habermehl-Cwirzen, A. Cwirzen, Mechanochemical activation of natural clay minerals: an alternative to produce sustainable cementitious binders – review. *Mineral. Petrol.* 2019. **113**, 449–462.

83. P. A. Thießen, Physikalisch-chemische Untersuchungen tribomechanischer Vorgänge (Fragestellung, Ergebnisse, Aussichten). *Zeitschrift für Chemie*. 1965. **5**, 162–171.

2 Motivation and Scientific Goals

Nanozymes are nanomaterials with an enzyme-like characteristic and have gained importance in the last decades due to the great advantages such as low costs, good stability, and easy storage compared to natural enzymes. One of the first nanozymes were Fe_3O_4 nanoparticles with an intrinsic peroxidase-mimicking activity. After that, other compounds were quickly discovered that can mimic the catalytic activity of haloperoxidase, oxidase, catalase, and many more. [1–3]

In this work, the focus is on mimicking the enzyme haloperoxidase because of its capability to oxidatively brominate organic molecules. Organometallic vanadium complexes have already emerged as a possibility for mimicking haloperoxidase.[4] In 2012, V_2O_5 nanorods were synthesized by *Natalio et al.,* which also demonstrated haloperoxidase-like activity.[5] However, the use of V_2O_5 in the environment is not harmless and alternatives continued to be investigated.[6] A few years later (2017), *Herget et al.* managed the problem by synthesizing CeO_2 nanoparticles that exhibited even better haloperoxidase activity.[7,8] The nanoparticles are expected to find application in inhibiting biofilm growth due to haloperoxidase-like activity.[9] Biofilm growth is caused by communication of bacteria with the support of signal molecules.[10] This communication can be interrupted by the enzyme in the presence of H_2O_2 and a halide by chemically altering the signal molecule through oxidative bromination. [11]

The scientific goal of this work is to investigate in more detail the different influences on the catalytic activity of CeO_2 nanoparticles and to obtain a composite that has a potential application in everyday life. Since the surface of the nanoparticles is involved in the reaction, it was studied in more detail in the first two chapters of this thesis.

On the one hand, it should be determined whether different morphologies of CeO_2 lead to a difference in catalytic activity and what changes occur in the surface properties. A synthesis for oxidative bromination on the molecule thymol (2-isopropyl-5-methylphenol) with CeO_2 as nanocatalyst should be established. For the interpretation of the various rate constant for bromination, the parameters such as Lewis-acidity, ζ-potential and BET specific surface area will be discussed in more detail.

Another possibility to increase the catalytic activity is to dope nanoparticles. The synthesis will be performed using a planetary ball mill, which should facilitate the upscaling. Here,

the defect density of the nanoparticle surface will be studied using Raman and ESR spectroscopy. Also, FTIR measurements will be used to observe whether differences exist in the intensity of the vibration modes and whether a correlation with the ζ-potential can be explored.

In the third chapter it will be presented if a composite of CeO_2 and a polymer can prevent the biofilm formation of a Gram-negative bacterium by quorum quenching. This will be confirmed using bioassays.

2.1. References

1. M. Liang, X. Yan, Nanozymes: From New Concepts, Mechanisms, and Standards to Applications. *Acc. Chem. Res.* 2019. **52**, 2190–2200.
2. H. Wei, E. Wang, Fe3O4 Magnetic Nanoparticles as Peroxidase Mimetics and Their Applications in H2O2 and Glucose Detection. *Anal. Chem.* 2008. **80**, 2250–2254.
3. R. André, F. Natálio, M. Humanes, J. Leppin, K. Heinze, R. Wever, H. C. Schröder, W. E. G. Müller, W. Tremel, V2O5 Nanowires with an Intrinsic Peroxidase-Like Activity. *Adv. Funct. Mater*. 2011. **21**, 501–509.
4. B. J. Hamstra, G. J. Colpas, V. L. Pecoraro, Reactivity of Dioxovanadium(V) Complexes with Hydrogen Peroxide: Implications for Vanadium Haloperoxidase. *Inorg. Chem.* 1998. **37**, 949–955.
5. F. Natalio, R. André, A. F. Hartog, B. Stoll, K. P. Jochum, R. Wever, W. Tremel, Vanadium pentoxide nanoparticles mimic vanadium haloperoxidases and thwart biofilm formation. *Nat. Nanotechnol. 2012 78*. 2012. **7**, 530–535.
6. F. L. Assem, L. S. Levy, A Review of Current Toxicological Concerns on Vanadium Pentoxide and Other Vanadium Compounds: Gaps in Knowledge and Directions for Future Research. 2009. **12**, 289–306.
7. K. Herget, P. Hubach, S. Pusch, P. Deglmann, H. Götz, T. E. Gorelik, ya A. Gural, F. Pfitzner, T. Link, S. Schenk, M. Panthöfer, V. Ksenofontov, U. Kolb, T. Opatz, R. André, W. Tremel, K. Herget, T. E. Gorelik, I. A. Gural, F. Pfitzner, M. Panthöfer, V. Ksenofontov, U. Kolb, W. Tremel, P. Hubach, R. André, S. Pusch, T. Opatz, P. Deglmann, S. Schenk, H. Götz, T. Link, Haloperoxidase Mimicry by CeO2−x Nanorods Combats Biofouling. *Adv. Mater*. 2017. **29**, 1603823.
8. K. Herget, H. Frerichs, F. Pfitzner, M. N. Tahir, W. Tremel, Functional Enzyme Mimics for Oxidative Halogenation Reactions that Combat Biofilm Formation. *Adv. Mater.* 2018. **30**, 1707073.
9. H. Frerichs, E. Pütz, F. Pfitzner, T. Reich, A. Gazanis, M. Panthöfer, J. Hartmann, O. Jegel, R. Heermann, W. Tremel, Nanocomposite antimicrobials prevent bacterial growth through the enzyme-like activity of Bi-doped cerium dioxide (Ce1−xBixO2−δ). *Nanoscale*. 2020. **12**, 21344–21358.
10. O. Kareb, M. Aïder, Quorum Sensing Circuits in the Communicating Mechanisms of Bacteria and Its Implication in the Biosynthesis of Bacteriocins by Lactic Acid Bacteria: a Review. *Probiotics Antimicrob. Proteins*. 2020. **12**, 5–17.
11. A. Butler, M. Sandy, Mechanistic considerations of halogenating enzymes. *Nat. 2009 4607257*. 2009. **460**, 848–854.

3 Morphology Regulated Oxidative Bromination of Thymol with CeO_{2-x} Nanocrystal Enzyme Mimics

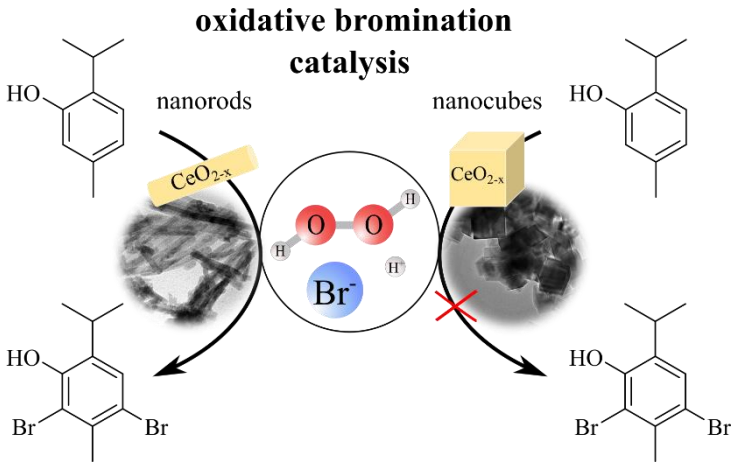

Author Contributions:

Olga Jegel:	Concept development, nanoparticle synthesis, TEM images, ζ-potential and ^{1}H-NMR measurement, manuscript preparation, figure preparation.
XXX:	Concept development, nanoparticle synthesis, TEM and BET surface are measurement, ^{1}H-NMR measurement, manuscript preparation, figure preparation.
XXX:	^{31}P NMR measurement, manuscript correction.
XXX:	PXRD refinements.
XXX:	Deconvolution of ^{31}P-NMR data.
XXX:	HRTEM measurement.
XXX:	HRTEM measurement
XXX:	Raman measurement.
XXX:	XPS measurement.
XXX:	Manuscript correction and scientific supervision.

3.1. Summary

It is already known that CeO_2 can mimic the enzyme vanadium haloperoxidase. Due to the presence of H_2O_2 and a halide anion, it is potentially able to oxidatively brominate organic compounds. In this chapter, we investigated whether oxidative bromination can be transferred to the natural monoterpenoid phenol derivate thymol (2-isopropyl-5-methylphenol) and what influences the morphology of CeO_2 nanoparticles has on the reaction rate.

For this purpose, three different morphologies of CeO_2 nanoparticles were considered: nanorods, nanospheres, and nanocubes. These were utilized as catalysts, in the presence of H_2O_2, Br^- and $HClO_4$, for the oxidative bromination of thymol. It was demonstrated that the different morphologies exhibited different catalytic activities, which was investigated by ^{1}H-NMR spectroscopy. Here, the nanorods showed that thymol was completely monobrominated after only three minutes and the reaction continued directly with dibromination. The nanospheres, on the other hand, reacted slightly slower and the reaction to the dibrominated product also occurred with a certain delay. The nanocubes barely showed any activity to oxidative bromination. After 30 min the reactant was still not completely transformed.

To identify the reason for the different reaction rates, the surface of the nanoparticles was investigated in more detail. Therefore, the BET specific surface area (S_{BET}), zeta potential (ζ –potential) and Lewis acidity were investigated. For the Lewis acidity the molecule trimethylphosphine (TMP) was adsorbed on the surface of the nanoparticles and the shift of the ^{31}P signal was measured with solid state NMR. This revealed the following trend: nanorods (highest acidity) > nanospheres (intermediate acidity) > nanocubes (lowest acidity).

Since it is assumed that a surface peroxido or hydroperoxido ligand is binding to the CeO_2 facets, this peroxido complex was investigated in more detail by adding H_2O_2 to the nanoparticles by Raman spectroscopy. Significant differences in the various morphologies were also obtained here. Nanocubes completely degraded the peroxido ligand after 15 minutes, whereas in the case of nanorods the ligand remained stable on the surface.

Also crucial was that X-ray photoelectron spectroscopy (XPS)-, high-resolution transmission (HRTEM)-, Raman- and Powder X-ray Diffraction (PXRD) data showed that nanorods exhibit the highest defect density, indicating a more frequent occurrence of Ce^{3+} on the surface than for nanospheres or nanocubes.

In general, it was confirmed that a high BET surface, a highly positive ζ –potential, a high Lewis acidity, and surface defects greatly benefit rapid oxidative bromination and increase the reaction rate.

3.2. Introduction

Halogenated organic compounds are important intermediates in chemical[1], pharmaceutical[2], or agrochemical[3] research, because the carbon-halogen bond is susceptible to nucleophilic substitution, which increases biological activity and bioavailability of the corresponding compounds[4] or enables metal-catalyzed cross-coupling reactions[5]. While traditional chemical halogenation methods employ highly reactive reagents and generate harmful waste. Nature has evolved a variety of enzymes that halogenate their substrates with Cl^-, Br^-, I^- or even F^- anions and oxygen or peroxide at room temperature in aqueous solution[6]. Therefore, these halogenating enzymes, halogenases and haloperoxidases[7,8], are attractive synthetic tools, because their reactions are regioselective and may address even electronically disfavoured positions. A number of transition metal complexes[9,10], V_2O_5[11] and molybdate anions[12] can act as functional mimics of haloperoxidases ("nanozymes").[13,14] Although enzymatic oxidative halogenation (via vanadium bromoperoxidases[15,16]) is well explored, mechanistic information on solid state biomimetic models is scarce. The catalytic effect of V-dependent haloperoxidases related to the formation of a vanadium–peroxido species at the active site through reaction with hydrogen peroxide[17], which is a stronger oxidant than H_2O_2 itself. The final product is formed from a hypobromite intermediate by reaction with an organic substrate. Alternatively, reaction with another oxidant molecule leads to its decomposition accompanied by singlet dioxygen formation.[18] Molecular complexes have been reported to form high-valent metal–oxo/peroxido intermediates.[19–22] Likewise, V_2O_5 nanoparticles[23,24] form surface-peroxido species, but they leach with time due to the formation of soluble polyoxovanadates.[25]

Ceria nanoparticles are an efficient functional mimics of haloperoxidases as well.[26] The formation of stable hydroperoxo/peroxo surface species[26,27] enables the reduction of unwanted reactive oxygen species in biological systems,[28] which make ceria nanoparticles very active functional mimics of peroxidases[29–31] and haloperoxidases.[32] Since ceria is highly insoluble ($K_L = 10^{-60}\ mol^3 \cdot L^{-3}$),[33] non-leaching,[34,35] and chemically stable over a wide temperature and pH range (pH 1-13)[34]. It has improved storage and operational stability towards denaturation by heat, organic solvents, and autoproteolysis compared to natural or recombinant enzymes. Moreover, ceria has low production costs, high catalyst productivities and it is easy to recover and recycle.

Since cerium is redox active and can cycle between its tetra- and trivalent states ($E° = 1.72$ V).[36] Ceria is non-stoichiometric (CeO_{2-x}) with oxygen vacancies.[37] Its success in

chemical reactions (e.g. for HCl oxidation in a Deaconprocess in order to recover Cl_2)[38] is connected not only to these unique redox and structural properties associated with oxygen diffusion and oxygen storage/release capacity, but also to its acid/base properties.[37,39] In nanocrystals, the oxygen vacancies may cluster at the particle surface, [40,41] because the ionic radius of Ce^{3+} (128 pm)[42] is more compatible with the undercoordinated surface positions than the 8-fold coordinated positions of Ce^{4+} (115 pm) in the CeO_{2-x} structure.[26,43]

While the haloperoxidase properties of nanoceria are promising, the design rules for developing nanocatalysts with optimal halogenating properties are not yet defined. Nanoparticle powders typically expose a range of surfaces with different defect sites, predominantly low-index surfaces with low surface energies. CeO_{2-x} particles with specific morphologies have been employed before to study the structure sensitivity of catalytic reactions experimentally[44–46] or theoretically[47], but most studies were carried out at high temperatures in the gas phase.[48] In aqueous environment the stability and reactivity of ceria nanoparticles may change significantly, because ion charges and solvation effects at the metal oxide/water interface come into play.[49,50] The aim of the this work is to directly compare the morphology-dependent oxidative bromination reaction catalyzed by CeO_{2-x} nanoparticles with thymol, a monoterpenoid phenolic compound, as model substrate. To investigate the impact of morphology in terms of BET surface area (S_{BET}), ζ-potential and haloperoxidase activity of CeO_{2-x}, we employed CeO_{2-x} particles with defined diameters and morphologies (spheres, cubes, rods).[51] The structures of the different morphologies are related with the surface acid/base properties (or the resulting surface charge), which are essential for the formation of surface hydroperoxo groups and the reaction with negatively charged halide species in aqueous solution.[52,53] The Lewis acidity of the surface was investigated with trimethylphosphine (TMP) as ^{31}P nuclear magnetic resonance (NMR) probe.[54]

CeO_{2-x} nanorods displayed the highest performance towards bromination of thymol. Catalytic activity for the three morphologies were separated from the impact of active surface area and surface charge (ζ-potential) by determining the BET surface areas (S_{BET}) by nitrogen physisorption and the ζ-potential by light scattering. In essence, the maximum activity is related to the interplay of the acidity,ζ-potentia and the S_{BET} of the CeO_{2-x} nanocrystals.

3.3. Results and Discussions

TEM/XRD characterization. Ceria nanoparticles were synthesized as described before. Ceria nanorods and cubes were prepared hydrothermally using different NaOH concentrations (rods 4 M, cubes 19 M).[55–57] Spherical ceria particles were prepared by sol-gel chemistry using citric acid as ligand with an average size of 6-7 nm were synthesized by sol-gel chemistry.[58] Phase composition, morphology and size were determined by powder X-ray diffraction and transmission electron microscopy (TEM), respectively. (Figure 3.1., Figure S3.1B)

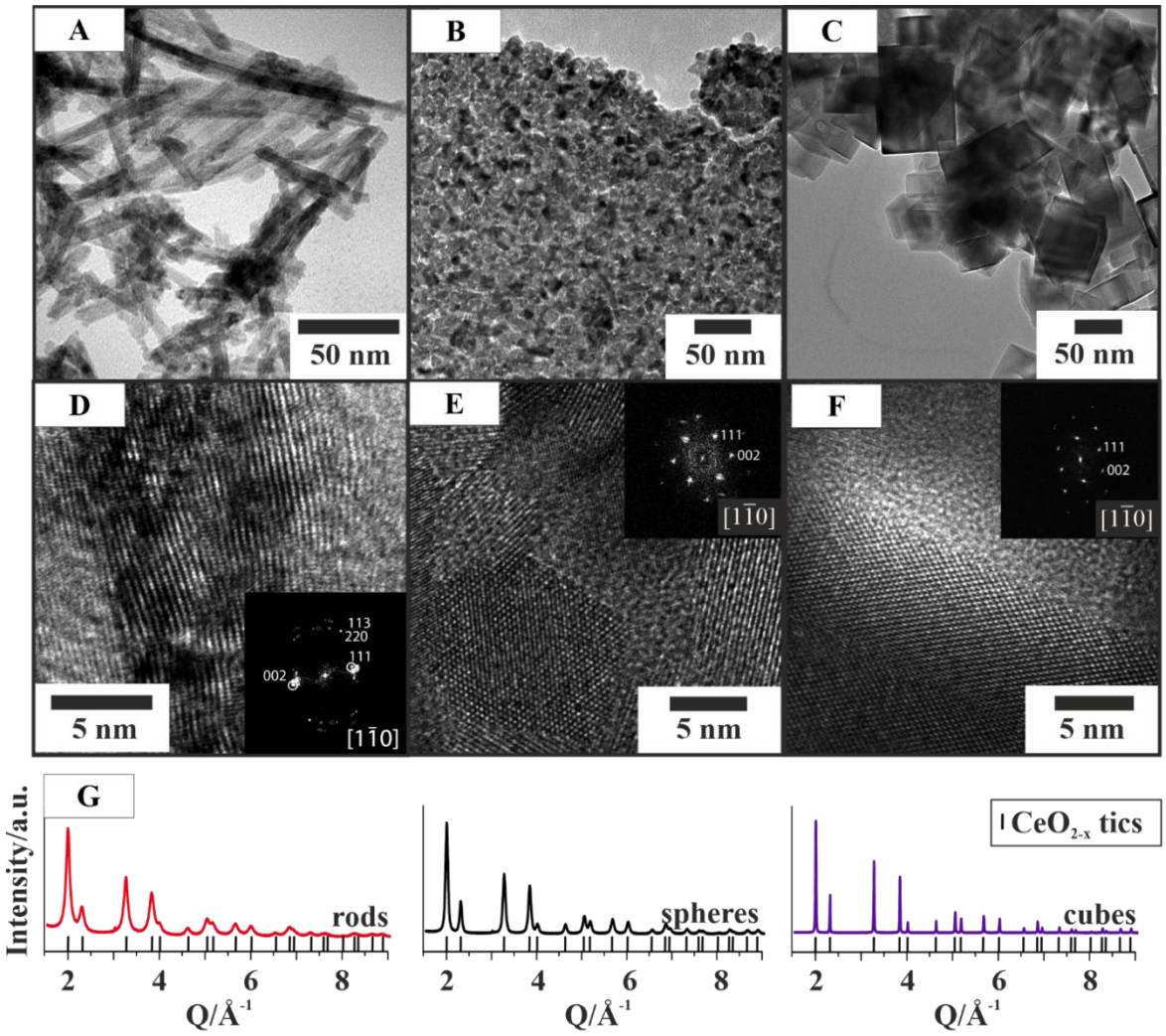

Figure 3.1. TEM (A-C) and high resolution (HR)TEM (D-F) images of CeO_{2-x} nanoparticles with fast Fourier transform (FFT). (A, D) nanorods, (B, E) nanospheres, (C, F) nanocubes. (G) Experimental X-ray powder of CeO_{2-x} nanorods (red line), nanospheres (black line) and nanocubes (purple line). Ticks indicate theoretical positions of Bragg intensities.

Figure 3.1A+D shows TEM images of CeO_{2-x} nanorods. The nanorods have an uniform width (5-7 nm) and a broad length distribution (40-200 nm) (Figure S3.1C+D). Increasing

the NaOH concentration leads to the formation of well-defined cubes with average sizes of 35 nm. (Figure 3.1C, Figure S3.1A) Spherical CeO_{2-x} particles (Figure 3.1B, HRTEM images of all CeO_{2-x} morphologies reveal a crystal orientation along the $[1\bar{1}0]$ zone axis (Figure 3.1D-F). According to the corresponding fast Fourier transform (FFT) pattern, two sets of diffractive dots can be observed for nanocubes and nanospheres, which are attributed to (111) and (002) planes. However, the FFT pattern of nanorods demonstrate a polycrystalline structure with additional (113) and (220) planes. The polycrystinallity of the nanorods is also confirmed by Rietveld refinements. The powder diffraction patterns in Figure 3.1G show that all ceria particles crystallize in the cerianite phase with the space group ($Fm\bar{3}m$) which is related to the typical calcium fluoride (CaF_2) structure. Rietveld refined power diffraction patterns are demonstrated in Figure S3.6. The reflection half widths in the PXRD pattern of the nanocubes are very narrow, indicating high crystallinity, lower defect density and larger crystal domains. The reflections of the pattern of CeO_{2-x} spheres are broader due to the small crystallite sizes. The strong reflection broadening of the nanorods are attributed to internal pores and surface defects such as vacancy clusters, pits, and a high degree of surface roughness.[59–61]

Determination of Lewis acidity using TMP. Quantum chemical calculations at various theory levels suggested that the catalytic HOBr formation cycle starts by binding a surface peroxido or hydroperoxido ligand to the CeO_{2-x} facets *via* exchange of a surface-bound water molecule. With a Gibbs free energy change ($\Delta G°$) close to zero this exchange was predicted to be unlikely (for typical H_2O_2 concentrations), but to become favorable ($\Delta G°<0$) for a dissociation of H_2O_2 accompanied by a transfer of an oxygen atom to a bromide anion (or HBr molecule) and its subsequent desorption.[26]

Neither a replacement of the water ligand nor an oxygen transfer reaction require a redox activity of Ce, and the haloperoxidase reaction is likely to be dictated by the Lewis acidity of the CeO_{2-x} surfaces. Therefore, the three different CeO_{2-x} nanocrystals were compared with respect to their Lewis acidity, ζ-potential and S_{BET}. ^{31}P solid state NMR spectroscopy was used to study the Lewis acidity of the (amorphous oxygen) deficient CeO_{2-x} surface layer of the ceria nanoparticles with different morphology using a known procedure.[53] The method relies on the dependence of the ^{31}P chemical shift on the different binding strength of the trimethylphosphine (TMP) phosphorous on the ceria surface. When a complex between TMP and a Bronsted acidic proton from a hydroxyl surface group is formed, ^{31}P shifts result in a relatively narrow spectral range of a few ppm – from -3 to -5 ppm.[62] This

hardly allows a direct correlation between the chemical shift and the different morphologies. However, chemisorbed TMP on the ceria surface acts as a Lewis base donating the phosphorous unpaired electron pair to the cerium cations. Their Lewis acidity varies significantly depending on the morphology. The ^{31}P chemical shifts are detected in the range of -20 ppm to -60 ppm for the different cerium oxide morphologies which facilitates their differentiation. Less acidic Ce cations bind only weakly to TMP.[62] At the same time, more acidic Ce cations are capable of forming stronger bonds, which leads to a reduction in the TMP-Ce bond length. Consequently, the phosphorous is more deshielded and the ^{31}P resonance shifts downfield. Figure 3.2 presents the deconvoluted ^{31}P solid state NMR spectra of TMP bound to CeO_{2-x} nanocrystals with different morphologies. The corresponding ^{31}P NMR spectra show different ^{31}P-NMR shifts indicating Ce sites with Lewis acidities in the order −31.6 ppm (rods, highest acidity) > −41.3 ppm (spheres, intermediate acidity) > −61.5 ppm (cubes, lowest acidity). ^{31}P-NMR spectra of CeO_{2-x} nanocubes show a sharp resonance at -61.5 ppm with a full width of half maximum (fwhm) of 0.183 kHz (1.1 ppm) indicating only a single type of site with low Lewis acidity and uniform size distribution. This is compatible with the results of powder X-ray diffraction and TEM, the cube-like nanocrystals showed high crystallinity.

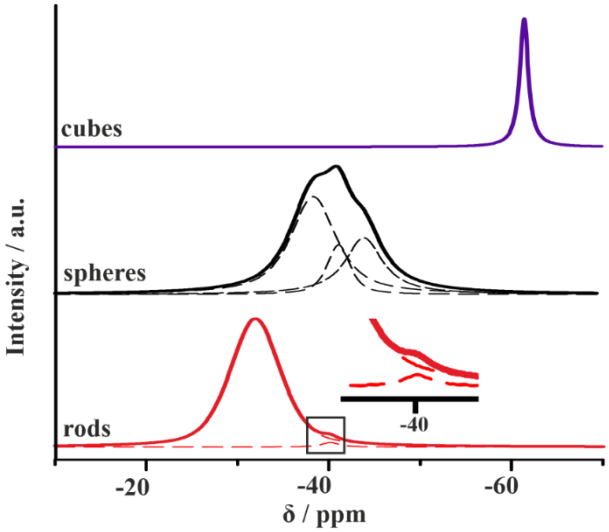

Figure 3.2. TMP ^{31}P-NMR spectra for different CeO_{2-x} morphologies.

The ^{31}P-NMR spectrum of the spherical nanoparticles shows a complex signal, which after deconvolution splits into three different resonances respectively at -44.2ppm (0.809 kHz, 5 ppm) , -41.4 ppm (0.485 kHz, 3 ppm) and -38.6 ppm (0.971 kHz, 6 ppm) with an integral ratio of 4:1:2. This indicates the presence of three distinguishable sites within a narrow ppm

range and Lewis acidities of comparable strength, compatible with a poorly ordered or disordered surface.[53] No well-ordered crystallite surface is formed, because of the small crystallite size and the large surface/volume ratio (0.44 nm^{-1}). Thus, different sites with comparable Lewis acidity remain. Two resonances are observed in the ^{31}P NMR spectrum of the rods: a dominant signal at -31.9 ppm (1.054 kHz, 6.5 ppm) and a low intensity peak at -40.1 ppm (0.347 kHz, 2.1 ppm) with an integral ratio of 1:0.015. The latter is comparable with the spheres signal indicating a disordered surface within the rods, which is in harmony with Raman, PXRD, HRTEM and XPS data revealing a high defect density for nanorods.

Effect of ζ-potential and S_{BET}. ζ –potential (zeta potential) measurements are an analytical method to determine surface potential of nanoparticles in a colloidal systems. The surface charge has an influence on i) the stability of a colloidal system and ii) the catalytic behaviour due to electrostatic attraction or repulsion forces between substrate and the catalyst surface. It is known that fluoride ion addition causes a negative ζ –potential at CeO_{2-x} surfaces, accelerating peroxidase reaction, since there is an electrostatic attraction between the substrate TMB (positive) and catalysts surface.[63] Surface charge is likely to play a crucial role in ceria-catalyzed oxidative bromination reactions in solution, because a negatively charged halide anion must adsorb to the catalyst surface. Surface charge is an integral characteristic of the surface acidity because it is the sum of all acidic (as determined by ^{31}P NMR) and basic surface groups on the surface. Therefore, the effect of ζ-potential and S_{BET} on the reaction rate were determined.

The ζ-potential was determined in acidic medium ($HClO_4$ addition, pH=1) to mimic the conditions of thymol bromination.[64] For nanospheres and nanorods ζ-potentials of +31 mV and +25.4 mV were measured, which are in a similar range. Ceria nanocubes showed the distinctly lowest ζ-potential with +11.8 mV. The S_{BET} surface area for CeO_{2-x} nanorods was determined by N_2 sorption as 98.4 m^2g^{-1}, the S_{BET} surface areas for nanospheres and -cubes were considerably smaller (44.6 m^2g^{-1} and 16.1 m^2g^{-1}). Since catalytic activity depends on both factors i) ζ-potential and ii) S_{BET}, a product of both is formed taking these factors into account. S_{BET} and ζ-potential product thus represents the surface charge with the highest accessible surface area.[43] . Table 3.1 shows an overview of ζ-potential, S_{BET} and the product of S_{BET} and ζ-potential for all three morphologies.

Table 3.1. ζ-potential, S_{BET} and the product of S_{BET} and ζ-potential for CeO_{2-x} nanorods, spheres and cubes.

morphology	**S_{BET} / m^2g^{-1}**	**ζ-potential / mV**	**S_{BET} · ζ-potential / m^2g^{-1}**
rods	98.4	25.4 ± 0.6	2500 ± 40
spheres	44.6	31.0 ± 1.0	1383 ± 45
cubes	16.1	11.8 ± 0.7	190 ± 11

Peroxido complex on ceria surface. The binding of H_2O_2 to ceria surfaces is likely to be an initial step for the oxidative halogenation reaction. H_2O_2 is known to bind to nanoceria surfaces which catalyze its decomposition to water and oxygen (peroxidase reaction).[28] In a second step, bromide anions have to approach or adsorb to the CeO_{2-x} nanocrystal surface to form hypohalite species. Reactive oxygen intermediates resulting from the reaction of H_2O_2 with ceria nano-powders and the oxidation of organic compounds by a CeO_{2-x}/H_2O_2 system have been studied based on the competitive binding of organic dyes and hydrogen peroxide to Ce surface sites and the subsequent degradation of the organics by pre-formed peroxo species.[65,66]

The binding of H_2O_2 to the facets of ceria nanocrystals give rise to Raman absorption bands.[65,67] (Figure 3.3) 2 µL of H_2O_2 (35%) was added to the nanoparticles and spectra were recorded for 5 min each over a period of 20 min. After H_2O_2 addition an orange powder was obtained. The Raman spectra show a new vibrational band at 840 cm^{-1},which is in harmony with Raman bands for cerium peroxo species at 842 cm^{-1} and 839 cm^{-1}.[65,68,69] CeO_{2-x} nanocrystals are yellow colored. Binding of H_2O_2 causes a color change from light yellow to dark orange-brow, which is associated with a ligand to metal charge transfer (LMCT) and deepens for increasing H_2O_2 concentration.[70] Figure 3.3 shows an image of CeO_{2-x} nanopowder (nanorods, nanospheres, nanocubes) after adding H_2O_2 (c = 11 M). A significant difference between the peroxo band of different morphologies can be observed. The CeO_{2-x} nanorods show no change in signal at 840 cm^{-1} after 20 min. A clear signal can also be detected after 24 h. Spherical particles show a much weaker peroxide signal that decreases with time. The lowest signal is displayed by the cubes, with the signal disappearing completely after 20 min. Coherently, it can be concluded that the persistence of the peroxo complex has a correlation with the rate constant of thymol bromination. Our hypothesis is that the formation of the peroxo complex on the surface is essential for HOBr formation, and the peroxo complex is a key factor for the catalysis.

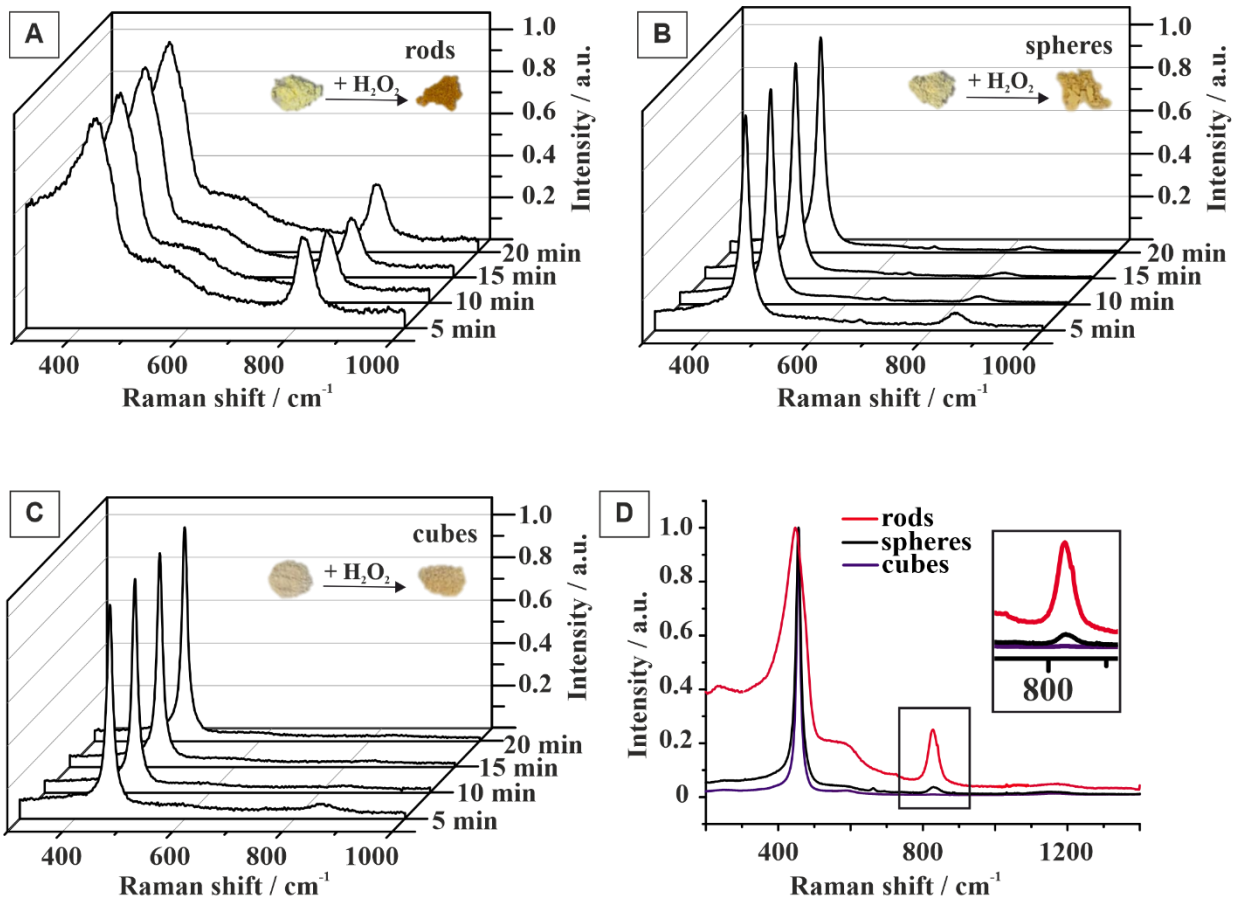

Figure 3.3. Raman spectra of CeO_{2-x} (A)-nanorods, (B) -nanospheres and (C) -nanocubes after H_2O_2 (35%) addition recorded every 5 min over a period of 20 min with a corresponding image of the particles before and after H_2O_2 addition. (D) shows a Raman spectra 24 h after H_2O_2 addition with a zoom in to 800-900 nm.

An additionally difference exhibits the spectrum of the rods with the signal at 595 cm^{-1}, which is assigned to Frenkel-type oxygen vacancies.[71] This is an evidence that the rods have more defects than spheres or cubes and thus the defects have an important influence on the catalytic rate. Moreover, HRTEM images confirm this result and show the presence of line defects (Figure S3.2). All spectra demonstrate a triply degenerate active band at 464 cm^{-1} (F_{2g} band). This band is associated with the stretching of the Ce-O band.[72] The signal of the spheres and the cubes is a sharp signal, which indicates a higher crystallinity in the lattice. However, the rods demonstrate a broad signal, which is induced by a disorder in the lattice which is caused by the presence of defects.[73] The higher defect concentration located in CeO_{2-x} nanorods is in harmony with the measured XPS spectra shown in Figure S3.14. As expected from the ionic radii of Ce^{4+} and Ce^{3+}, Ce^{3+} predominantly occurs at the particle surface in association with oxygen defects. The XPS survey spectra (Figure S3.13) of CeO_{2-x} nanorods, -spehres and –cubes confirm the presence of the elements Ce and O.

Michaelis−Menten kinetic studies can also regard the affinity of H_2O_2 to different CeO_{2-x} morphologies[53] indicate that the affinities (and stabilities) of H_2O_2 based on the Michaelis constants (K_m)[74] behave in the order: cubes (K_m=n.a.) < spheres (K_m=750 μM) < rods (K_m=330 μM). Here, the affinity is reciprocal to the Michaelis Menten constant K_m. No Michaelis Menten kinetics could be calculated for the cubes, since no reaction occurred. (Figure S3.7) However, Ce promotes H_2O_2 reduction (peroxidase reaction) in the reverse order because Ce with lower acidity (or higher electron density) can reduce H_2O_2 easier.

Bromination of thymol. Nanozymes are known for their low cost of manufacture, high stability and robust catalytic activity[75] thus being an excellent alternative to natural enzymes. The catalytic activity of the ceria nanoparticles with defined diameters and morphologies (spheres, cubes, rods) was investigated by *in situ* monitoring a model reaction, the oxidative halogenation of the phenolic monoterpene thymol, using ^{1}H NMR spectroscopy.[76,16]

A reaction mixture consisting of thymol, KBr, $HClO_4$ and the cerium oxide nanoparticles with different morphologies (rods, cubes and spheres) in D_2O/CD_3OD (10% v/v) was prepared and examined via ^{1}H NMR spectroscopy after H_2O_2 addition. An excess of bromide was added and not only the monobrominated product (4-bromotyhmol) but also, depending on the particle morphologie, the dibrominated product (2,4-dibromothymol) could be formed. For kinetic analysis, the progress of the reactions was followed in-situ by ^{1}H-NMR spectroscopy after adding H_2O_2. The reaction was monitored minutewise for a period of 30 minutes (Figure S3.3, 3.4, 3.5) following the development of the aromatic proton resonances in the spectral range between 6.8 and 7.3 ppm. Stacked spectra of the reaction catalyzed by CeO_{2-x} nanorods are shown in Figure 3.4A. All signals were normalized to the signals of the isopropyl group (at ~1 ppm). The doublett at 6.9 ppm corresponds to the aromatic proton of thymol (Figure 3.4A+D: red circle). Already in one minute its intensity decreases to 50% which is coupled with the appearance of a new resonance at 7.1 ppm. The latter corresponds to the proton of 4-bromothymol (Figure 3.4A+D: blue circle) which is formed as a result of the first bromination step. The signal at 7.2 ppm results from the proton of dibrominated product (Figure 3.4A+D: cyan circle) 2,4-dibromothymol, which is formed already 2 minutes after H_2O_2 addition. Bromination can be followed based on the change of integrals of aromatic protons highlighted in red, blue and cyan in Figure 3.4B. A fast exponential intensity decrease of the thymol 6.9 ppm (red) doublet is observed in the first 3 minutes with a complete transformation within 8 minutes, whereas the signal at 7.1 ppm (blue) for the 4-

bromothymol increases exponentially up to a maximum. An additional signal appears after 2 minutes at 7.2 ppm, which is associated with 2,4-dibromothymol (cyan). An equilibrium between the mono- and di-brominated thymol is reached after 8 min with a respective integral ratio of 1:1.34. The NMR signals were assigned unambiguously from the 2D ^{1}H COSY NMR spectra (Figure S 3.8, 3.9, 3.10) where cross signals due to the coupling between the aliphatic protons appear. No such cross signals between the two aromatic singlets (i.e. the aromatic protons are in *para* position to each other) are detected. Experimental details are presented in the Supporting Information.

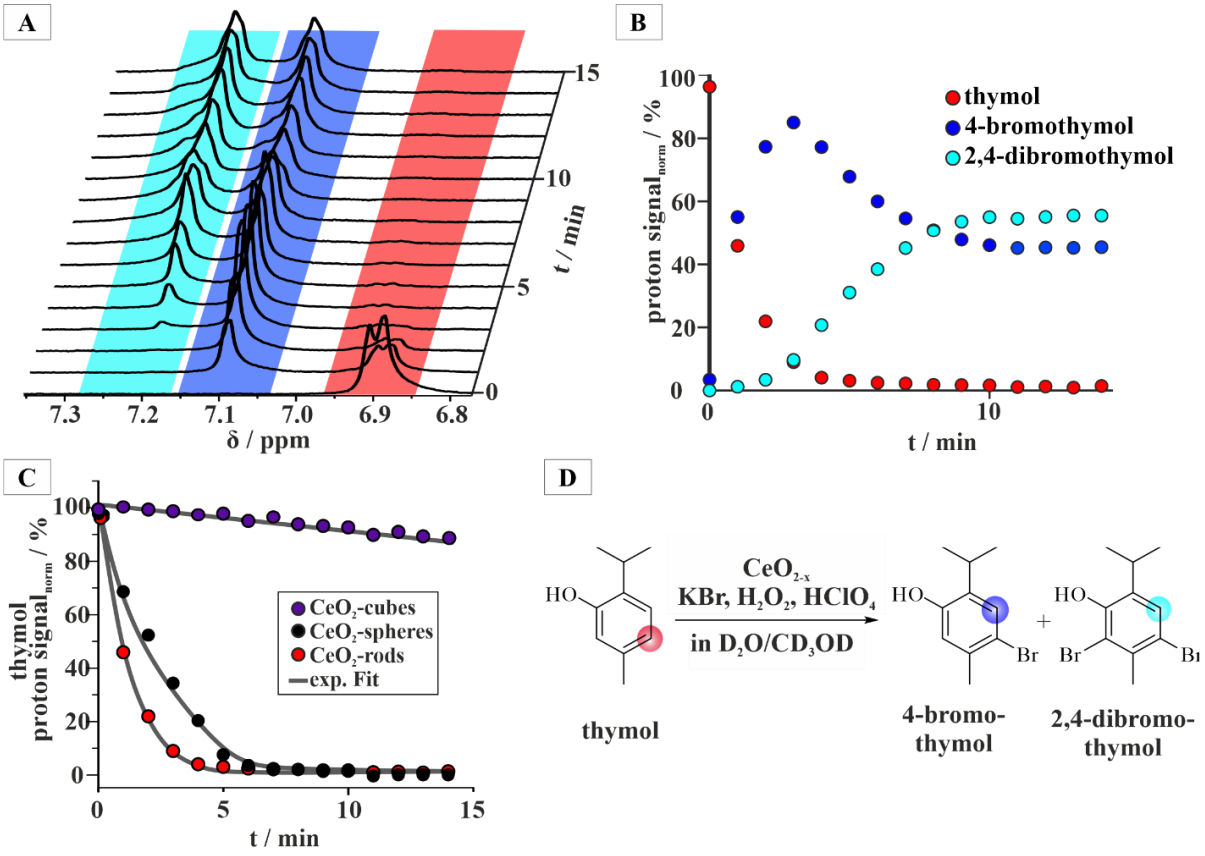

Figure 3.4. (A) Stacked ^{1}H-NMR spectra of thymol (cyan), 4-bromothymol (blue) and 2,4-dibromothymol (red) for the bromination of thymol with CeO_{2-x} nanorod catalyst. (B) Time-dependent change in proton signal intensities for thymol (red), 4-bromothymol (blue) and 2,4-dibromothymol (cyan). (C) Conversion of thymol for bromination using CeO_{2-x} nanocubes (gray), nanospheres (black) and nanorods (red) as catalyst over a period of 15 min. (D) Oxidative bromination of thymol via a 4-bromothymol intermediate to 2,4-dibromothymol as final product.

CeO_{2-x} nanospheres also catalyse the bromination reaction, however more slowly. The equilibrium between the mono- and dibrominated product is reached after ca. 15 minutes with an end integral ratio between both of 1:1. The thymol bromination catalyzed by CeO_{2-x} nanocubes results in the formation of only the monobrominated product. Furthermore, 80%

of the original thymol remains unreacted after 30 minutes. Figure 3.4C shows the intensity changes of the aromatic protons of thymol for different CeO_{2-x} catalyst morphologies. The decrease of the proton signals is faster for the nanorods (rate constant $k_{rods}=772\cdot10^{-3}\pm19\cdot10^{-3}$ min^{-1}) than for the nanospheres ($k_{spheres}=396\cdot10^{-3}\pm10\cdot10^{-3}$ min^{-1}). Virtually no reaction (i.e. no change of the signal intensities with $k_{cubes}=9.6\cdot10^{-3}\pm0.1\cdot10^{-3}$ min^{-1}) was observed for CeO_{2-x} nanocubes. A first-order pseudokinetic model was used to compare the conversion rates of thymol (equation 3.1) where "a(t)" indicates the thymol concentration at time *t* and a_0 set to 1. Figure S 3.3, 3.4, 3.5, 3.15 shows the ^1H NMR spectra for the reaction products in the absence and the presence of the CeO_{2-x} nanocrystals.

$$a(t) = a_0 e^{-k_a \cdot t} \tag{3.1}$$

In order to explain the different reaction rates of the CeO_{2-x} morphologies, the lewis acidity and the product of surface area and ζ-potential were compared in the following. Figure 3.5 shows that reaction velocity scales with i) lewis acidity (Figure 3.5A) and ii) $S_{BET}\cdot\zeta$-potential (Figure 3.5B) of the nanoparticles in the order rods > spheres > cubes. In essence, the Lewis acidities of the CeO_{2-x} nanocrystals dictate the bromination rate of thymol: The higher the Lewis acidity, the faster the observed bromination rate. A key feature of oxidative halogenation reactions in aqueous environments is that chemical transformations are sensitive toward changes in solvation. High Lewis acidity will allow a polar molecules or ion species (like H_2O_2 or halide anions) to replace solvent molecules at nanocrystal surfaces.

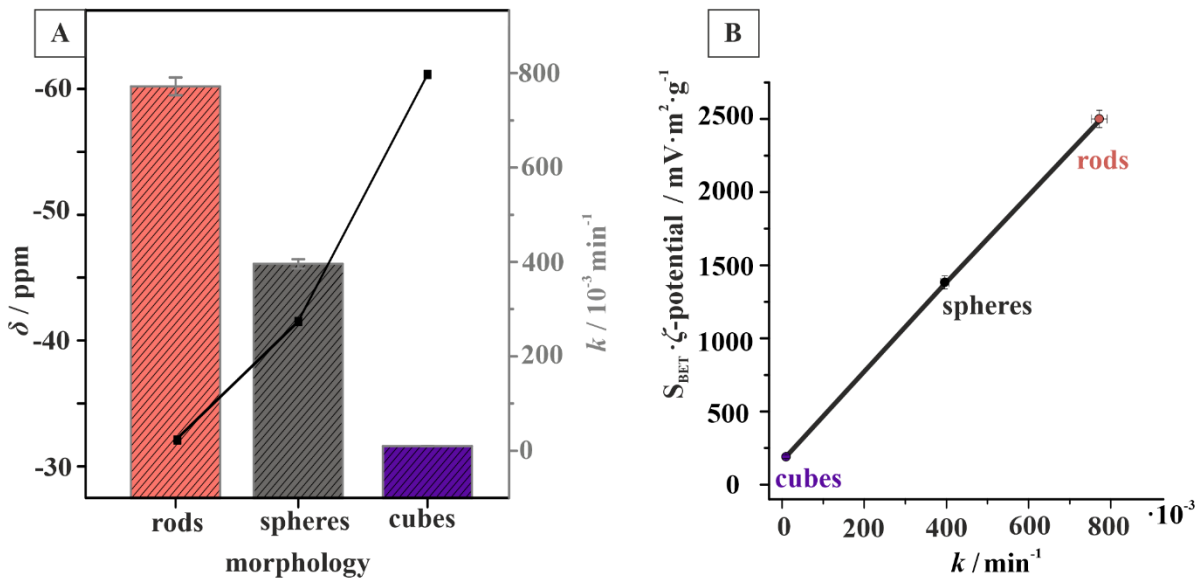

Figure 3.5. (A) Reaction velocity (*k*) scaled with Lewis acidy of different CeO_{2-x} morphologies. (B) Linear impact of S_{BET} ·ζ-potential on *k* for three different morphologies.

The experimental results allow sketching a mechanism of the halogenation reaction. Halogenation catalysis by nanoceria requires: (i) the largest possible active surface, (ii) a rapid H_2O_2 binding (influenced by the surface acidity), (iii) sufficient stability of the Ce-O-O-H surface species with respect to the peroxidase reaction, and (iv) bromide adsorption to be sufficiently fast and strong to allow the transfer of an oxygen atom to bromide anion before a dioxygen molecule can be formed. Here, the surface i) lewis acidity and ii) S_{BET}·ζ-potential of the CeO_{2-x} nanocrystals will determine the rate of bromide adsorption.

In essence, the Lewis acidities of the CeO_{2-x} nanocrystals dictate the bromination rate of thymol: *The higher the Lewis acidity, the faster the observed bromination rate* (Figure 3.5A). A key feature of oxidative halogenation reactions in aqueous environments is that chemical transformations are sensitive toward changes in solvation. High Lewis acidity will allow a polar molecules or ion species (like H_2O_2 or halide anions) to replace solvent molecules at nanocrystal surfaces.

3.4. Experimental Section

MATERIAL AND SYNTHESIS

All commercial reagents and solvents were used as received, without further purification. Ceriumnitrate hexahydrate (99.5%) and Thymol (98+%) were obtained from Alfa Aeser. Potassium bromide (99+%) and Perchloric acid (ca.70% solution in water) were obtained from Acros Organics. Hydrogen peroxide (35%), Citric acid (<99.5%, anhydrous) were purchased from Carl Roth. Methanol-d_4 (99.8%) and Deuterium oxide (99.9%) were purchased from Deutero. Ammonium hydroxide (25%) was utilized from VWR, and Sodium hydroxide from Fisher Scientific. Trimethylphosphine (97%) were obtained from Sigma Aldrich. Ultrapure water (18.2 MΩ cm-1) was used for all experiments.

CeO_{2-x} Nanospheres.[77] 1.6 mL of an aqueous 1 M $Ce(NO_3)_3 \cdot 6H_2O$ solution and 3.2 mL of a 4 M aqueous solution of citric acid were put in a beaker and refilled with Milli-Q water to a total volume of 20 mL. After the resulting sol was stirred for 10 min, conc. ammonia solution was added until a pH of 8.5-9 was reached. Then, the solution was stirred for another 10 min and placed in the oven at 100°C overnight. The resulted gel was heated in an oven with a heat rate of 5°C/min to 550°C for 3 h. After cooling down the product was mortared and analyzed.

CeO_{2-x} Nanorods.[26] $Ce(NO_3)_3 \cdot 6H_2O$ (4,86 g, 11 mmol) was used as precursor for the synthesis of CeO_{2-x} nanorods and filled in a Teflon-lined autoclave. 210 mL of a 4 M aqueous NaOH solution were slowly dropped in the Teflon-inlay with the precursor while stirring. After finished addition, the solution was stirred for another 30 min and autoclaved in the autoclave at 80°C for 16 h. When the suspension was cooled down, the product was centrifuged for 10 min at 9000 rpm and washed with water six times (until the washing water was neutral). The yellow product was freez-dried in liquid nitrogen and vacuum dried.

CeO_{2-x} Nanocubes[57]. $Ce(NO_3)_3 \cdot 6H_2O$ (0.868 g, 2 mmol) and $NaNO_3$ (0.85 g, 1 mmol) were dissolved in 10 mL Milli-Q water. 30 mL of an aqueous NaOH solution (50%) were added and stirred for 30 min. The solution was transferred into a Teflon inlay and heated in a microwave oven to 180°C for 120 min (heating rate 10°C/min). After cooling, the product was collected by centrifugation for 10 min at 9000 rpm, washed with water until the supernatant was neutral and dried in vacuum.

Bromination of Thymol. To investigate the oxidative bromination *via* ^{1}H-NMR spectroscopy a reaction medium consisting of nanoparticles (2.85 mg mL^{-1}), thymol (66 mM), KBr (142 mM), $HClO_4$ (91 mM) and H_2O_2 (266 mM) in CD_3OD was prepared.

Firstly, KBr and $HOCl_4$ were dissolved in a CD_3OD/D_2O mixture, and the resulting precipitate of $KClO_4$ was separated. Thymol and the CeO_{2-x} nanoparticles were added, followed by ultrasonification for 30 s. The first NMR spectrum was measured without H_2O_2. The catalysis was started by adding H_2O_2 to the tube. The first spectrum of the kinetic measurement was recorded after 1 min. The following spectra were recorded every minute. ^1H NMR (400 MHz,CD_3OD): 4-bromo-2-isopropyl-5-methylphenol (4-Bromthymol): δ[ppm] = 6.90 (d, *J* = 7.7 Hz, Ar-H), 6.55-6.42 (m, Ar-H), 3.13 (m, *J* = 7.0 Hz, Ar-CH-), 2.13 (s, Ar-CH_3), 1.10 (d, J=6.9 Hz, -$C(CH_3)_2$). 4,6-dibromo-2-isopropyl-5-methylphenol. δ[ppm] = 7.26 (s, Ar-H), 3.14 (m, Ar-CH-), 2.47 (s, Ar-CH_3), 1.16 (d, *J*=6.9 Hz,-$C(CH_3)_2$).

Michaelis Menten Kinetics. The Michaelis Menten kinetics was determined with various H_2O_2 concentrations. The kinetic analysis was performed at λ =592 nm, the absorbance maximum of Br_4PR. For each measurement, the same stock solution of PR (50µM) mixed with KBr (25mM) was used. After adding 62.5µL of nanoparticle suspension (1mg/mL), the reaction was left stirring (800 rpm) for 2 min for temperature equilibration (25°C). Prior to H_2O_2 addition the absorbance was set to zero. The kinetics were measured for 10 minutes. All data points were linearly fitted in the period of 1-10 minutes.

CHARACTERIZATION

Transmission Electron Microscopy. Samples for transmission electron microscopy (TEM) were prepared by placing a drop of dilute NP dispersion (1mg/mL) in Milliq-Q water on a carbon-coated copper grid. TEM images were obtained with a FEI Tecnai 12 TWIN LaB6 at 120 kV together with a Gatan US1000 CCD-camera (16-bit, 2048 x 2048 pixels) using the Gatan Digital Micrograph software.

Nuclear Magnetic Resonance (NMR) . All solution ^1H NMR spectra were recorded at 295 K on a Bruker Avance DRX 400 MHz spectrometer (Bruker Biospin GmbH, Rheinstetten, Germany) operating at a proton frequency of 400.31 MHz. A commercial Bruker 2 channel 5 mm inverse probe head was used. 8 scans were averaged witth a recycle delay of 28 s for the quantitative measurements.

Prior to all solid state NMR measurements, 200 mg CeO_{2-x} nanoparticles were heated in a ground glass vessel at 120°C under vacuum for 2 µL of trimethylphosphine (TMP) was added. TMP adsoption onto the particles´ surface was allowed for 20 minutes to reach equilibrium. The sample was transferred into a solid state NMR rotor. Solid state ^{31}P NMR spectra were recorded on a Bruker Avance DSX 400 MHz spectrometer operating at a ^1H

and ^{31}P frequencies of 399.87 and 161.87 MHz respectively. A commercial 3 channel Bruker 4 mm probe head was used at a magic angle spinning (MAS) of 10 kHz. The quantitative ^{31}P experiments were conducted using a 30° flip angle pulse and averaging 64 scans with a recycle delay of 15 s with inverse-gated proton decoupling.Two-pulse phase modulation decoupling scheme was used for the experiments.No correction for the frictional heating was conducted. The spectra were referenced to $NH_4H_2PO_4$ at 0.9 ppm as an external standard.

Powder X-ray Diffraction. X-ray diffraction patterns were recorded on a STOE Stadi P diffractometer equipped with a Dectris My-then 1k detector in transmission mode using Mo Kα1 radiation. Crystalline phases were identified according to the PDF–2 database using Bruker AXS EVA 10.0 software.

Zeta Potentials. ζ-potentials were measured on a Malvern Zetasizer Nano using disposable capillary cells (DTS1070) and single-use polystyrene cuvettes. Data analysis was performed with Malvern Zetasizer Software 8.01.4906.

BET Surface Area. BET measurements were conducted with 3P Micro 300 gas adsorption instrument using nitrogen as the analysis gas at 77.4 K. The software 3P Surface Area & Pore Size Analyzer System 10.03.02 was used to analyze the recorded data.

X-ray photoelectron spectroscopy (XPS). XPS measurements were carried out on an Axis Ultra DLD imaging photoelectron spectrometer. Measurements were carried out using the Hybrid mode with 10 mA and 15 kV at the Al anode. The analysis area was 700 μm × 300 μm (i.e., X-ray spot size). Survey spectra were measured at a pass energy of 80 eV and elemental spectra at 20 eV pass energy of the analyzer. All spectra were charge corrected to a binding energy of 284.8 eV for the C 1s line corresponding to adventitious aliphatic carbon. Measurements were analyzed using the CasaXPS software plotted with Origin 8.1.

Raman Spectroscopy. The Raman spectra were recorded with a Bruker Senterra Microscope and the *OPUS* software.

UV/Vis. An Agilent Cary 3500 spectrophotometer was used.

3.5. Conclusions

In summary, we have shown by a combination of electron microscopy, X-ray diffraction, ^{31}P and ^{1}H NMR, XPS, Raman spectroscopy and chemical reactivity of the CeO_{2-x} in oxidative halogenating depends on various factors. We employed CeO_{2-x} nanocrystals with well-defined diameters and morphologies (nanocubes, -spheres, -rods). The kinetics of the catalytic activity of CeO_{2-x} nanocrystals with cubic, rod like, and spherical morphologies was determined by ^{1}H NMR spectroscopy using thymol, a monoterpenoid phenolic compound, as a model substrate.

The acid-base properties of CeO_{2-x} nanocrystals (and thus the catalytic behavior in haloperoxidase chemistry) are related to its surface structure. The Lewis acidities, determined using TMP ^{31}P NMR, follow the order nanorods > nanospheres > nanocubes , i.e., the Lewis acidities of the CeO_{2-x} nanocrystals dictate the bromination rate of thymol. The higher the Lewis acidity, the faster the observed bromination rate. Since the haloperoxidase reaction involves the transfer of an oxygen atom from the surface-bound H_2O_2 oxidant to a bromide anion, surface charge (controlling bromide adsorption) and stability of the Ce-O-O-H species are essential. Multiplicative combination of two independent factors, ζ-potential and S_{BET} surface area, provides a reliable measure to describe the rate of the haloperoxidase reaction in the order nanorods > nanospheres > nanocubes. The surface charge is reflected by the S_{BET} ·ζ-potential, which scales the experimentally determined surface acidities for the three different nanocrystal morphologies, which follow the order nanorods > nanospheres > nanocubes. This is consistent with the sequence of surface acidities, H_2O_2 affinity, and reported stability of Ce-O-O-H surface species scaling in the order nanorods > nanospheres > nanocubes. Since the haloperoxidase reaction requires a cleavage of surface-bound O-O units, the peroxidase activity of nanoceria is relevant for the oxidation of bromide *via* transfer of an oxygen atom. CeO_{2-x} has been reported to promote H_2O_2 reduction (peroxidase reaction) with a concomitant release of an oxygen atom in the order nanocubes > nanorods > nanospheres. Thus, the haloperoxidase reaction on CeO_{2-x} is determined by the interplay of cleaving a surface-bound Ce-O-O-H group (peroxidase reaction) and the adsorption of a halide species to which the oxygen resulting from the peroxidase reaction is transferred. Our studies provide new insight into the halogenation catalysis of ceria nanocrystals in aqueous environment and show parallels between inorganic catalysis and enzyme-like activities of CeO_{2-x}. Our results show that an understanding of the surface chemistry of catalysts, including the chemical state and the

number of active sites is the key to unravel catalytic correlation. In view of the growing interest in the use of ceria as “nanozyme” and the lack of mechanistic understanding of its reactivity, our findings may provide guidance for the investigation of soluble nanoceria and for expanding the scope of its reactivity even beyond aqueous chemistry.

3.6. References

1. Y. Sasson, Formation of Carbon-Halogen Bonds (Cl, Br, I) . *PATAI's Chem. Funct. Groups*. 2009 (available at https://dokumen.tips/download/link/patais-chemistry-of-functional-groups-formation-of-carbon-halogen-bonds).
2. R. Wilcken, M. O. Zimmermann, A. Lange, A. C. Joerger, F. M. Boeckler, Principles and Applications of Halogen Bonding in Medicinal Chemistry and Chemical Biology. *J. Med. Chem.* 2013. **56**, 1363–1388.
3. P. Jeschke, Latest generation of halogen-containing pesticides. *Pest Manag. Sci.* 2017. **73**, 1053–1066.
4. G. W. Gribble, Biological Activity of Recently Discovered Halogenated Marine Natural Products. *Mar. Drugs*. 2015. **13**, 4044–4136.
5. S. Z. Tasker, E. A. Standley, T. F. Jamison, Recent advances in homogeneous nickel catalysis. *Nat.* 2014. **509**, 299–309.
6. D. S. Gkotsi, H. Ludewig, S. V. Sharma, J. A. Connolly, J. Dhaliwal, Y. Wang, W. P. Unsworth, R. J. K. Taylor, M. M. W. McLachlan, S. Shanahan, J. H. Naismith, R. J. M. Goss, A marine viral halogenase that iodinates diverse substrates. *Nat. Chem.* 2019. **11**, 1091–1097.
7. V. Weichold, D. Milbredt, K. H. Van Pée, Specific Enzymatic Halogenation-From the Discovery of Halogenated Enzymes to Their Applications In Vitro and In Vivo. *Angew. Chem. Int. Ed. Engl.* 2016. **55**, 6374–6389.
8. F. Hollmann, D. J. Opperman, C. E. Paul, Biocatalytic Reduction Reactions from a Chemist's Perspective. *Angew. Chemie Int. Ed.* 2021. **60**, 5644–5665.
9. V. Conte, B. Floris, Vanadium and molybdenum peroxides: synthesis and catalytic activity in oxidation reactions. *Dalt. Trans.* 2011. **40**, 1419–1436.
10. N. Madaan, N. R. Shiju, G. Rothenberg, Predicting the performance of oxidation catalysts using descriptor models. *Catal. Sci. Technol.* 2015. **6**, 125–133.
11. F. Natalio, R. André, A. F. Hartog, B. Stoll, K. P. Jochum, R. Wever, W. Tremel, Vanadium pentoxide nanoparticles mimic vanadium haloperoxidases and thwart biofilm formation. *Nat. Nanotechnol*. 2012. **7**, 530–535.
12. B. Sels, D. De Vos, M. Buntinx, F. Plerard, A. Kirsch-De Mesmaeker, P. Jacobs, Layered double hydroxides exchanged with tungstate as biomimetic catalysts for mild oxidative bromination. *Nat.* 1999. **400**, 855–857.
13. H. Wei, E. Wang, Nanomaterials with enzyme-like characteristics (nanozymes): next-generation artificial enzymes. *Chem. Soc. Rev.* 2013. **42**, 6060–6093.
14. K. Korschelt, M. N. Tahir, W. Tremel, A Step into the Future: Applications of Nanoparticle Enzyme Mimics. *Chem. – A Eur. J.* 2018. **24**, 9703–9713.
15. F. Sabuzi, E. Churakova, P. Galloni, R. Wever, F. Hollmann, B. Floris, V. Conte, Thymol Bromination – A Comparison between Enzymatic and Chemical Catalysis. *Eur. J. Inorg. Chem.* 2015. **2015**, 3519–3525.
16. G. T. Höfler, A. But, F. Hollmann, Haloperoxidases as catalysts in organic synthesis. *Org. Biomol. Chem.* 2019. **17**, 9267–9274.
17. E. de Boer, R. Wever, The reaction mechanism of the novel vanadium-bromoperoxidase. A steady-state kinetic analysis. *J. Biol. Chem.* 1988. **263**, 12326–12332.

18. R. R. Everett, H. S. Soedjak, A. Butler, Mechanism of dioxygen formation catalyzed by vanadium bromoperoxidase. Steady state kinetic analysis and comparison to the mechanism of bromination. *J. Biol. Chem.* 1990. **265**, 15671–15679.

19. W. Liu, X. Huang, M. J. Cheng, R. J. Nielsen, W. A. Goddard, J. T. Groves, Oxidative aliphatic C-H fluorination with fluoride ion catalyzed by a manganese porphyrin. *Science*. 2012. **337**, 1322–1325.

20. A. K. Vardhaman, P. Barman, S. Kumar, C. V. Sastri, D. Kumar, S. P. de Visser, Mechanistic insight into halide oxidation by non-heme iron complexes. Haloperoxidase versus halogenase activity. *Chem. Commun.* 2013. **49**, 10926–10928.

21. P. Galloni, M. Mancini, B. Floris, V. Conte, A sustainable two-phase procedure for V-catalyzed toluene oxidative bromination with H2O2 –KBr. *Dalt. Trans.* 2013. **42**, 11963–11970.

22. F. Würthner, M. Stolte, Naphthalene and perylene diimides for organic transistors. *Chem. Commun.* 2011. **47**, 5109–5115.

23. R. André, F. Natálio, M. Humanes, J. Leppin, K. Heinze, R. Wever, H. C. Schröder, W. E. G. Müller, W. Tremel, V2O5 Nanowires with an Intrinsic Peroxidase-Like Activity. *Adv. Funct. Mater.* 2011. **21**, 501–509.

24. C. Wu, X. Zhang, J. Dai, J. Yang, Z. Wu, S. Wei, Y. Xie, Direct hydrothermal synthesis of monoclinic VO2(M) single-domain nanorods on large scale displaying magnetocaloric effect. *J. Mater. Chem.* 2011. **21**, 4509–4517.

25. N. N. Greenwood, A. Earnshaw, *Chemistry of the Elements*.

26. K. Herget, P. Hubach, S. Pusch, P. Deglmann, H. Götz, T. E. Gorelik, ya A. Gural, F. Pfitzner, T. Link, S. Schenk, M. Panthöfer, V. Ksenofontov, U. Kolb, T. Opatz, R. André, W. Tremel, K. Herget, T. E. Gorelik, I. A. Gural, F. Pfitzner, M. Panthöfer, V. Ksenofontov, U. Kolb, W. Tremel, P. Hubach, R. André, S. Pusch, T. Opatz, P. Deglmann, S. Schenk, H. Götz, T. Link, Haloperoxidase Mimicry by CeO2−x Nanorods Combats Biofouling. *Adv. Mater.* 2017. **29**, 1603823.

27. K. Fuku, K. Sayama, Efficient oxidative hydrogen peroxide production and accumulation in photoelectrochemical water splitting using a tungsten trioxide/bismuth vanadate photoanode. *Chem. Commun.* 2016. **52**, 5406–5409.

28. A. Karakoti, S. Singh, J. M. Dowding, S. Seal, W. T. Self, Redox-active radical scavenging nanomaterials. *Chem. Soc. Rev.* 2010. **39**, 4422–4432.

29. C. Korsvik, S. Patil, S. Seal, W. T. Self, Superoxide dismutase mimetic properties exhibited by vacancy engineered ceria nanoparticles. *Chem. Commun.* 2007, 1056–1058.

30. T. Pirmohamed, J. M. Dowding, S. Singh, B. Wasserman, E. Heckert, A. S. Karakoti, J. E. S. King, S. Seal, W. T. Self, Nanoceria exhibit redox state-dependent catalase mimetic activity. *Chem. Commun.* 2010. **46**, 2736–2738.

31. C. K. Kim, T. Kim, I. Y. Choi, M. Soh, D. Kim, Y. J. Kim, H. Jang, H. S. Yang, J. Y. Kim, H. K. Park, S. P. Park, S. Park, T. Yu, B. W. Yoon, S. H. Lee, T. Hyeon, Ceria Nanoparticles that can Protect against Ischemic Stroke. *Angew. Chemie Int. Ed.* 2012. **51**, 11039–11043.

32. K. Herget, H. Frerichs, F. Pfitzner, M. N. Tahir, W. Tremel, Functional Enzyme Mimics for Oxidative Halogenation Reactions that Combat Biofilm Formation. *Adv. Mater.* 2018. **30**, 1707073.

33. T. V. Plakhova, A. Y. Romanchuk, S. N. Yakunin, T. Dumas, S. Demir, S. Wang, S. G.

Minasian, D. K. Shuh, T. Tyliszczak, A. A. Shiryaev, A. V. Egorov, V. K. Ivanov, S. N. Kalmykov, Solubility of nanocrystalline cerium dioxide: Experimental data and thermodynamic modeling. *J. Phys. Chem. C*. 2016. **120**, 22615–22626.

34. J. T. Dahle, K. Livi, Y. Arai, Effects of pH and phosphate on CeO2 nanoparticle dissolution. *Chemosphere*. 2015. **119**, 1365–1371.

35. B. Collin, M. Auffan, A. C. Johnson, I. Kaur, A. A. Keller, A. Lazareva, J. R. Lead, X. Ma, R. C. Merrifield, C. Svendsen, J. C. White, J. M. Unrine, Environmental release, fate and ecotoxicological effects of manufactured ceria nanomaterials. *Environ. Sci. Nano*. 2014. **1**, 533–548.

36. J. T. Dahle, Y. Arai, Environmental geochemistry of cerium: Applications and toxicology of cerium oxide nanoparticles. *Int. J. Environ. Res. Public Health*. 2015. **12**, 1253–1278.

37. T. Montini, M. Melchionna, M. Monai, P. Fornasiero, Fundamentals and Catalytic Applications of CeO2-Based Materials. *Chem. Rev.* 2016. **116**, 5987–6041.

38. C. Li, Y. Sun, I. Djerdj, P. Voepel, C. C. Sack, T. Weller, R. Ellinghaus, J. Sann, Y. Guo, B. M. Smarsly, H. Over, Shape-controlled CeO2 nanoparticles: Stability and activity in the catalyzed HCl oxidation reaction. *ACS Catal.* 2017. **7**, 6453–6463.

39. K. Korschelt, R. Schwidetzky, F. Pfitzner, J. Strugatchi, C. Schilling, M. Von Der Au, K. Kirchhoff, M. Panthöfer, I. Lieberwirth, M. N. Tahir, C. Hess, B. Meermann, W. Tremel, CeO2−x nanorods with intrinsic urease-like activity. *Nanoscale*. 2018. **10**, 13074–13082.

40. C. T. Campbell, C. H. F. Peden, Oxygen vacancies and catalysis on ceria surfaces. *Science.* 2005. **309**, 713–714.

41. F. Esch, S. Fabris, L. Zhou, T. Montini, C. Africh, P. Fornasiero, G. Comelli, R. Rosei, Chemistry: Electron localization determines defect formation on ceria substrates. *Science (80-.).* 2005. **309**, 752–755.

42. R. D. Shannon, Revised effective ionic radii and systematic studies of interatomic distances in halides and chalcogenides. *Acta Crystallogr. Sect. A*. 1976. **32**, 751–767.

43. H. Frerichs, E. Pütz, F. Pfitzner, T. Reich, A. Gazanis, M. Panthöfer, J. Hartmann, O. Jegel, R. Heermann, W. Tremel, Nanocomposite antimicrobials prevent bacterial growth through the enzyme-like activity of Bi-doped cerium dioxide (Ce1−xBixO2−δ). *Nanoscale*. 2020. **12**, 21344–21358.

44. Z. A. Qiao, Z. Wu, S. Dai, Shape-Controlled Ceria-based Nanostructures for Catalysis Applications. *ChemSusChem*. 2013. **6**, 1821–1833.

45. A. K. P. Mann, Z. Wu, F. C. Calaza, S. H. Overbury, Adsorption and reaction of acetaldehyde on shape-controlled CeO2 nanocrystals: Elucidation of structure-function relationships. *ACS Catal.* 2014. **4**, 2437–2448.

46. Z. Hu, X. Liu, D. Meng, Y. Guo, Y. Guo, G. Lu, Effect of Ceria Crystal Plane on the Physicochemical and Catalytic Properties of Pd/Ceria for CO and Propane Oxidation. *ACS Catal.* 2016. **6**, 2265–2279.

47. C. J. Guild, D. Vovchok, D. A. Kriz, A. Bruix, B. Hammer, J. Llorca, W. Xu, A. El-Sawy, S. Biswas, J. A. Rodriguez, S. D. Senanayake, S. L. Suib, Water-Gas-Shift over Metal-Free Nanocrystalline Ceria: An Experimental and Theoretical Study. *ChemCatChem*. 2017.

48. V. Paunović, G. Zichittella, S. Mitchell, R. Hauert, J. Pérez-Ramírez, Selective Methane Oxybromination over Nanostructured Ceria Catalysts. *ACS Catal.* 2018. **8**, 291–303.

49. G. V. Lowry, R. J. Hill, S. Harper, A. F. Rawle, C. O. Hendren, F. Klaessig, U. Nobbmann,

P. Sayre, J. Rumble, Guidance to improve the scientific value of zeta-potential measurements in nano EHS. *Environ. Sci. Nano*. 2016. **3**, 953–965.

50. Z. W. She, J. Kibsgaard, C. F. Dickens, I. Chorkendorff, J. K. Nørskov, T. F. Jaramillo, Combining theory and experiment in electrocatalysis: Insights into materials design. *Science*. 2017. **355**, eaad4998.

51. D. R. Mullins, The surface chemistry of cerium oxide. *Surf. Sci. Rep.* 2015. **70**, 42–85.

52. Y. Wang, F. Wang, Q. Song, Q. Xin, S. Xu, J. Xu, Heterogeneous ceria catalyst with water-tolerant Lewis acidic sites for one-pot synthesis of 1,3-diols via prins condensation and hydrolysis reactions. *J. Am. Chem. Soc.* 2013. **135**, 1506–1515.

53. Z. Tan, G. Li, H. L. Chou, Y. Li, X. Yi, A. H. Mahadi, A. Zheng, S. C. Edman Tsang, Y. K. Peng, Differentiating Surface Ce Species among CeO2 Facets by Solid-State NMR for Catalytic Correlation. *ACS Catal.* 2020. **10**, 4003–4011.

54. W. P. Rothwell, W. X. Shen, J. H. Lunsford, Solid-state phosphorus-31 NMR of a chemisorbed phosphonium ion in HY zeolite: observation of proton-phosphorus-31 coupling in the solid-state. *J. Am. Chem. Soc.* 2002. **106**, 2452–2453.

55. Z. Ji, X. Wang, H. Zhang, S. Lin, H. Meng, B. Sun, S. George, T. Xia, A. E. Nel, J. I. Zink, Designed synthesis of CeO 2 nanorods and nanowires for studying toxicological effects of high aspect ratio nanomaterials. *ACS Nano*. 2012. **6**, 5366–5380.

56. C. Tyrsted, K. M. Ornsbjerg Jensen, E. D. Bøjesen, N. Lock, M. Christensen, S. J. L. Billinge, B. Brummerstedt Iversen, Understanding the Formation and Evolution of Ceria Nanoparticles Under Hydrothermal Conditions. *Angew. Chemie Int. Ed.* 2012. **51**, 9030–9033.

57. T. J. Fisher, M. Wang, Y. Ibrahim, B. Steffensmeier, C. L. Cheung, Effect of sodium nitrate on microwave-assisted synthesis of ceria nanocubes. *Mater. Lett.* 2016. **178**, 71–74.

58. P. Periyat, F. Laffir, S. A. M. Tofail, E. Magner, A facile aqueous sol–gel method for high surface area nanocrystalline CeO2. *RSC Adv.* 2011. **1**, 1794–1798.

59. Z. Wu, M. Li, J. Howe, H. M. Meyer, S. H. Overbury, Probing defect sites on CeO2 nanocrystals with well-defined surface planes by raman spectroscopy and O2 adsorption. *Langmuir*. 2010. **26**, 16595–16606.

60. I. Florea, C. Feral-Martin, J. Majimel, D. Ihiawakrim, C. Hirlimann, O. Ersen, Three-dimensional tomographic analyses of CeO2 nanoparticles. *Cryst. Growth Des.* 2013. **13**, 1110–1121.

61. C. Yang, X. Yu, S. Heißler, A. Nefedov, S. Colussi, J. Llorca, A. Trovarelli, Y. Wang, C. Wöll, Surface Faceting and Reconstruction of Ceria Nanoparticles. *Angew. Chemie Int. Ed.* 2017. **56**, 375–379.

62. Y. Chu, Z. Yu, A. Zheng, H. Fang, H. Zhang, S. J. Huang, S. Bin Liu, F. Deng, Acidic Strengths of Brønsted and Lewis Acid Sites in Solid Acids Scaled by 31P NMR Chemical Shifts of Adsorbed Trimethylphosphine. *J. Phys. Chem. C*. 2011. **115**, 7660–7667.

63. B. Liu, Z. Huang, J. Liu, Boosting the oxidase mimicking activity of nanoceria by fluoride capping: rivaling protein enzymes and ultrasensitive F− detection. *Nanoscale*. 2016. **8**, 13562–13567.

64. H. Li, M. Vrinat, G. Berhault, D. Li, H. Nie, P. Afanasiev, Hydrothermal synthesis and acidity characterization of TiO2 polymorphs. *Mater. Res. Bull.* 2013. **48**, 3374–3382.

65. F. H. Scholes, A. E. Hughes, S. G. Hardin, P. Lynch, P. R. Miller, Influence of Hydrogen

Peroxide in the Preparation of Nanocrystalline Ceria. *Chem. Mater.* 2007. **19**, 2321–2328.

66. P. Ji, L. Wang, F. Chen, J. Zhang, P Ji, L. Wang, F. Chen, J. Zhang, Ce3+-Centric Organic Pollutant Elimination by CeO2 in the Presence of H2O2. *ChemCatChem*. 2010. **2**, 1552–1554.

67. Y. J. Wang, H. Dong, G. M. Lyu, H. Y. Zhang, J. Ke, L. Q. Kang, J. L. Teng, L. D. Sun, R. Si, J. Zhang, Y. J. Liu, Y. W. Zhang, Y. H. Huang, C. H. Yan, Engineering the defect state and reducibility of ceria based nanoparticles for improved anti-oxidation performance. *Nanoscale*. 2015. **7**, 13981–13990.

68. H. Zhao, Y. Dong, P. Jiang, G. Wang, J. Zhang, Highly dispersed CeO2 on TiO2 nanotube: A synergistic nanocomposite with superior peroxidase-like activity. *ACS Appl. Mater. Interfaces*. 2015. **7**, 6451–6461.

69. V. V. Pushkarev, V. I. Kovalchuk, J. L. D'Itri, Probing defect sites on the CeO2 surface with dioxygen. *J. Phys. Chem. B.* 2004. **108**, 5341–5348.

70. S. V. N. T. Kuchibhatla, A. S. Karakoti, D. R. Baer, S. Samudrala, M. H. Engelhard, J. E. Amonette, S. Thevuthasan, S. Seal, Influence of Aging and Environment on Nanoparticle Chemistry: Implication to Confinement Effects in Nanoceria. *J. Phys. Chem. C*. 2012. **116**, 14108–14114.

71. Z. Zhang, Y. Wang, M. Wang, J. Lü, L. Li, Z. Zhang, M. Li, J. Jiang, F. Wang, An investigation of the effects of CeO2 crystal planes on the aerobic oxidative synthesis of imines from alcohols and amines. *Chinese J. Catal.* 2015. **36**, 1623–1630.

72. E. Sartoretti, C. Novara, F. Giorgis, M. Piumetti, S. Bensaid, N. Russo, D. Fino, In situ Raman analyses of the soot oxidation reaction over nanostructured ceria-based catalysts. *Sci. Reports*. 2019. **9**, 1–14.

73. S. Patil, S. Seal, Y. Guo, A. Schulte, J. Norwood, Role of trivalent La and Nd dopants in lattice distortion and oxygen vacancy generation in cerium oxide nanoparticles. *Appl. Phys. Lett.* 2006. **88**, 243110.

74. M. Kluenker, M. Nawaz Tahir, R. Ragg, K. Korschelt, P. Simon, T. E. Gorelik, B. Barton, S. I. Shylin, M. Panthöfer, J. Herzberger, H. Frey, V. Ksenofontov, A. Möller, U. Kolb, J. Grin, W. Tremel, Pd@Fe2O3 Superparticles with Enhanced Peroxidase Activity by Solution Phase Epitaxial Growth. *Chem. Mater.* 2017. **29**, 1134–1146.

75. Y. Huang, J. Ren, X. Qu, Nanozymes: Classification, Catalytic Mechanisms, Activity Regulation, and Applications. *Chem. Rev.* 2019. **119**, 4357–4412.

76. D. Wischang, O. Brücher, J. Hartung, Bromoperoxidases and functional enzyme mimics as catalysts for oxidative bromination-A sustainable synthetic approach. *Coord. Chem. Rev.* 2011. **255**, 2204–2217.

77. J. Kaspar, P. Fornasiero, G. Balducci, R. Di Monte, N. Hickey, V. Sergo, Effect of ZrO2 content on textural and structural properties of CeO2–ZrO2 solid solutions made by citrate complexation route. *Inorganica Chim. Acta*. 2003. **349**, 217–226.

3.7. Supporting Information

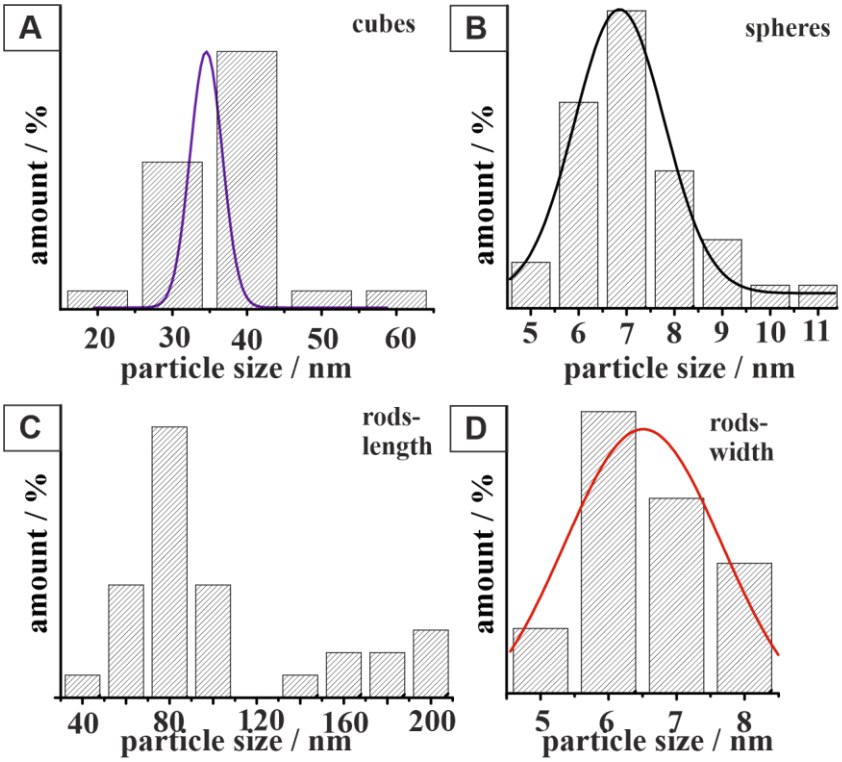

Figure S3.1 Histograms showing the particle size distribution of CeO_{2-x} (A) nanocubes, (B) nanospheres and (C,D) nanorods.

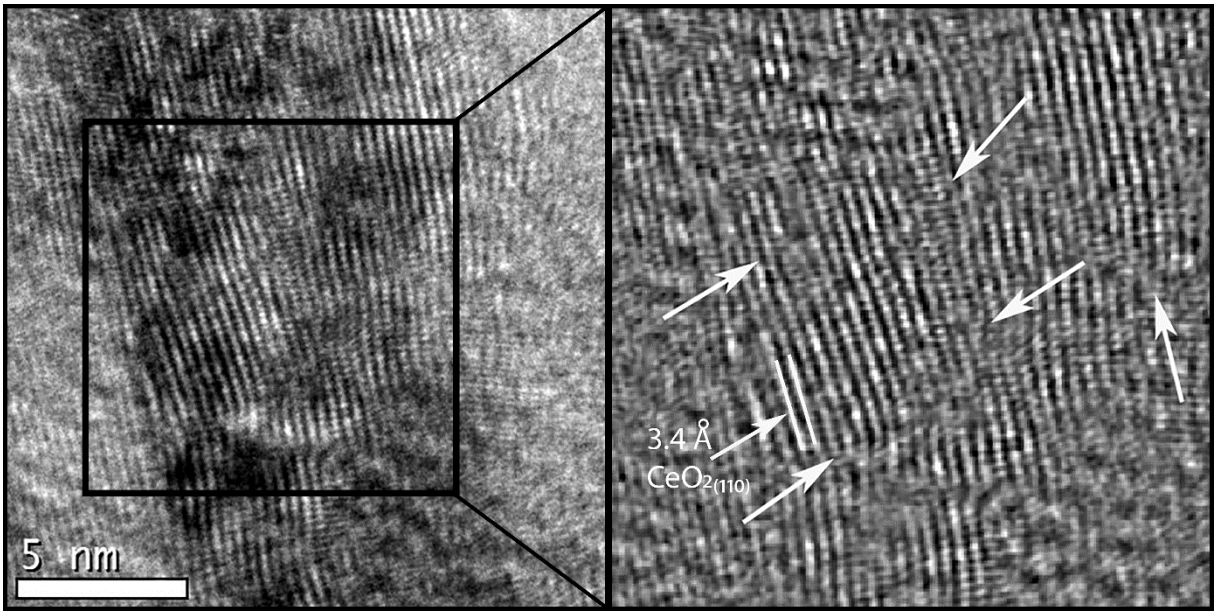

Figure S3.2. HRTEM images of CeO_{2-x} nanorods with a zoom of showing line defects.

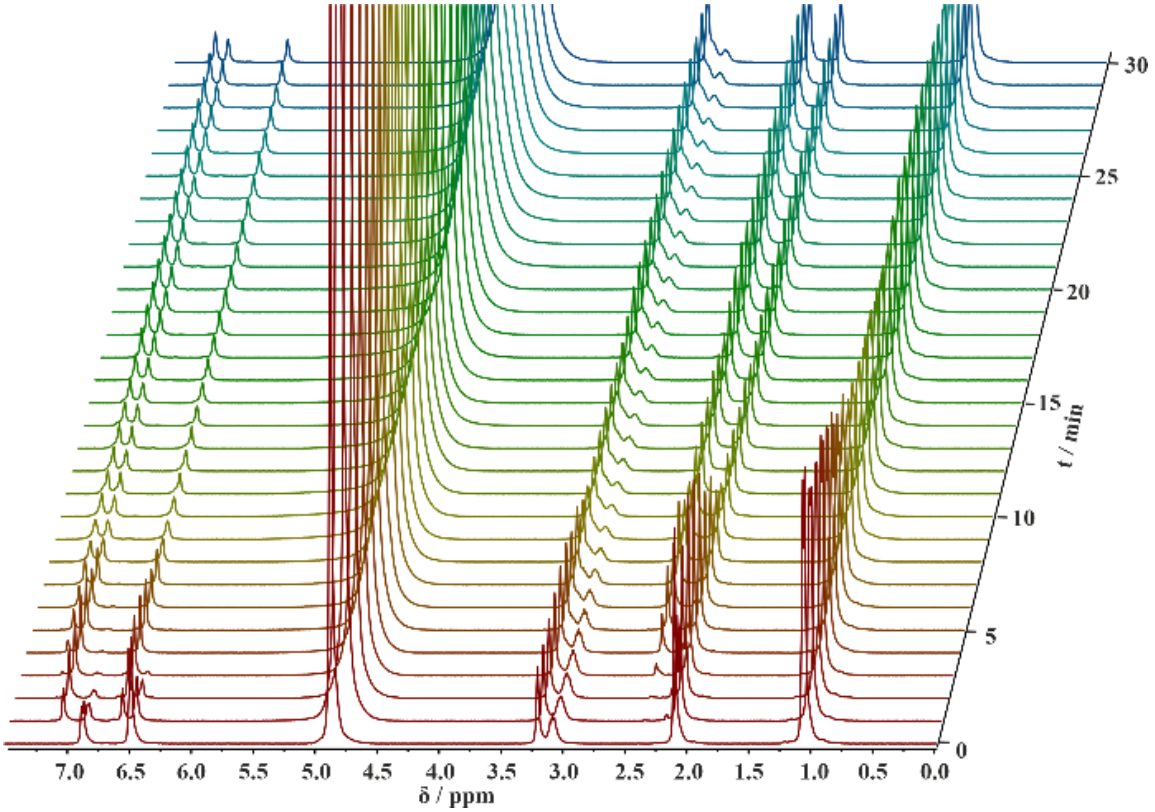

Figure S3.3 Time-resolved (stacked) ^{1}H NMR spectra for the bromination of thymol catalyzed by CeO_{2-x} nanorods.

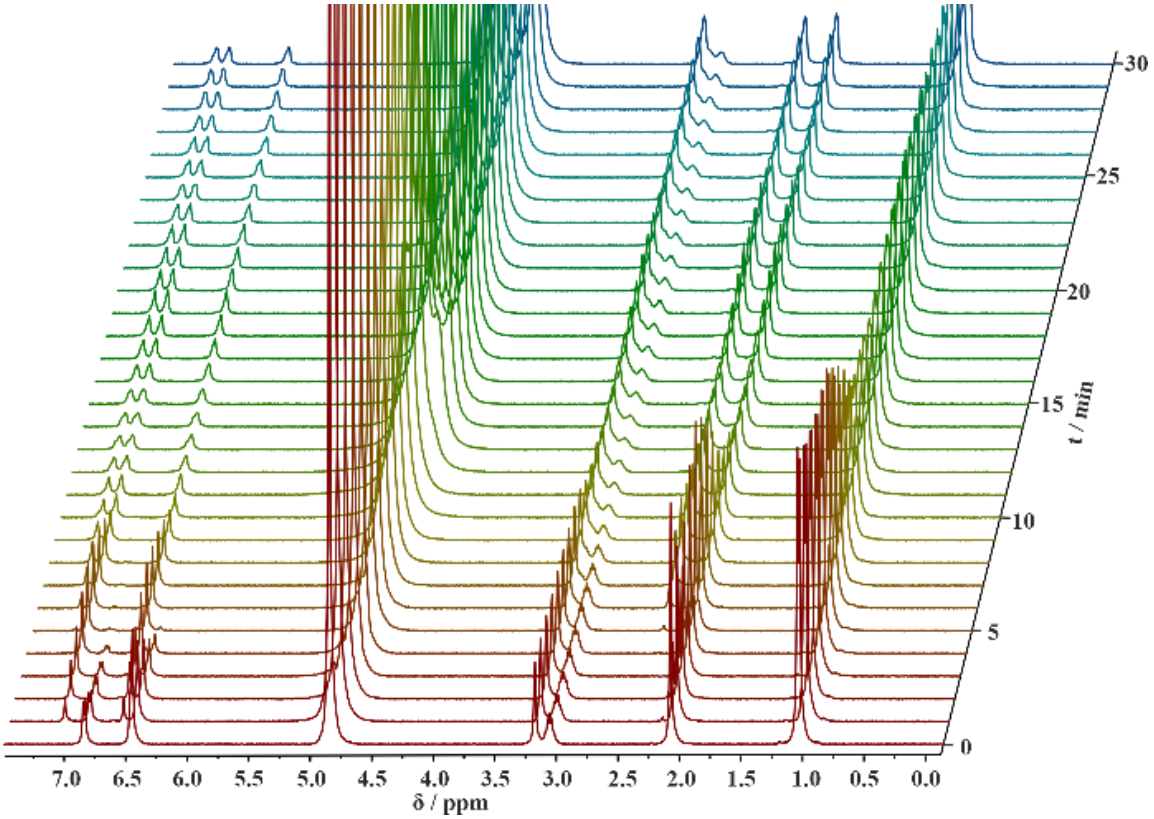

Figure S3.4. Time-resolved (stacked) ^{1}H NMR spectra for the bromination of thymol catalyzed by CeO_{2-x} nanospheres.

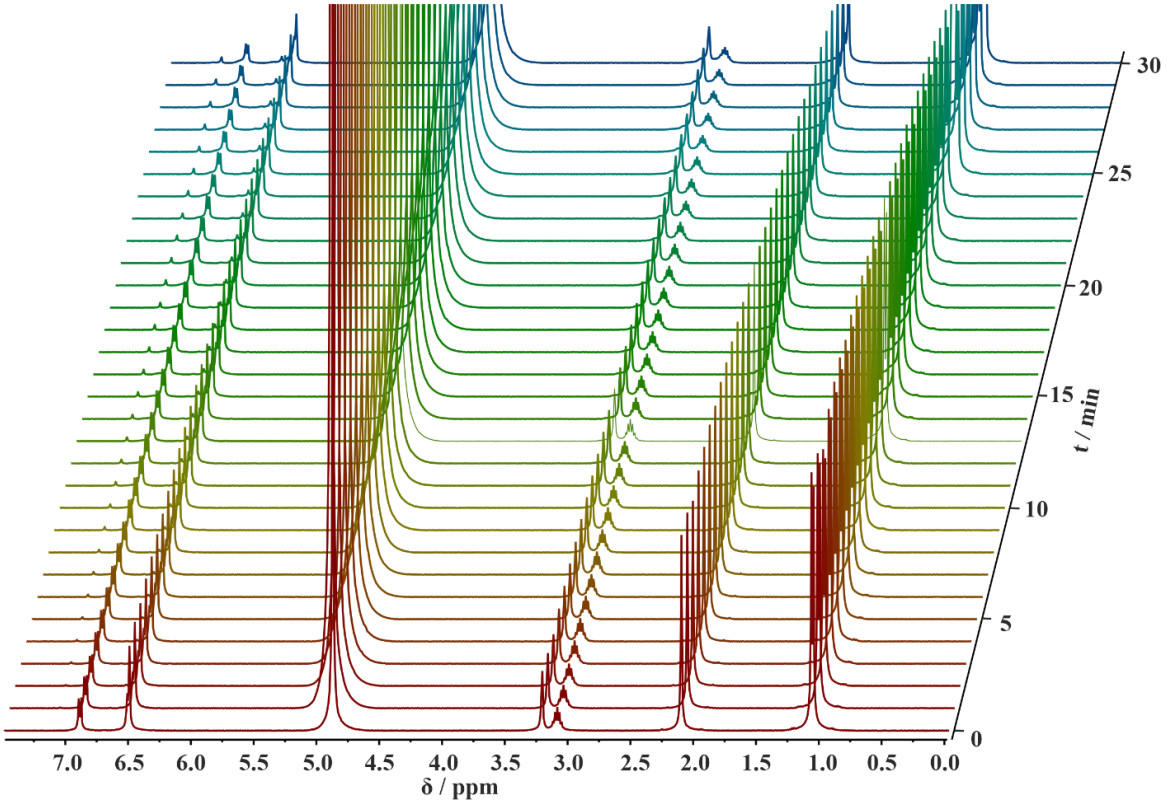

Figure S3.5. Time-resolved (stacked) ^{1}H NMR spectra for the bromination of thymol catalyzed by CeO_{2-x} nanocubes.

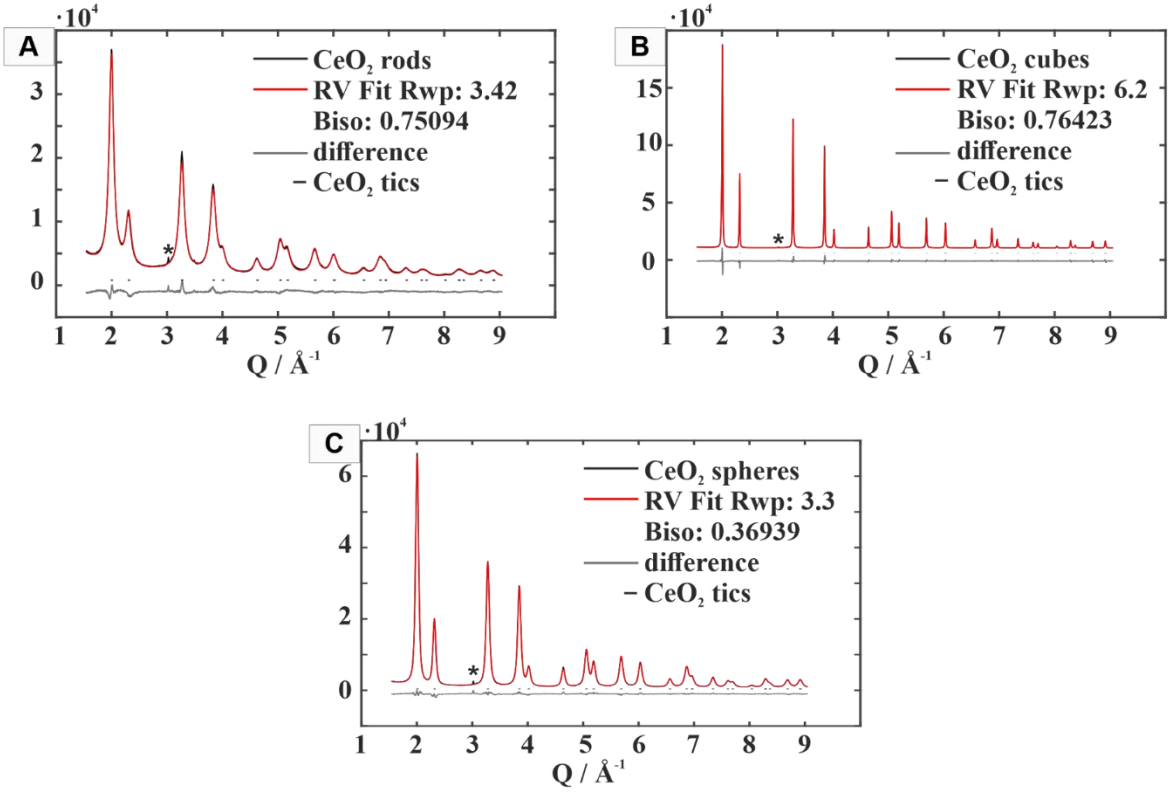

Figure S3.6. Powder diffraction phase analysis with Rietveld refinements of CeO_{2-x} nanorods (A), nanocubes (B) and nanospheres (C). Experimental powder pattern (black dots), Rietveld analysis (red lines), difference plots (blue lines). Tick marks show reflection positions of for pure ceria (fluorite structure, $Fm\bar{3}m$). The additional reflex "*"is due to the sample preparation on acetate foil.

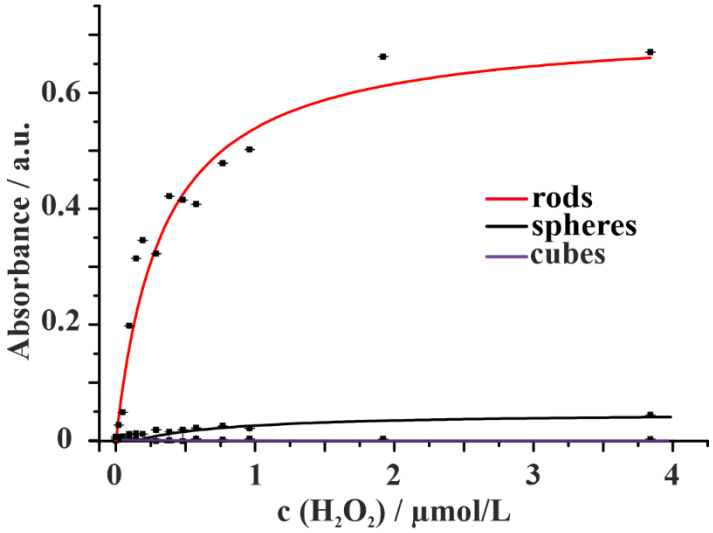

Figure S3.7. Michaelis Menten Fit for CeO_{2-x} rods (red), spheres (black) and cubes.

The catalytic activity of CeO_{2-x} nanocrystals is described by their turnover frequencies (TOF) or the catalytic constants (k_{cat}).[1] The TOF depends on the (i) catalyst surface, (ii) time, and (iii) mass concentration. Brunauer-Emmett-Teller (BET) surface areas of 98.4 m^2g^{-1} (nanorods), 44.6 m^2g^{-1} (nanospheres) and 16.1 m^2g^{-1} (nanocubes) were determined to normalize the reaction rates because the bromination of thymol is surface specific (only the surface of the catalyst is accessible for the substrate). The rate of reaction (ROR) is defined by equation (S3.1). Here, the accessible surface area per mass equivalent of the catalyst is expressed through the BET surface area (S_{BET} in $m^2\ g^{-1}$), and equation (S3.1) was evaluated based on time (v_{max} / M min^{-1}), surface area (S_{BET} / $m^2\ g^{-1}$) and mass concentration (β(Cat) / g L^{-1}).

$$\mathrm{TOF} = \frac{v_{max}}{[\mathrm{Cat}]_0} \xrightarrow{[\mathrm{Cat}]_0 \rightarrow S_{BET}\cdot\beta(\mathrm{Cat})} \mathrm{ROR} = \frac{v_{max}}{S_{BET}\cdot\beta(\mathrm{Cat})} \qquad \text{(S3.1)}$$

Table S3.1. shows an overview of v_{max}, K_m, S_{BET} and ROR for all three morphologies.

Sample	**v_{max} / µM min^{-1}**	**K_m/ µM**	**S_{BET}/$m^2\ g^{-1}$**	**ROR/ µmol m^{-2} min^{-1}**
CeO_{2-x} nanorods	0.72±0.04	330±5	98.4	0.29
CeO_{2-x} nanospheres	0.049±0.007	750±24	44.6	0.04
CeO_{2-x} nanocubes	n.a.	n.a.	16.1	n.a.

Experimental procedure isolating products:

4-Bromothymol: 225 mg (1.5 mmol) Thymol and 140 mg (1.18 mmol) KBr were dissolved in 33 mL of a 10:1 % v/v MeOH/H_2O mixture. Subsequentially 300 µL conc. H_2O_2 and 300 µL conc. $HClO_4$ are added to obtain pH=1. 28 mg of CeO_{2-x} nanoparticles (rods) were added. The reaction was stirred for 3 h at room temperature. The reaction solution was diluted with water to 100 ml and extracted five times with 30 mL diethylether. The organic phase was dried over sodium sulfate (Na_2SO_4), filtered and the solvent was evaporated by a rotary evaporator. A yellow oil was received, which was crystallized at -20°C using 1 mL petrol ether yielding colourless crystals. ^{1}H NMR (400 MHz,$CDCl_3$): 4-bromo-2-isopropyl-5-methylphenol (4-Bromthymol): δ[ppm]= 7.29 (s, 1 H, H-3), 6.64 (s, 1 H, H-6), 3.13 (h, *J*=6.9 Hz, 1 H, Ar-C<u>H</u>-(CH_3)$_2$), 2.30 (s, 1 H, Ar-C<u>H</u>$_3$, 1.22 (d, *J* = 6.9 Hz, 6 H, Ar-CH-(C<u>H</u>$_3$)$_2$).

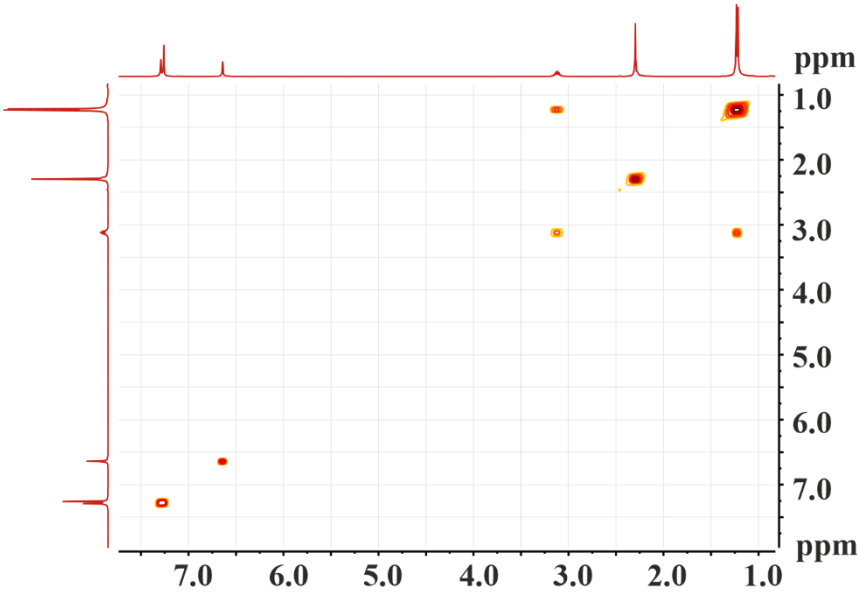

Figure S3.8. COSY of 4-Bromothymol.

2,4-Dibromothymol: 225 mg (1.5 mmol) Thymol and 360 mg (3 mmol) KBr were dissolved in 33 mL of a 10:1 % v/v MeOH/H_2O mixture. Subsequentially 300 µL conc. H_2O_2 and 300 µL conc. $HClO_4$ are added to obtain pH=1. 28 mg of CeO_{2-x} nanoparticles (rods) were added. The reaction was stirred for 3 h at room temperature. The reaction solution was diluted with water to 100 ml and extracted five times with 30 mL diethylether. The organic phase was dried over sodium sulfate (Na_2SO_4), filtered and the solvent was evaporated by a rotary evaporator. A yellow oil was received, which purified via column chromatography using a 3:1 mixture of cyclohexan/dichloromethane.

^{1}H NMR (400 MHz,$CDCl_3$): 2,4-dibromo-6-isopropyl-3-methylphenol (2,4-Dibromthymol): δ[ppm]= 7.31 (s, 1 H, H5), 5.68 (s, 1 H, Ar-O<u>H</u>), 3.26 (h, *J*=6.9 Hz, 1 H, Ar-C<u>H</u>-$(CH_3)_2$), 2.52 (s, 3 H, Ar-C<u>H</u>$_3$, 1.22 (d, *J* = 6.9 Hz, 6 H, Ar-CH-(C<u>H</u>$_3$)$_2$).

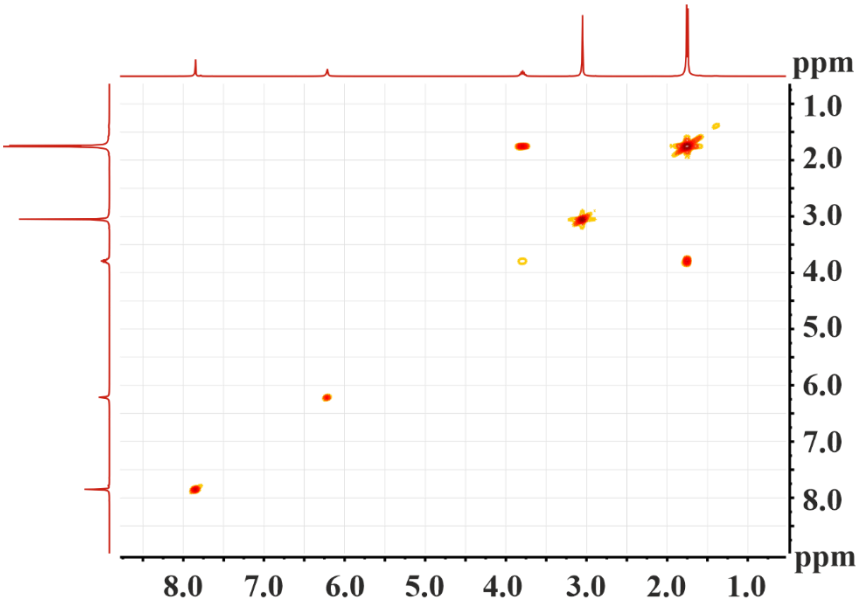

Figure S3.9. COSY of 2,4-Dibromothymol.

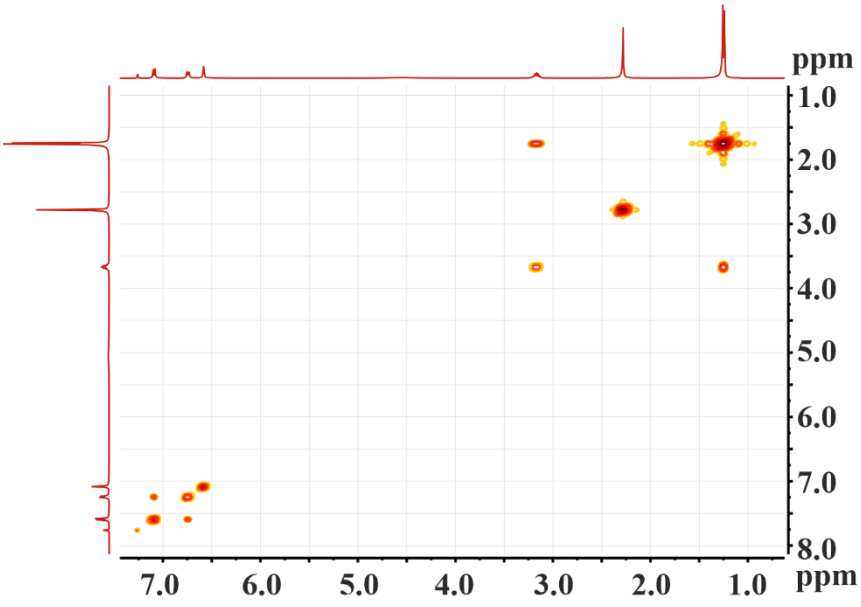

Figure S3.10. COSY of thymol.

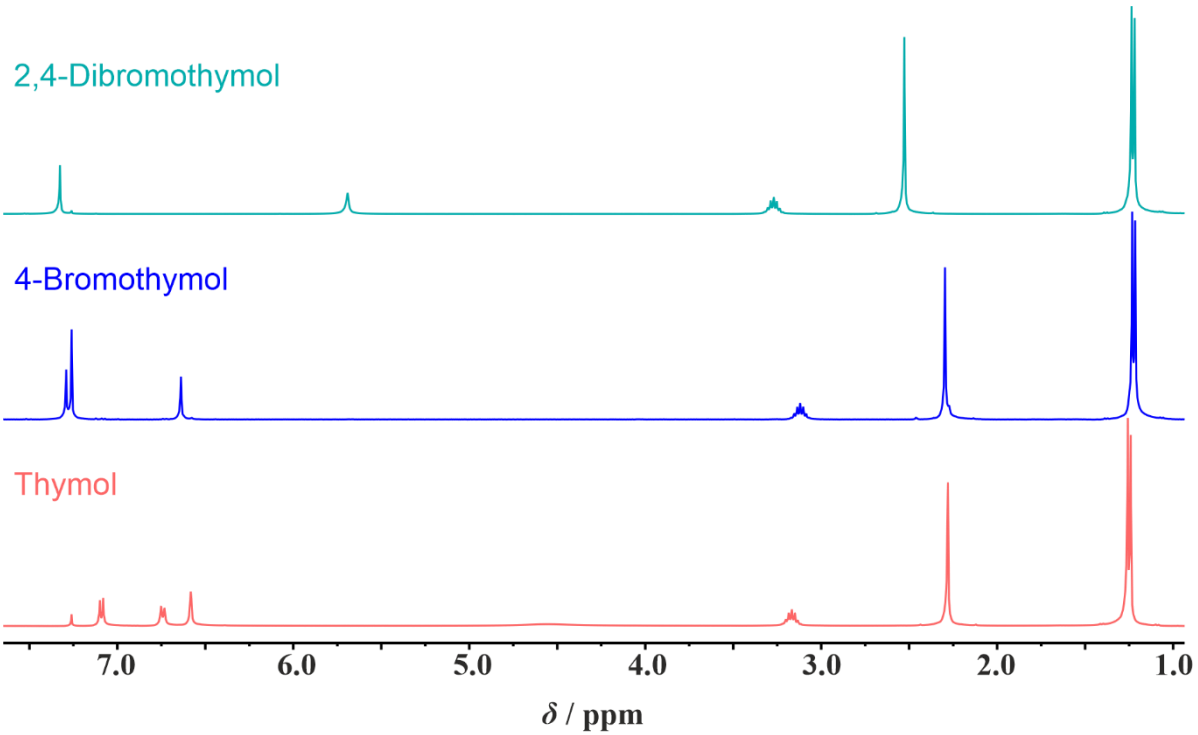

Figure S3.11. Stacked ^{1}H-NMR of Thymol, 4-Bromothymol and 2,4-Dibromothymol.

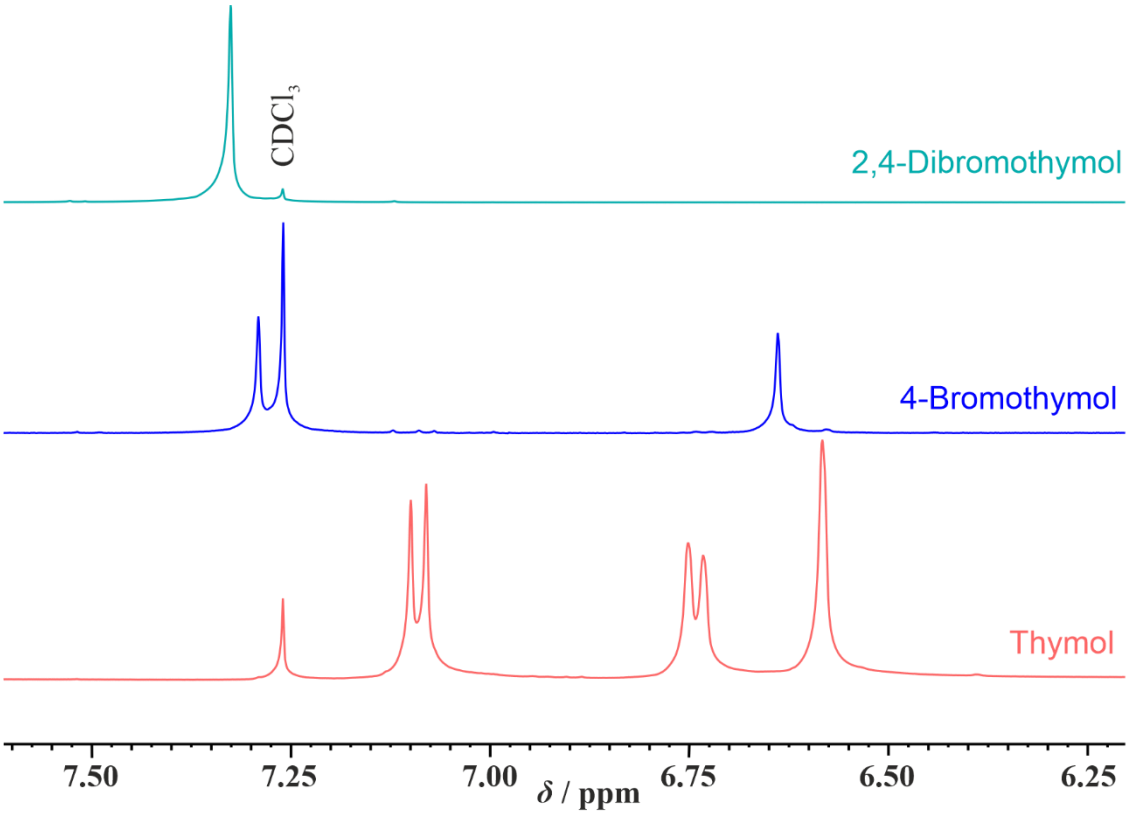

Figure S3.12. Stacked ^{1}H-NMR of Thymol, 4-Bromothymol and 2,4-Dibromothymol in range from 7.5-6.25 ppm.

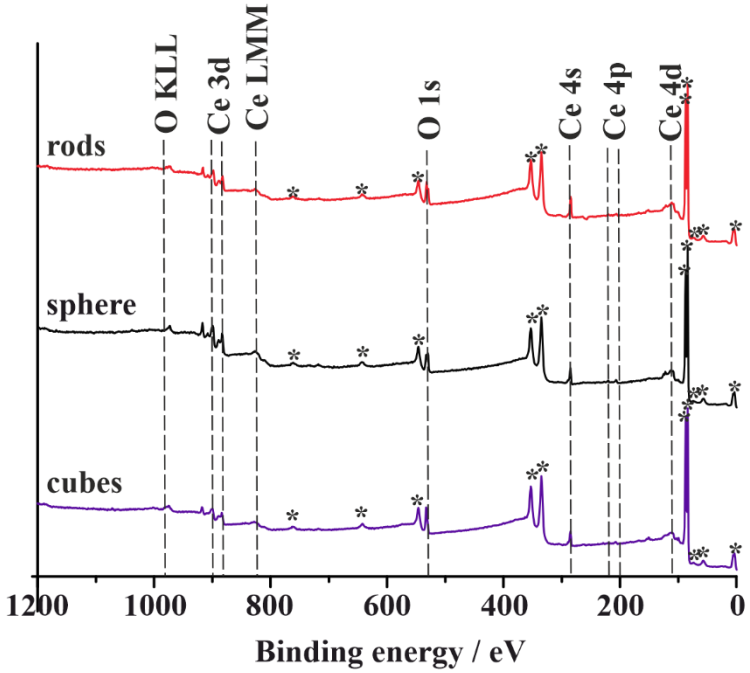

Figure S3.13. XPS survey spectrum of CeO_{2-x} nanorods, -spheres and –cubes using non-monochromatized Al Kα excitation. The detected XPS lines of Ce and O are named respectively, the additional signals marked with * belong to Au caused by prior sputtering of sample holders before preparation.

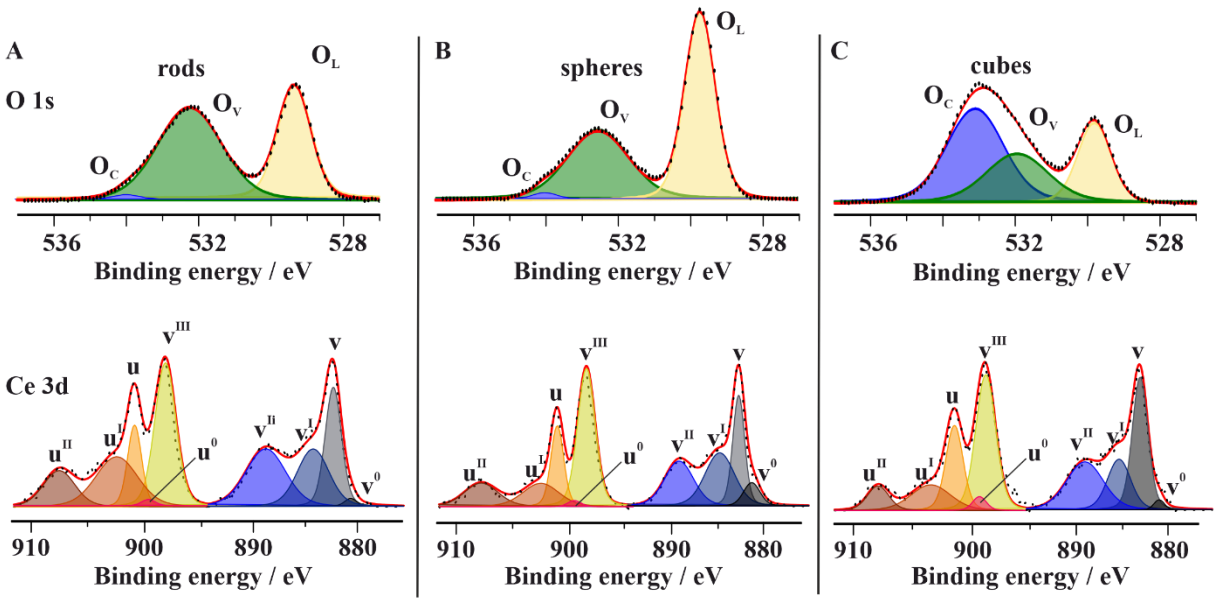

Figure S3.14. XPS spectra of CeO_{2-x} (A) nanorods, (B) -spheres and (C) -cubes. Shown are the Ce 3d, O 1s regions confirming the presence of the elements Ce and O.

Figure S3.13 show the Ce and O regions of the XPS spectra of CeO_{2-x} nanorods, -spheres and -cubes. The signals are labeled as v, v^{II}, v^{III} and u, u^{II}, where v and u correspond to $3d_{5/2}$

and $3d_{3/2}$ orbitals of Ce^{4+}, respectively. For Ce^{3+} v^0, v^1 and u^0, u^1 correspond to $3d_{5/2}$ and $3d_{3/2}$ orbitals. Revealing mixed oxidation states (4+/3+) for surface Ce in CeO_{2-x}. Deconvolution of the peaks with respect to the $3d_{5/2}$ and $3d_{3/2}$ transitions of Ce^{4+} and Ce^{3+} yielded proportions of approx. 30, 30, and 20% Ce^{3+} surface sites for CeO_{2-x} nanorods, -spheres and -cubes. This shows also that oxygen defects associated with Ce^{3+} predominantly occur at the particle surface (as expected from the ionic radii of Ce^{4+} and Ce^{3+}. However Ce^{3+}/Ce^{4+} ratio in nanocubes and –spehres does not differ much from each other. The 1s oxygen signals in Figure S3.14 are assigned to oxide in the crystalline network (O_L), oxygen-deficient regions (O_v) and chemisorbed oxygen species (O_c), respectively.[2,3] Oxygen deficient concentration is highest for CeO_{2-x} nanorods which is in harmony with raman results and the XPS spectrum of Ce 3d region (highest Ce^{3+} concentration). Cubes exhibit a higher ratio of adsorbed hydroxylgroups (blue) on its surface, wheras rods and spheres only show traces. XPS measurements reveal oxygen-deficient regions (green) on the surface for all samples as well as lattice oxygen (yellow). For cubes, chemisorbed oxygen compounds like lossly bound hydroxyl groups or water exhibit the highest concentration. The increasing content of hydroxyl surface groups may hinder the activity towards oxidative bromination. Attachement of negatively charged Br^- as well as hydrogenperoxide species could be made more difficult.

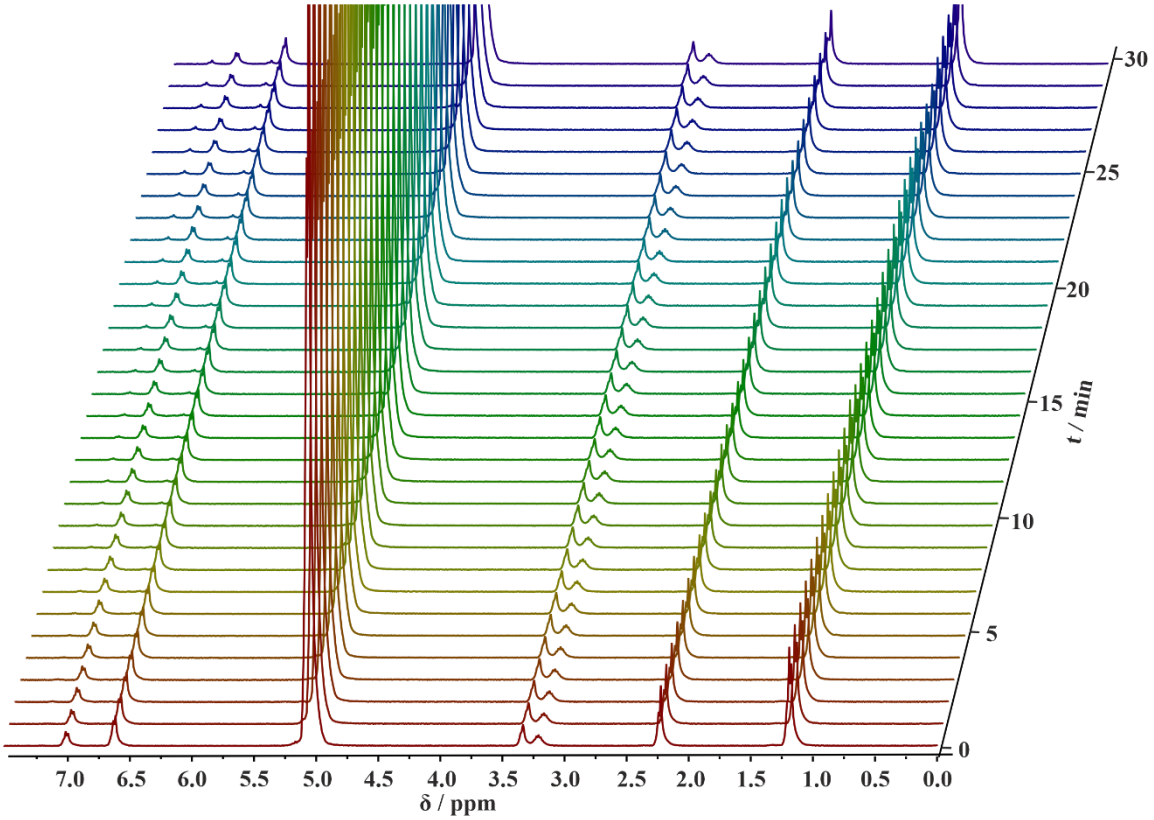

Figure S 3.15. Time-resolved (stacked) ^{1}H NMR spectra for the bromination of thymol without addition of CeO_{2-x} nanoparticles.

3.7.1. References

1. S. Kozuch, J. M. L. Martin, “Turning Over” Definitions in Catalytic Cycles. *ACS Catal.* 2012. **2**, 2787–2794.

2. D. H. Yoon, Y. J. Tak, S. P. Park, J. Jung, H. Lee, H. J. Kim, Simultaneous engineering of the interface and bulk layer of Al/ sol -NiO x /Si structured resistive random access memory devices. *J. Mater. Chem. C.* 2014. **2**, 6148–6154.

3. C. Wang, X. Cui, J. Liu, X. Zhou, X. Cheng, P. Sun, X. Hu, X. Li, J. Zheng, G. Lu, Design of Superior Ethanol Gas Sensor Based on Al-Doped NiO Nanorod-Flowers. *ACS Sensors*. 2016. **1**, 131–136.

4 Defect-Controlled Halogenating Properties of Lanthanide-Doped Ceria Nanozymes

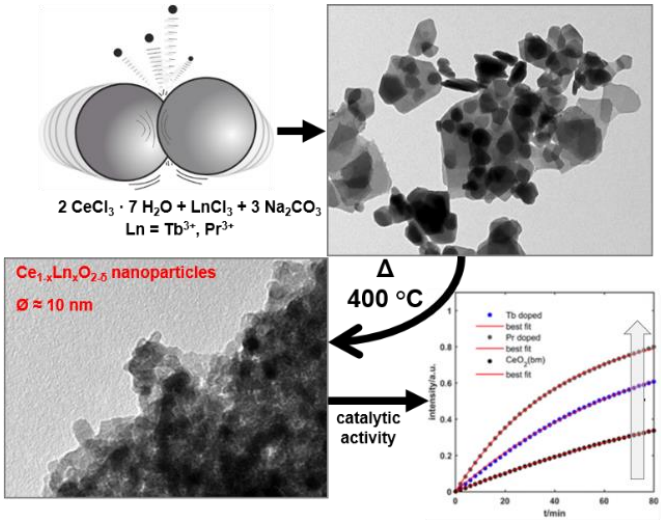

This chapter 4 is submitted in Nanoscale, 2021.

Author Contributions:

Olga Jegel: Concept development, nanoparticle synthesis, TEM and SEM measurement, ζ–potential and BET surface are measurement, haloperoxidase assay, manuscript preparation, figure preparation.

XXX: Concept development, nanoparticle synthesis, PXRD refinements and FTIR measurement, manuscript preparation, figure preparation.

XXX: Nanoparticle synthesis, haloperoxidase assay.

XXX: Raman measurement.

XXX: ESR measurement.

XXX: Biologic evaluation.

XXX: XPS measurement.

XXX: Manuscript correction.

XXX: Manuscript correction.

XXX: Manuscript correction and scientific supervision.

4.1. Summary

After investigating in the first chapter whether the morphology of the nanoparticles has an influence on the catalytic activity, the aim of this chapter was to examine whether an increase in activity can be achieved by doping CeO_2 nanoparticles with other lanthanides. Indeed, doping with a foreign atom can easily change the properties of a compound.

In this process, a mechanochemical synthesis was adopted for the production of the nanoparticles. This offers the advantage of producing larger quantities and reducing use of solvents, which make it a "green chemistry" technique.

For the synthesis of CeO_2 in a planetary ball mill, the reactants $CeCl_3 \cdot 7H_2O$ and Na_2CO_3 were milled; for doping, the salts $TbCl_3 \cdot 6\ H_2O$ and $PrCl_3 \cdot H_2O$ were also added with a doping level of 10%. It was elucidated that milling forms the intermediates $Na_4Ce_2(CO_3)_5$ and NaCl, which results in the desired product CeO_2 after thermal treatment at 400°C. We assume that NaCl has an important role in the synthesis as a template or matrix by inhibiting particle growth.

The nanoparticles were tested for their haloperoxidase-like activity. This revealed that doping with terbium doubled the catalytic activity, and doping with praseodymium even almost increased it fourfold.

Subsequently, the factors responsible for the change in catalytic activity were investigated after doping the nanoparticles. For this purpose, the defect density of the undoped and doped compounds were analyzed in more detail. Therefore, Raman and ESR measurements were performed. Raman spectra showed that doping resulted in more surface defects than for undoped nanoparticles. This hypothesis was also confirmed by the ESR data. They show an increase of these surface-located O-defects upon doping with Pr^{3+} and Tb^{3+} using ball-mill synthesis, which means that these dopants stabilize the catalytically important O_2^- radicals.

To investigate the behavior of the doped and undoped nanoparticles in aqueous solution in more detail and to interpret a correlation between the different ζ-potentials, FTIR spectra of wet and dry nanoparticles were recorded. A difference between the carbonate vibration modes of the doped and undoped CeO_2 nanoparticles was obtained. We assume that CO_2 is chemisorbed less due to Ln-doping, resulting in a more positive ζ-potential for doped nanocrystals.

4.2. Introduction

Cerium dioxide has a wide range of applications in catalysis.[1] The high mobility of oxygen ions coupled with its mixed valence properties (Ce^{4+}/Ce^{3+}) makes the material suitable for use as a redox-active support in three-way catalytic converters,[2] water-gas shift reaction,[3] steam reforming,[1] water splitting,[4] and fuel cells.[5] In addition, biomedical applications of nanoceria[6,7] are being explored for use in coatings,[8] UV shielding,[9] and humidity sensors.[10]

Biofouling is a pervasive problem, especially in environments where microorganisms are present.[11] A number of marine organisms have developed a sustainable defense strategy based on the interruption of bacterial communication ("quorum sensing") through chemical modification of signaling molecules, so-called "autoinducers (AIs)" by halogenation.[12–15] This makes biohalogenation an effective method for inhibiting biofilm formation. Naturally enzymes such as haloperoxidases (HPOs) aid in the halogenation of signaling molecules by catalyzing the formation of hypohalites as bioactive intermediates (HOX: hypohalous acid or hypohalites) through the reaction of halide ions (Cl^-, Br^-, I^-) with hydrogen peroxide formed in sunlight.[13,16,17] V_2O_5 and CeO_2 nanoparticles can emulate the catalytic activity of haloperoxidases, i.e., they act as functional mimics of these halogenating enzymes (nanozymes).[8,18–23]

The defect chemistry of ceria is crucial for its catalytic performance. It can be engineered by metal substitution (i.e., with metal "dopants") associated with oxygen vacancies.[24,25] Metal substitution showed a drastic enhancement in the activity of the nanoceria enzyme mimic.[26,27] However, metal substitution alters not only the defect concentration but also the surface potential, which may enhance (but also prevent) the adsorption of charged reactant species.[26]

Due to the growing interest in ceria nanoparticles, there is a need for versatile synthesis routes with high yields, access to a wide range of dopants, and small and homogeneous particle sizes. Mechanochemical synthesis is promising for this purpose. Ball-milling is of particular interest for large-scale applications due to its scalability and reduced use of solvents, which make it a "green chemistry" technique.[28] In addition, mechanochemistry can lead to out-of-equilibrium structures by introducing strain and defects.[28]

Here we show that a mechanochemical preparation for CeO_2[29] can be used for preparing homogeneous solid solutions (i.e., for doping) with lanthanides $Ce_{1-x}Ln_xO_{2-x/2}$, in particular Pr^{3+} and Tb^{3+}, over the full substitution range with a significantly smaller particle size. The

haloperoxidase activity of the particles was compared to a CeO_2 reference material prepared hydrothermally under equilibrium conditions.

4.3. Results and Discussion

Synthesis of Nanoceria. Ceria nanocrystals were synthesized mechanochemically in a planetary ball mill. For this purpose, cerium trichloride (prepared from hydrated cerium carbonate $Ce_2(CO_3)_3 \cdot 8H_2O$) and sodium carbonate were ball-milled in cyclohexane as dispersion medium, followed by annealing at 400 °C for 5 hours. The resulting product mixture was washed several times with water until the pH was neutral and dried *in vacuo*. Figure 4.1a shows the X-ray powder diffractogram and the corresponding transmission electron microscopy (TEM) image of nanoceria after mechanochemical treatment of the reactants $CeCl_3$ and Na_2CO_3.

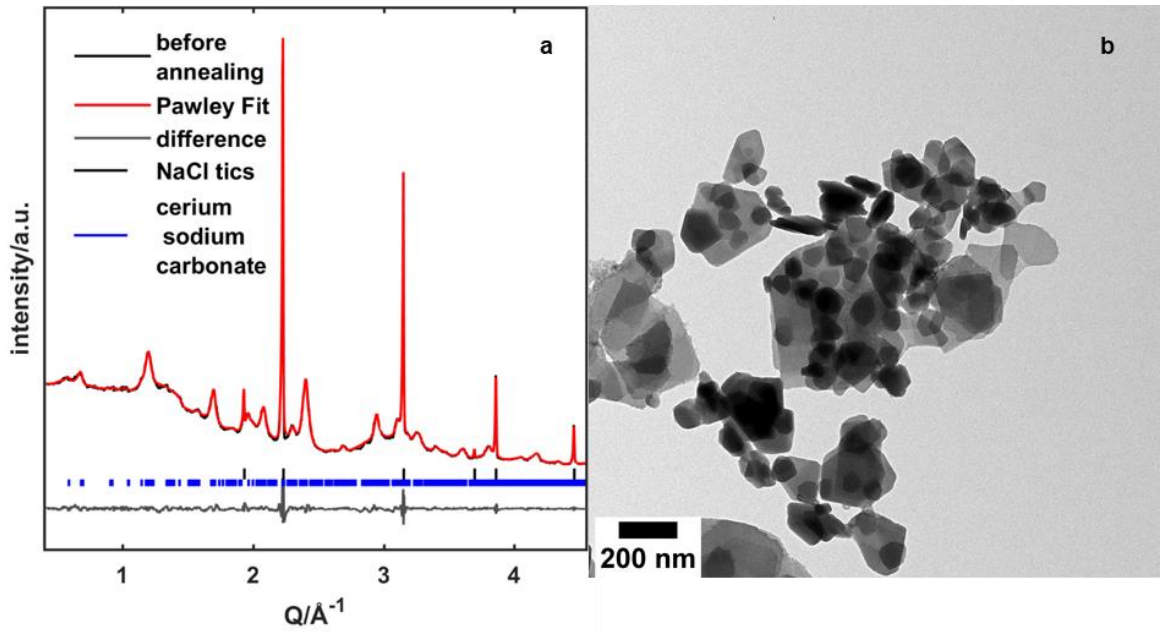

Figure 4.1. (a) Pawley fit of the X-ray powder diffractogram after mechanical treatment of the reactants $CeCl_3$ and Na_2CO_3 before annealing. (b) TEM image of $Na_4Ce_2(CO_3)_5$ before annealing.

The expected intermediates according to a simplified mechanochemical reaction

$$2\ CeCl_3 \cdot 7\ H_2O + 3\ Na_2CO_3 \rightarrow Ce_2(CO_3)_3 + 6\ NaCl + 14\ H_2O \quad (4.1)$$

are $Ce_2(CO_3)_2$ and NaCl. However, because shear forces during milling are high and the reaction is locally constrained to a mechanical event, sodium cerium carbonate, $Na_4Ce_2(CO_3)_5$, is formed in an initial step according to

$$2\ CeCl_3 \cdot 7\ H_2O + 5\ Na_2CO_3 \rightarrow Na_4Ce_2(CO_3)_5 + 6\ NaCl + 14\ H_2O \quad (4.2)$$

The reflections of $Na_4Ce_2(CO_3)_5$ are broad indicating low crystallinity. Despite the high scattering cross section of cerium (compared to sodium), the intensity of the reflections is low, further supporting the assumption of a small domain size or possible disorder. Since product formation occurs during local mechanical events that cause high local diffusion

(compression, shear etc.), structures with strain and local disorder are expected. The transmission electron microscopy (TEM) image of a sample before annealing (Figure 4.1b) shows that the product contains no monodisperse particles at this stage.

Figure 4.2a and b shows the powder diffractograms of the annealed mixture before and after washing with water. The product contains CeO_2 and NaCl before and single-phase CeO_2 after washing. The broad reflections associated with ceria indicate the presence of nanocrystals. Therefore, CeO_2 nanocrystals are formed during annealing. $Na_4Ce_2(CO_3)_5$ thermally decomposes to CeO_2, CO_2 and Na_2O. No ceria nanocrystals were obtained by washing the ball-milled mixture with water (to remove the sodium-containing products before annealing). *Thus, NaCl is essential for the formation of nanocrystals*. We assume that NaCl acts as a template or matrix by inhibiting particle growth. Figure 4.2c shows a TEM image of the ceria nanoparticles synthesized by ball milling after annealing and washing with water. Depending on the annealing temperature, particles with sizes ranging from about 5 to several hundred nm could be prepared.

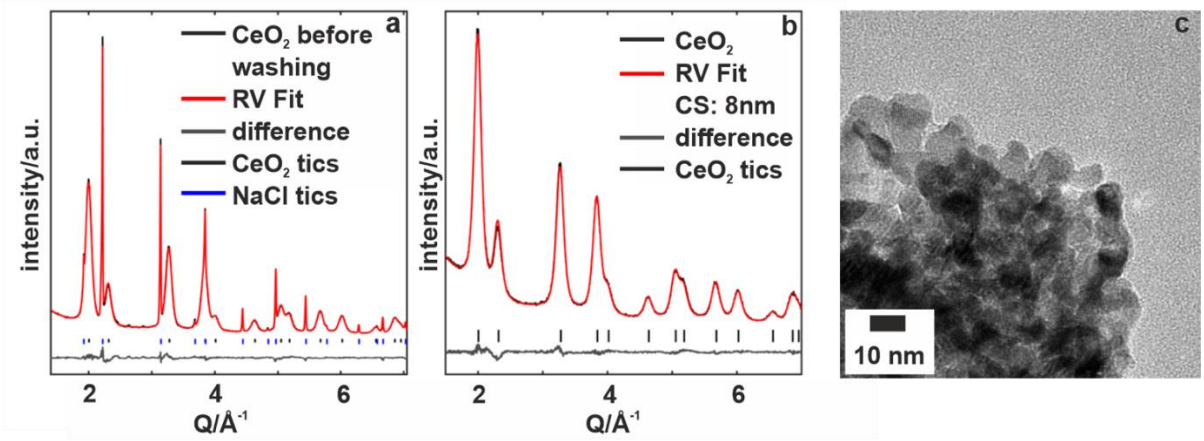

Figure 4.2. (a) X-ray diffractogram of ceria nanocrystals after annealing and before washing with water. (b) X-ray diffractogram of ceria nanocrystals after washing with water (experimental data (red dots), Rietveld refinement (black line) and corresponding difference plot (red line)). Reflections were indexed to a face-centered cubic cell with a = 5.41877(6), R_{wp} = 3.6 %, and GoF = 1.3 for (a) and a = 5.4099(5) Å, R_{wp} = 4.3 % and GoF = 2.3 for (b). Blue tics indicate reflection positions of NaCl. (c) TEM image of CeO_2 synthesized by ball milling after annealing and washing with water.

Ln-Doping of Ceria Nanocrystals. Mechanochemical synthesis provides access to lanthanide-doped "activated" ceria with non-equilibrium structure[30] using lanthanoid (III) chlorides as starting compounds. We tested various lanthanides like europium (Eu), Dysprosium (Dy), Gadolinium (Gd) and Samarium (Sm). With some the activity could be increased, with some not. For more detailed studies, undoped CeO_2, a doped compound with moderate catalytic activity (terbium (Tb) substitution) and one with the highest activity

(praseodymium (Pr) substitution) were focused on. Hydrothermally prepared nanocrystals were used as "equilibrium-state" reference (Figure S4.1). Figure 4.3a and b show the powder X-ray diffraction (P-XRD) patterns of ceria nanocrystals doped with 10 % Pr^{3+} and Tb^{3+}. The doping level of 10% was chosen, as the particles showed the highest activity here. The compounds were doped up to 30%. For some compounds, a secondary phase was already formed at 40% doping, so a higher doping level was not prepared.

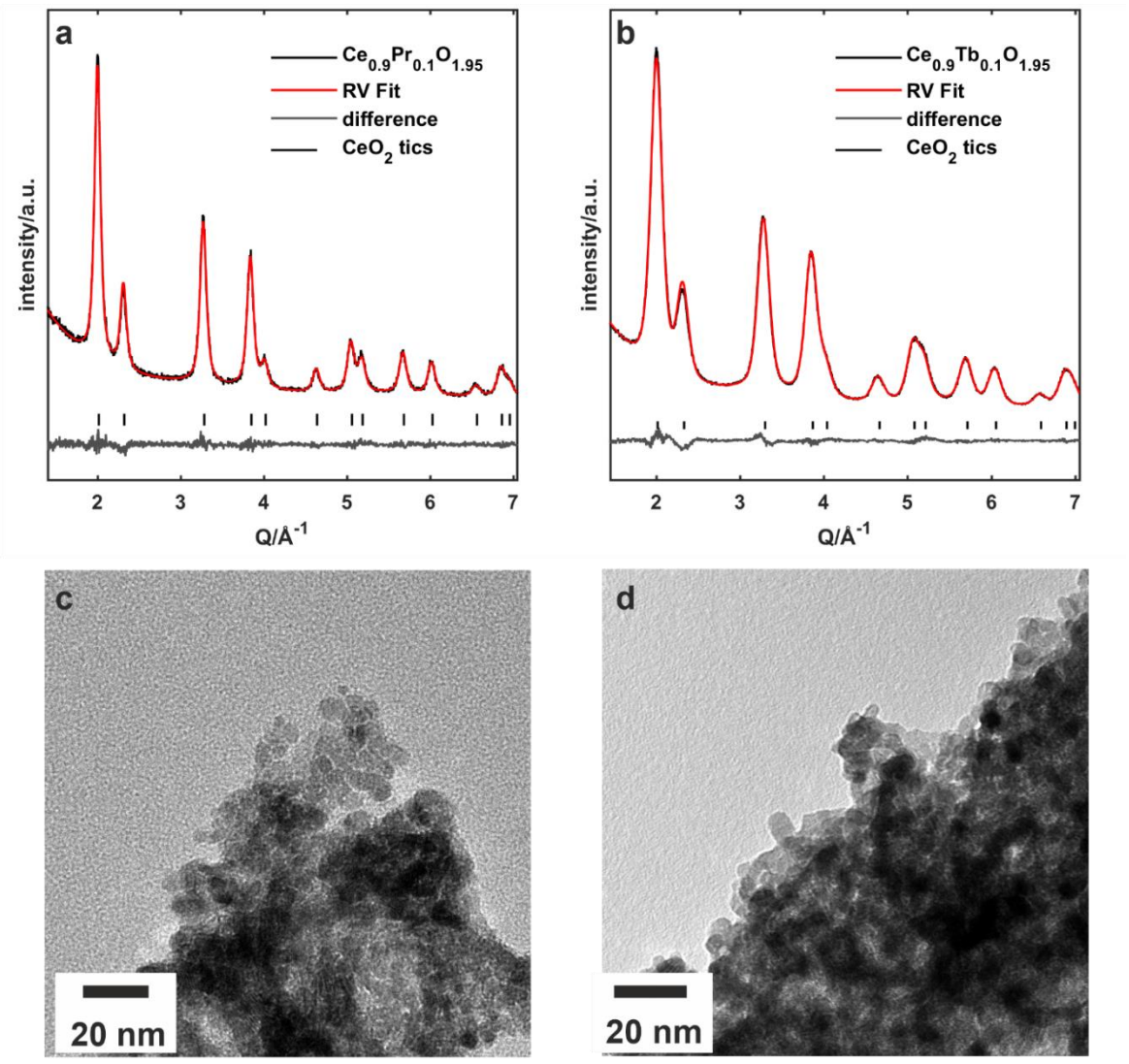

Figure 4.3. (a, b) X-ray diffractograms of $Ce_{1-x}Ln_xO_{2-x/2}$ nanoparticles (a) Ln = Pr^{3+} and (b) Ln = Tb^{3+} with x = 0.1 (experimental data (red dots), Rietveld refinement (black line) and difference plot (red line)). Reflections of ceria structure (black tics) could be indexed to the face-centered cubic cell with a = 5.4142(1) Å, R_{wp} = 2.6 %, and GoF = 1.3 for Ln = Pr^{3+} and a = 5.3938(9) Å, R_{wp} = 4.7 %, and GoF = 2.4 for Ln = Tb^{3+}. (c, d) TEM images of $Ce_{1-x}Ln_xO_{2-x/2}$ nanoparticles with (c) Tb^{3+} (x = 0.1) and (d) Pr^{3+} (x = 0.1).

The diameters of the $Ce_{1-x}Ln_xO_{2-x/2}$ nanocrystals are 7-10 nm as derived by Rietveld refinement (Table 4.1, bulk characterization), slightly larger than the average diameters of 6-7 nm derived by TEM (Figure 4.3c and d and Table 4.1, individual nanocrystals). This is a good agreement considering that X-ray diffraction is an ensemble measurement on bulk samples.

Table 4.1. Diameters of $Ce_{1-x}Ln_xO_{2-x/2}$ nanocrystals with Ln = Pr^{3+} and Ln = Tb^{3+} and x = 0.1, determined by averaging the diameters of 30 individual nanocrystals from TEM images and by Rietveld refinements of X-ray powder diffraction data.

Compound	Average particle size [nm] TEM	Average particle size [nm] P-XRD
$\mathbf{Ce_{0.9}Pr_{0.1}O_{1.95}}$	6.3±0.2	10.0±1.1
$\mathbf{Ce_{0.9}Tb_{0.1}O_{1.95}}$	6.7±0.4	7.3±0.4

To confirm that the nanoparticles are uniformly substituted and not phase-separated the nanoparticles were examined by scanning electron microscopy combined with energy-dispersive X-ray spectroscopy (SEM/EDX). The SEM/EDX mapping images for $Ce_{1-x}Ln_xO_{2-x/2}$ nanoparticles are shown in Figure S4.2 and S4.3. In order to additionally detect the presence of the lanthanides, XPS measurements were made. The XPS spectra shows signals of praseodymium and terbium (Figure S4.4, Table S4.1).

Distribution of Ln^{3+} Sites in CeO_2 Host Structure

Analysis by Electron Spin Resonance (ESR) Spectroscopy. To assess the catalytic activity of Ln-doped CeO_2 it is important to know whether the Ln^{3+} defect sites are distributed homogeneously in the bulk or at the nanocrystal surfaces. ESR spectroscopy allows to analyze the distribution of the Ln^{3+} defect sites. Ce^{4+} in the oxidation state +4 has all its *f* orbitals empty. Another possible oxidation state is +3 with a $4f^1$ occupancy which can exist as a paramagnetic defect center in CeO_2. The lanthanide ions Pr^{3+} and Tb^{3+} which are used as dopants in this study (and are assumed to be in the +3 or +4 oxidation states, as the samples are thermally treated in air) have the following *f* orbitals in high-spin configurations: Pr^{3+} ($4f^2$), Tb^{4+} ($4f^7$) and Tb^{3+} ($4f^8$).

Continuous wave ESR spectroscopy in the X-band shows significant differences between doped and pure CeO_2 (ball milling) and CeO_2 samples obtained hydrothermally (Figure 4.4). The ESR resonances of CeO_2 prepared by ball-milling (Figure 4.4) are qualitatively about one order of magnitude weaker than those of the CeO_2 prepared hydrothermally in autoclave reactions. The second important observation is that ball-milled $Ce_{1-x}Ln_xO_{2-x/2}$ nanocrystals

(with Ln = Pr^{3+} and Ln = Tb^{3+}) show intense sharp resonances which are independent of the paramagnetic dopant used. Besides, there are several broad resonances and a sharp sextet in a Tb-doped compound which originates most likely from a minor impurity of Mn(II).

How can these findings be interpreted? In CW ESR the resonances Pr^{3+} ($4f^2$), Tb^{4+} ($4f^7$) are often too broad to be observed by CW ESR and require much lower temperature to control their relaxation behavior. In other words, what can be seen here are not the dopant resonances themselves but ESR-active paramagnetic defects in CeO_2 which are indirectly related to the doping. CeO_2 attracted several previous ESR studies in which certain resonances could be assigned unambiguously (Table 4.2). Surface Ce^{3+} defects were assigned to a resonance with an axial *g*-tensor ($g_{xx} = g_{yy} = 1.9665$ and $g_{zz} = 1.9430$).[31–38] This surface defect could also be observed with other techniques such as XPS.[39] A second surface-related effect is the superoxide defect O_2^- which could be assigned because of its typical anisotropic *g*-tensor with the components $g_{xx} = 2.0655$, $g_{yy} = 2.0393$ and $g_{zz} = 2.0109$. Notice that the resolution of the resonance assigned to an O_2^- center showed a significant improvement in resolution upon cooling the sample to -170 °C (Figure 4.5).

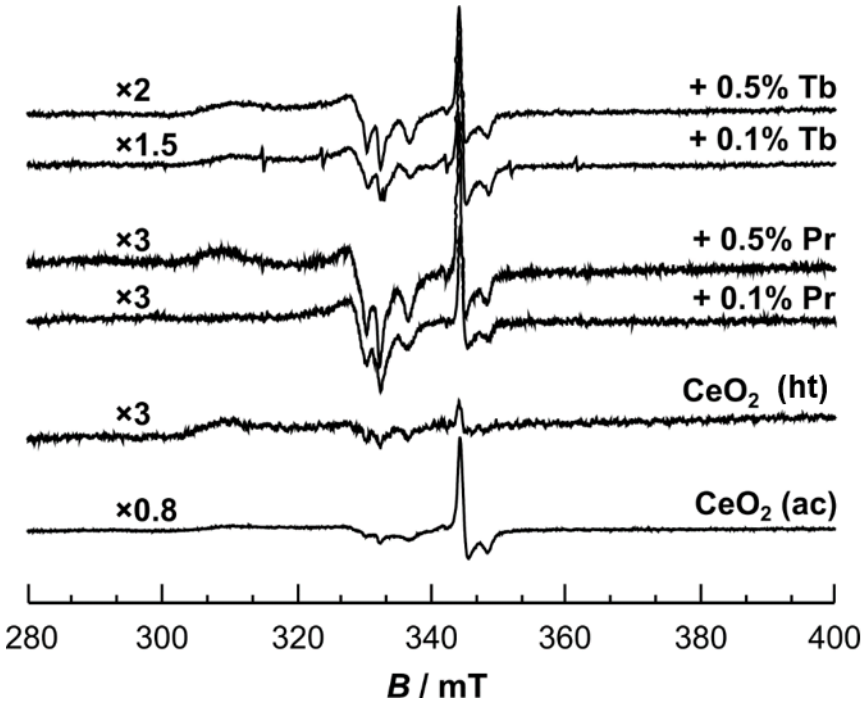

Figure 4.4. CW ESR spectra of pure CeO_2 prepared hydrothermally (bottom) and pure CeO_2, (second from bottom), Pr-doped CeO_2 and Tb-doped CeO_2 produced by ball-milling. The spectra were recorded at −170°C, *and background* was subtracted.

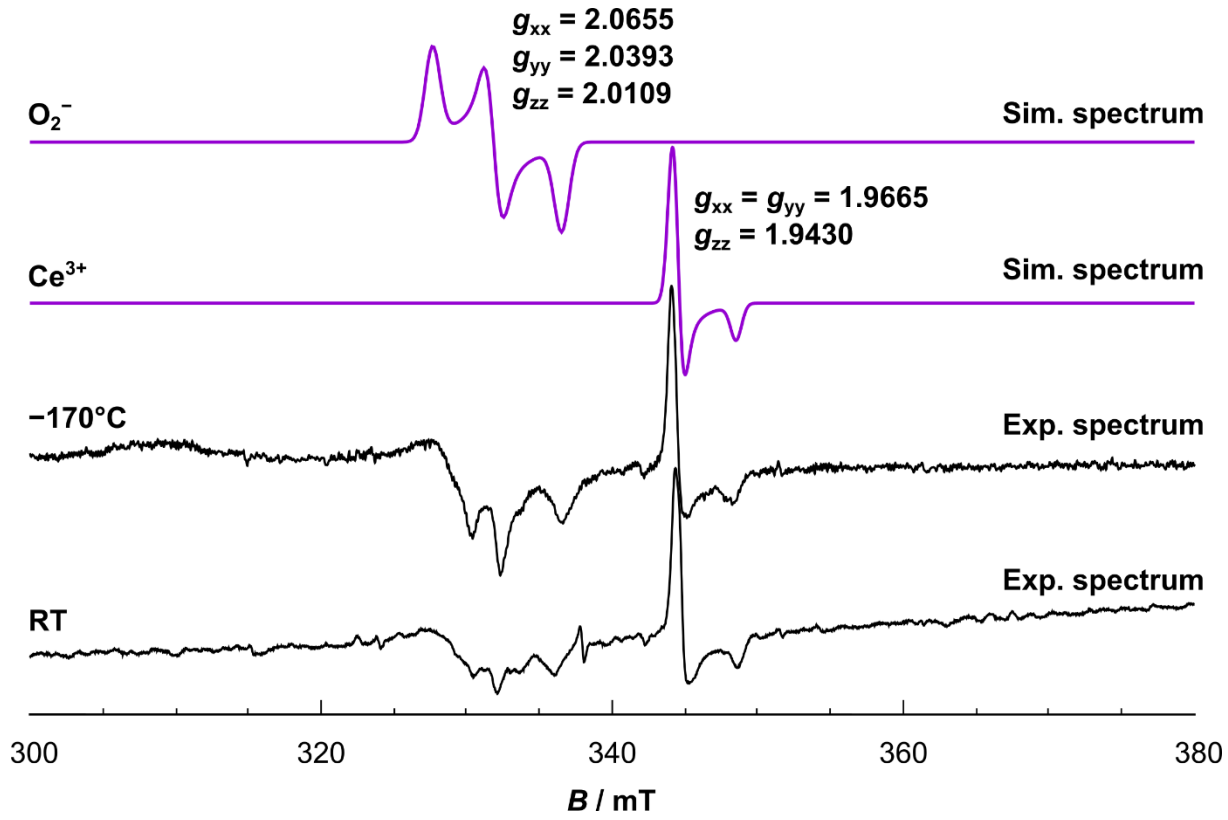

Figure 4.5. Experimental spectra of Pr-doped CeO_2 measured at RT and −170°C and simulated spectra for the two observed resonances (O_2^- and Ce^{3+}), carried out on the spectrum recorded at −170°C using the EasySpin[40] software package. For the RT spectrum, 20 scans were accumulated and averaged, while the spectrum at −170°C was a single scan.

Table 4.2. Comparison of *g*-tensor values for Ce^{3+} in CeO_2 nanocrystals prepared in this study with reference values from the literature.

Species	Spin Hamiltonian parameters			Conditions	Ref.
Ce^{3+}	$g_\perp$ = 1.967	$g_\parallel$ = 1.947		CeO_2 from $Ce(OH)_3$ oxidized at high T	41
Ce^{3+}	$g_\perp$ = 1.963	$g_\parallel$ = 1.944		Pt/CeO_2 via thermal treatment in air	42
Ce^{3+}	$g_\perp$ = 1.967	$g_\parallel$ = 1.947		CeO_2 treated at 400°C in vacuum	34
Ce^{3+}	$g_\perp$ = 1.9665	$g_\parallel$ = 1.9430		CeO_2:Pr via ball-milling and heating in air	this work
O_2^-	g_x = 2.011-2.010	g_y = 2.011-2.008	g_z = 2.003-2.048	CeO_2, Au/CeO_2, CeO_2/Al_2O_3 etc.	43
O_2^-	g_{xx} = 2.0655	g_{yy} = 2.0393	g_{zz} = 2.0109	CeO_2:Pr via ball-milling and heating in air	this work
Mn^{2+}	g = 2.000(1)	A_{iso} = 93.34 G		CeO_2 with metal oxide heated in air at 1373 K	44
Mn^{2+}	g = 2.001	A_{iso} = 257 MHz		CeO_2:Pr via ball-milling and heating in air	this work

Similar ESR signals have been seen observed for CeO_2-based materials. While the suggested models[45] to explain the ESR signals differ in detail there is agreement that the ESR signals are produced by an interaction of O_2 gas and surface-based defects. This leads to the formation of Ce^{3+} sites and oxygen-based radicals. One interpretation is that surface or subsurface oxygen vacancies ($Vo^{\bullet\bullet}$ in Kröger-Vink nomenclature) and two Ce^{3+} sites ($Ce_{Ce}^{'}$ in Kröger-Vink nomenclature) are formed,[45]

$$O_O^{\times} + 2\,Ce_{Ce}^{\times} \leftrightarrow Vo^{\bullet\bullet} + 2Ce_{Ce}^{'} + 1/2O_2\,(g) \qquad (4.3)$$

which upon addition of an O_2 molecule to a Ce^{3+} site can form a superoxide surface radical.

$$Ce_{Ce}^{'} + O_2 \leftrightarrow Ce_{Ce}^{\times}\text{-}O_2^{-} \qquad (4.4)$$

The above ESR spectra show an increase of these surface-located O-defects upon doping with Pr^{3+} and Tb^{3+} using ball-mill synthesis, which means that these dopants stabilize the catalytically important O_2^{-} radicals.

Vibrational Spectroscopy. To analyze the behavior of the ceria nanocrystals in water and to draw conclusions about their surface properties (especially the ζ-potential) in aqueous environment, FTIR studies were carried out on (i) dry powders, (ii) a drop of water, and (iii) a dry sample dispersed in water. Subsequently, the spectrum of the water was subtracted from those of the dry and water-dispersed particles (Figure S4.5, assignment of vibrational bands in Table S4.2).

Since the catalytic performance of the nanocrystals correlates with the ζ-potential,[26] the FTIR spectrum of the undoped CeO_2 nanoparticles with a potential of 15.2 mV was compared to that of the Pr-doped particles with a potential of 30.3 mV (Figure 4.6b).

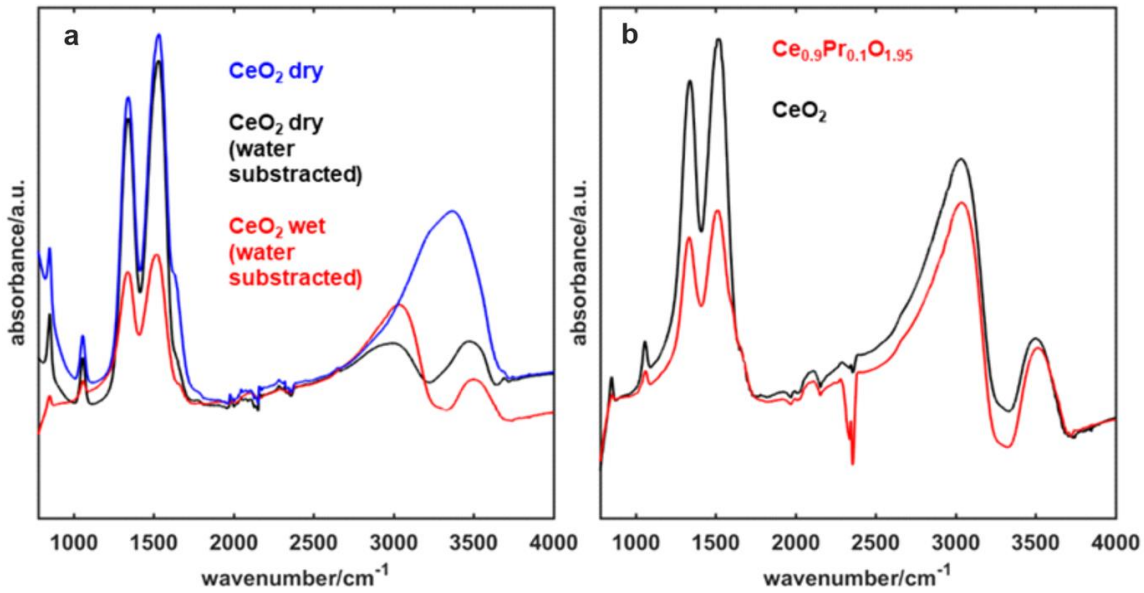

Figure 4.6. (a) FTIR spectra of ceria nanoparticles measured as a dry powder (blue), dry powder with water spectrum subtracted (black) and wet powder with water spectrum subtracted (red). (b) FTIR spectra of CeO_2 (black) and $Ce_{0.9}Pr_{0.1}O_{1.95}$ (red).

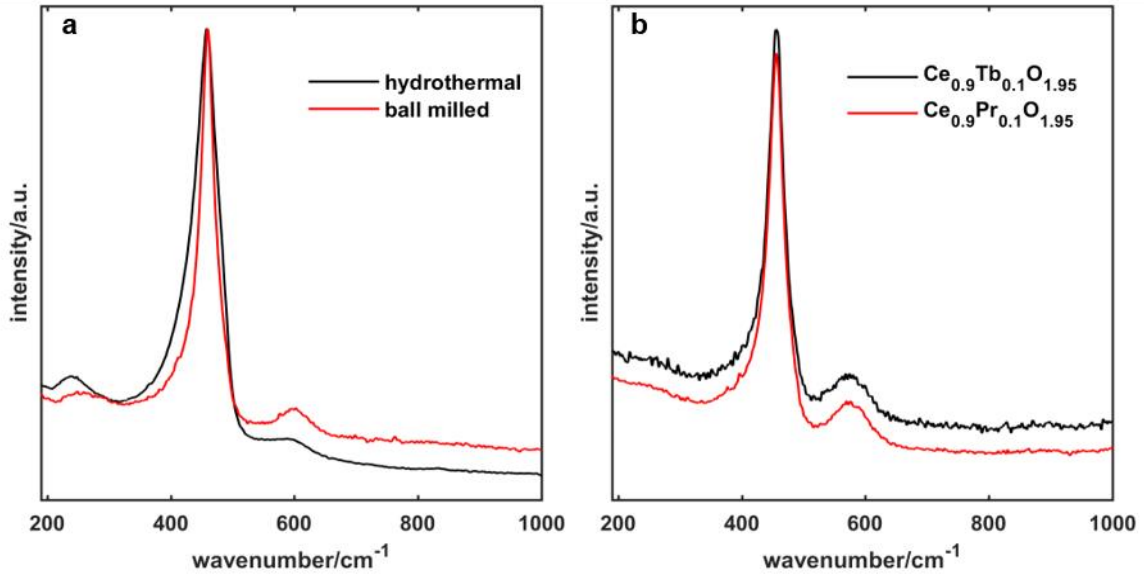

Figure 4.7. (a) Raman spectra of pure CeO_2 nanocrystals made by ball milling (red line) and hydrothermal synthesis (black line). (b) Raman spectra of $Ce_{0.9}Pr_{0.1}O_{1.95}$ nanocrystals and pure nanoceria prepared by ball milling.

The CeO_2 nanocrystals show significantly more intensive bands of the carbonate vibration modes compared to the hydroxyl groups than the Pr-doped CeO_2 ($Ce_{0.9}Pr_{0.1}O_{1.95}$) nanocrystals. Therefore, we assume that CO_2 is chemisorbed less due to Ln-doping, resulting in a more positive ζ-potential for Pr-doped $Ce_{0.9}Pr_{0.1}O_{1.95}$ nanocrystals. This may have the

following reasons: (i) The trivalent cations have a lower electron density withdrawing effect, making the surface oxide anions more affine to protons. (ii) The Ln-dopants lead to different surface facets *e.g.*, (111), (110), (100) resulting in different binding situations.

Raman spectra of undoped CeO_2 nanocrystals prepared by ball milling and hydrothermally are shown in Figure 4.7a. The main band at 460 cm^{-1} is assigned to the first-order allowed Raman mode F_{2G} in CeO_2 associated with the bulk. This band originates from a phonon mode, which can be viewed as a symmetric breathing mode of the oxide anions around each cation.[46] The position of the band is influenced by several factors. The band is assumed to experience a blue shift due to the presence of oxygen vacancies and a red shift due to a lattice expansion. However, crystal size (phonon confinement), strain or phonon anharmonicity may also contribute to the shift. The band at ~590 cm^{-1} is assigned to a convolution of the D_2 defect band attributed to a $Ce^{3+}O_7V_O$ unit and a longitudinal optical (LO) band.[47–49] The LO phonon is not Raman-allowed because of its F_{1u} symmetry. However, because of electron-phonon interactions and of the polaronic properties of CeO_2, the LO mode can be detected depending on the excitation energy, *i.e.,* the wavelength of the laser used. The band at 590 cm^{-1} is associated with oxygen defects. Taking this into account, we assume that both, ball milling and hydrothermal treatment, lead to defect formation. The expected D_1 band attributed to $Ce^{4+}O_7V_O$ defect sites may be overlaid by the broad F_{2g} band.

The Raman spectra of the Ln-doped $Ce_{0.9}Ln_{0.1}O_{1.95}$ nanocrystals (Ln = Pr, Tb) are shown in Figure 4.7b. The bands at 590 cm^{-1} are assigned again to the defect band D_1. The difference in the local and average structure in CeO_2 is linked to the presence of local strain fields. Therefore, the electron-phonon interactions, and thus the 1LO mode, are correlated with the formation of local strain around the oxygen vacancy defect caused by the dopant. The D_1 band of the Ln-doped particles is much more intense than its counterpart in the spectra of undoped CeO_2 particles. The high catalytic performance of Pr^{3+} and Tb^{3+}-doped CeO_2 nanoparticles can be attributed to the high defect density coupled with the positive surface potential (Figure S4.6+4.7, assignment of vibrational bands in Table S4.3).

Catalytic Activity

The haloperoxidase-like activity of $Ce_{1-x}Ln_xO_{2-x/2}$ (Ln = Pr, Tb) nanocrystals was analyzed to probe and compare the haloperoxidase-like activity of the mechanochemically and hydrothermally prepared $Ce_{1-x}Ln_xO_{2-x/2}$ nanozymes using the phenol red (PR) bromination assay. In this assay, phenol red (PR, phenolsulfonphtalein) is brominated oxidatively to tetrabromophenolblue (Br_4PR, 3´,3´´,5´,5´´-tetrabromphenolsulfonphtalein) in the presence

of the substrates Br^- and H_2O_2. Because both compounds have different absorption maxima (λ_{max}(PR) = 430 nm and λ_{max}(Br_4PR) = 590 nm) the kinetics of this reaction can be monitored by UV/Vis spectroscopy. Figure 4.8a shows the spectra of the $Ce_{0.9}Pr_{0.1}O_{1.95}$ nanocrystals as a function of reaction time.

Figure 4.8b shows the intensity of the maximum at 590 nm as a function of time. The bromination of PR is assumed to be a first-order reaction. The concentration c(t) of PR during the reaction can be described by the equation (c_0: initial concentration of PR, k: rate constant)

$$c(t) = c_0 \cdot \exp(-k \cdot t) \quad (4.5)$$

The concentration c_{Br} of Br_4PR is equal to the difference of the initial concentration and the current concentration of phenol red:

$$c_{Br}(t) = c_o \cdot (1-\exp(-k \cdot t)) \quad (4.6)$$

The concentration of c_{Br} of Br_4PR is proportional to the absorption (Lambert-Beer law). This equation can be used to fit the plot of the absorption maxima intensities and describe the kinetics of the reaction. This is shown for $Ce_{0.9}Pr_{0.1}O_{1.95}$ nanocrystals in Figure 4.8b.

Figure 4.8c compares of the catalytic activity of undoped CeO_2 nanocrystals synthesized by ball milling and hydrothermally. In both cases, the reaction rates are similar with k(ht) = $9 \cdot 10^{-3}$ µm min^{-1} and k(bm) = $7 \cdot 10^{-3}$ µm min^{-1}. However, doping of the nanocrystals leads to a large increase in the catalytic activity (Figure 4.8d). Tb^{3+} doping ($Ce_{0.9}Tb_{0.1}O_{1.95}$) doubled the rate constant k(Tb^{3+} doped) = $12.7 \cdot 10^{-3}$ µm min^{-1}. The activity of CeO_2 was increased by a factor of 3.5 by Pr^{3+} doping (k(Pr^{3+} doped) = $23.6 \cdot 10^{-3}$ µm min^{-1}).

The haloperoxidase like activity depends on the Br^- and the H_2O_2 concentration. Therefore, a Michaelis-Menten kinetics was performed by varying the concentration of the H_2O_2 substrate [S]. A Hill equitation (4.7) was used to fit the data.[50]

$$v = \frac{v_{max} \cdot [S]^n}{K_m{}^n + [S]^n} \quad (4.7)$$

The Michaelis constant K_m shows the affinity of the solid "nanozyme" (CeO_2, $Ce_{0.9}Pr_{0.1}O_{1.95}$ and $Ce_{0.9}Tb_{0.1}O_{1.95}$)[21,23] for the H_2O_2 substrate. v_{max} describes the maximum rate of the reaction and has the highest value of 0.498 µM min^{-1} for $Ce_{0.9}Pr_{0.1}O_{1.95}$. CeO_2 prepared by ball milling and Pr-doped ceria have approximately the same rate constants of 0.380 µM min^{-1} for CeO_2 (bm) and 0.382 µM min^{-1} for $Ce_{0.9}Tb_{0.1}O_{1.95}$. Hydrothermally prepared CeO_2 has the lowest maximum rate. As the affinity of the substrate is reciprocal to the K_m value, the following trend for the affinity to H_2O_2 is obtained: CeO_2 (ht) < CeO_2 (bm) < $Ce_{0.9}Tb_{0.1}O_{1.95}$ < $Ce_{0.9}Pr_{0.1}O_{1.95}$. The factor *n* demonstrates the cooperative effect and is

twice as large for the ceria prepared by ball milling compared to ceria synthesized hydrothermally in an autoclave reaction. Table 4.3 compiles the values for K_m, v_{max} and n.

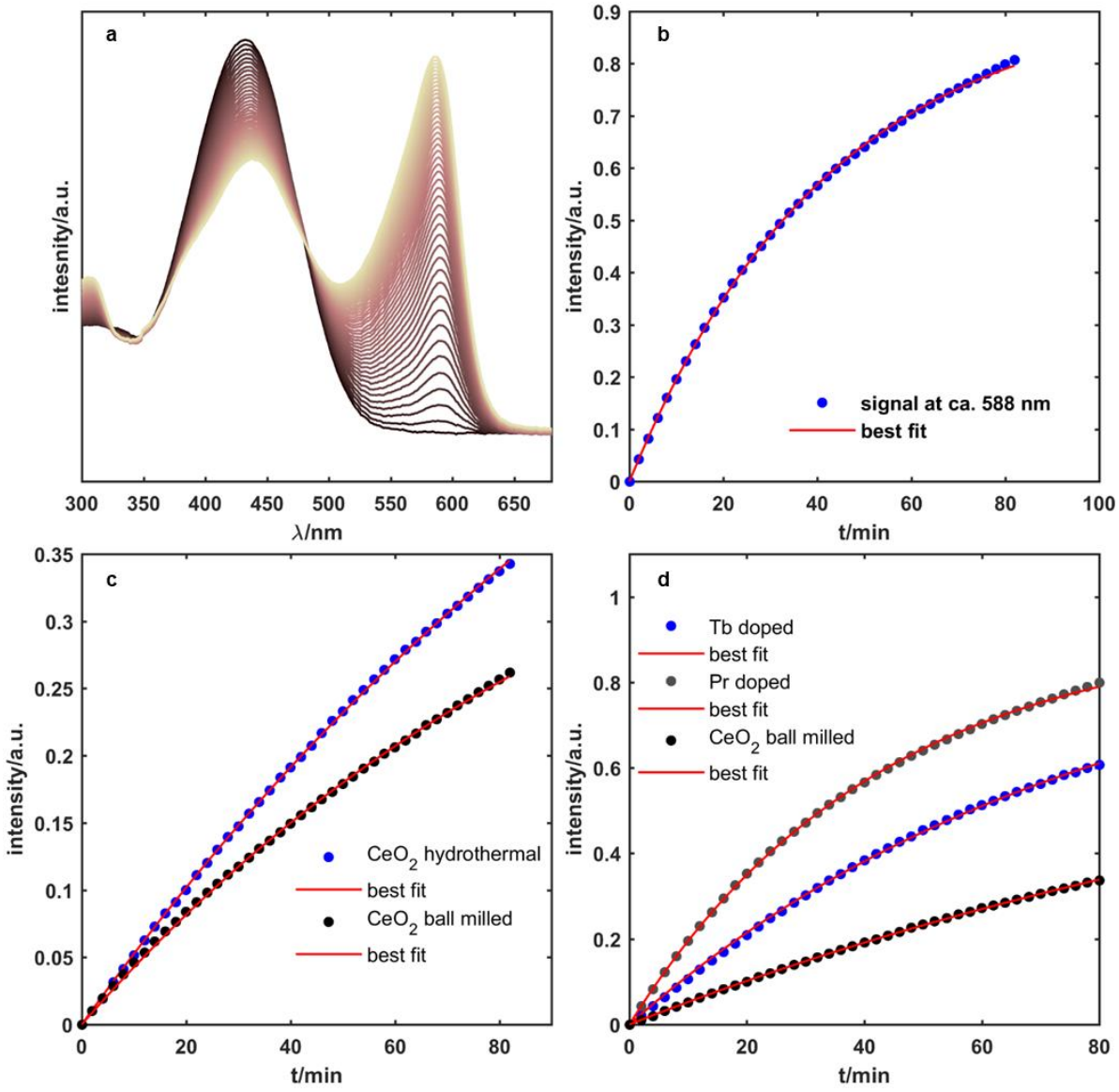

Figure 4.8. Oxidative bromination of PR. (a) Wave-dependent kinetics with the catalyst $Ce_{0.9}Pr_{0.1}O_{1.95}$ and (b) extinction at 590 nm as a function of time (90 min). (c, d) Comparison of the results of kinetic fits for ceria nanocrystals prepared by ball milling (bm, non-equilibrium) and hydrothermally (equilibrium). (c) Undoped CeO_2 nanocrystals prepared by ball milling and hydrothermally. (d) $Ce_{0.9}Ln_{0.1}O_{1.95}$ (Ln = Pr, Tb) prepared by ball milling. The red line represents the best fit.

Table 4.3. Parameters of a Michaelis-Menten analysis with H_2O_2 as substrate variable.

Sample	v_{max} / µM min^{-1}	K_m / µM	n
CeO_2 (ht)	0.347±0.049	353±130	0.950±0.208
CeO_2 (bm)	0.380±0.021	231±25	1.985±0.319
$Ce_{0.9}Tb_{0.1}O_{1.95}$	0.382±0.040	195±47	2.083±0.575
$Ce_{0.9}Pr_{0.1}O_{1.95}$	0.498±0.010	183±9	1.938±0.127

bm = ball milled ht=hydrothermal

Correlation of Catalytic Activity and Structural Properties. To understand the effect of the dopant on the catalytic activity, $Ce_{0.9}Ln_{0.1}O_{1.95}$ (Ln = Pr, Tb) nanocrystals were compared by their ζ-potential (surface potential) and their BET specific surface area. The values of the BET surface area are compiled in Table 4.4. Remarkably, the surface area of the ceria nanocrystals decreases with the doping ratio. In order to demonstrate that surface area is an important parameter for the haloperoxidase activity, the turnover rate *k* of the nanocrystals was normalized with respect to k(CeO_2 ball milled) and plotted as a function of the surface area (Figure 4.9). A correlation parameter of 0.82 indicates a good correlation. Therefore, the surface area, which represents the number of active sites of the catalyst, has a significant effect on catalytic performance.

Table 4.4. BET specific surface area for Pr- and Tb-doped CeO_2 nanocrystals (all values in m^2/g).

	x = 0	x = 0.1	x = 0.15	x = 0.2	x = 0.3
$Ce_{1-x}Pr_xO_{2-x/2}$	129.833	111.470	113.561	73.217	82.370
$Ce_{1-x}Tb_xO_{2-x/2}$	129.833	112.796	94.135	87.833	84.712

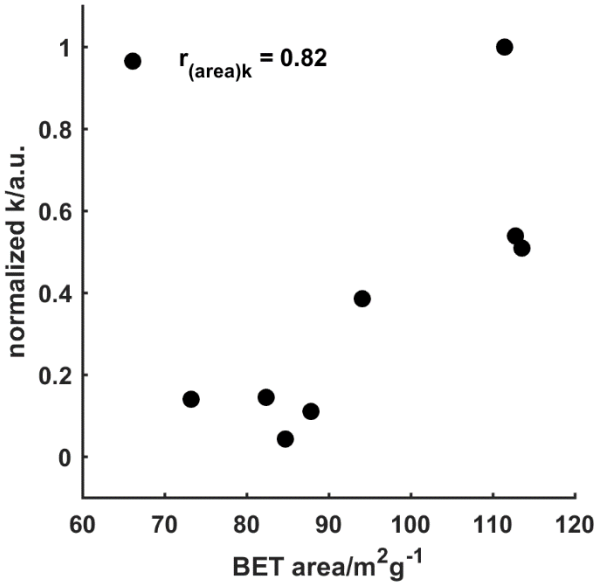

Figure 4.9. Correlation plot between the BET surface area and the turnover rate k of Pr- and Tb-doped CeO_2 nanocrystals (normalized to the turnover rate k of ball milled CeO_2).

The ζ-potential of Ln-doped CeO_2 nanocrystals increases upon doping. The highest values for the ζ-potential are reached for doping levels between 0.1 and 0.15. Remarkably, the ζ-potential shows a significantly higher correlation with the catalytic activity (Figure 4.10, Table 4.5). Therefore, a strong positive surface potential should have a crucial effect on the haloperoxidase performance of the (doped and undoped) CeO_2 nanocrystals. If sufficiently many catalytically active sites are present, the haloperoxidase performance depends on the affinity of the active (halide, peroxide) and charged (halide) species adsorbing to the particle surface.

Table 4.5. ζ-potential of Pr- and Tb-doped CeO_2 nanocrystals with different degrees of doping.

	x = 0	**x = 0.1**	**x = 0.15**	**x = 0.2**	**x= 0.3**
$Ce_{1-x}Tb_xO_{2-x/2}$	15.2 mV	23.3 mV	22.3 mV	20.3 mV	16.6 mV
$Ce_{1-x}Pr_xO_{2-x/2}$	15.2 mV	30.3 mV	16.2 mV	8.1 mV	15.5 mV

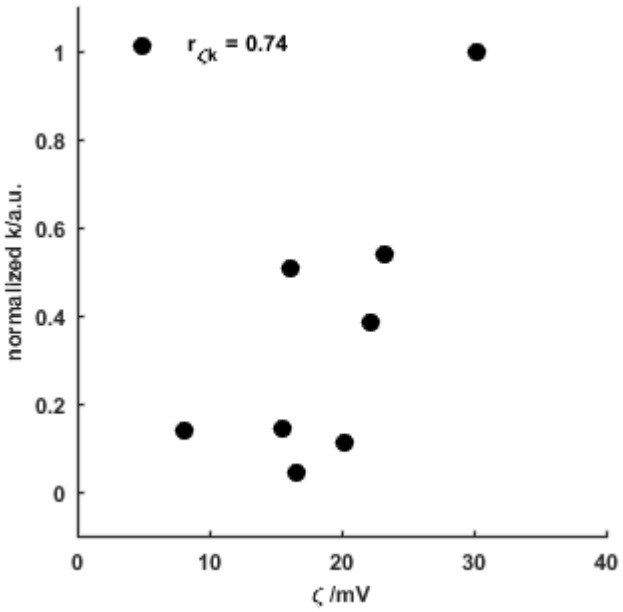

Figure 4.10. Correlation plot between the ζ-potential and the turnover rate k of Pr- and Tb-doped CeO_2 nanocrystals (normalized on the turnover rate k of ball milled CeO_2).

4.4. Experimental Section

Materials. Cerium (III) chloride heptahydrate and terbium (III) chloride hexahydrate (99%) were purchased from Alfa Aesar. Praseodymium (III) chloride hydrate were obtained from Aldrich. Sodium carbonate (99.5%, anhydrous) was purchased from Acros Organics. Cyclohexane >=99.8% was obtained from Fisher Chemical. All chemicals were used without further purification. Ultrapure water (18.2 MΩ cm-1) was used for all experiments.

Hydrothermal Synthesis of Ceria. 50 g of NaOH was dissolved in 210 mL of H_2O. 4.86 g of $Ce(NO_3)_3 \cdot 6H_2O$ was added and the solution was stirred for 30 minutes. The solution was transferred in a Teflon inlay. The Teflon inlay was placed in an autoclave and heated at 80°C for 16 h. The suspension was centrifuged for 10 min with 9000 rpm several times till the supernatant was neutral. The particles were dried at 60°C for 16 h.

Mechanochemical Synthesis of Ceria. A previous procedure[29] for submicrometer-sized CeO_2 particles was worked out to yield non-agglomerated and nanosized CeO_2 and $Ce_{1-x}Ln_xO_{2-x/2}$ particles. A total of 4 mmol of $CeCl_3 \cdot 7H_2O$ and the chloride of the appropriate trivalent dopant were weighed in in the desired molar ratio. 6 mmol of Na_2CO_3 anhydrous was added. The combined salts dispersed in 5 mL cyclohexane were treated in a planetary ball mill (Pulverisette 7 Classic, Fritsch) for 8 h with 720 rotations per minute. After milling, cyclohexane was removed and the mixture was annealed for 5 h at 400°C. After annealing, the mixture was dispersed in water and washed with water until the pH was 7. The product was dried in a vacuum desiccator.

Phenol Red Assay. 1460 µL of H_2O, 200 µL of a 250 mM KBr solution and 100 µL of a 1 mM phenol red solution were added in a cuvette. A UV/Vis spectrum was measured from 700 to 300 nm as baseline. The measurement was started by adding 50 µL of a 1 mg/mL solution of the nanoparticles and 60 µL of a 10 mM H_2O_2 solution. The measurement was repeated over a period of 90 minutes, with a spectrum measured every 2 minutes.

Michaelis Menten Kinetics. Menten kinetics were analyzed by adding different amounts of H_2O_2 to a stirred solution of phenol red, KBr and the catalyst nanoparticles. For this purpose, standard solutions of potassium bromide (250 mM) and phenol red (1 mM) were prepared separately by dissolving the appropriate amount in MQ-water under ultrasound. Then, a mixed standard solution of phenol red with potassium bromide was prepared by diluting the standard solutions. The final solution contained 50 µM of phenol red and 25 mM of bromide. From this solution 2 mL were mixed in a quartz cuvette with 62.5 µL of a nanoparticle dispersion (1 mg mL^{-1}). A 120 mM H_2O_2 standard solution was prepared as starting

solution. Diluted solutions with different concentrations of H_2O_2 were prepared from this solution. Of this, 50 µL was added to each cuvette. All kinetics were performed for 10 min reaction time and the absorbance change was measured at a wavelength of $\lambda = 590$ nm.

Bacterial Strains and Growth Conditions. *P. aeruginosa* PA14 was obtained from the lab of Dr. Max Schobert (Technische Universität Braunschweig, Germany). *P. aeruginosa* was aerobically in LB medium [1% (w/v) NaCl; 1% (w/v) tryptone; 0.5% (w/v) yeast extract] at 30 °C. For preparation of agar plates, 1.5% (w/v) agar was added to the medium.

Biofilm Assays. For quantification of bacterial biofilm production, a modified method of previously published protocols was used. [52] Briefly, P. aeruginosa was aerobically in LB medium overnight at 30°C. The cultures were then diluted in LB in a volume of 1 mL per well of a 24-well polystyrene microtiter plate (Sarstedt, Nürnbrecht) at a final Optical Density at 600 nm (OD600) of 0.5. Additionally, KBr (Roth, Karlsruhe, Germany) and H_2O_2 (Roth, Karlsruhe, Germany) at a final concentration of 32 mM and 0.8 mM, respectively, were added to the wells. Then, 28 µL of a 1 mg/mL CeO_2, $Ce_{0.9}Tb_{0.1}O_{1.95}$-, and $Ce_{0.9}Pr_{0.1}O_{1.95}$-particles dispersion were subjected. Subsequently, the microtiter plate was incubated for 72 h under gentle shaking (150 rpm) at 30°C. H_2O_2 was added stepwise at a final concentration of 0.8 mM every 24 h. Then, the plates were rinsed with water to remove the planktonic cells. After drying for 5 min, 1 mL of 1% (w/v) crystal violet (Merck, Darmstadt) was added to the wells containing the plates. After 30 min incubation at room temperature, unbound crystal violet was removed by gently submerging the plates two times in water. The plate was then air-dried over-night at room temperature. For quantification, 1 mL of 30% (v/v) acetic acid (Roth, Karlsruhe) was added to the plates to solubilize the crystal violet from the biofilm. After 15 min of incubation at room temperature, absorbance was quantified in a plate reader (Tecan, Salzburg) at 575 nm.

CHARACTERIZATION

Electron Microscopy. Samples for transmission electron microscopy (TEM) were prepared by placing a drop of dilute NP dispersion in ethanol on a carbon-coated copper grid. TEM images were obtained with a FEI Tecnai 12 TWIN LaB_6 at 120 kV together with a Gatan US1000 CCD-camera (16-bit, 2048 x 2048 pixels) using the Gatan Digital Micrograph software.

Samples for scanning electron microscopy (SEM) were prepared with carbon film pads on aluminum holders. A silicon wafer was used for the sample preparation and fixed on the

carbon pad. The sample was dispersed on ethanol (c=1 mg/mL) and placed on the silica wafer. SEM images were obtained using a FEI Nova NanoSEM 630 equipped with an EDAX-Pegasus X4M unit for the EDX measurements. The acceleration voltage was set to 5 kV. The elemental composition was calculated using the EDAX Genesis Software Suite.

Powder X-ray Diffraction. X-ray diffraction patterns were recorded on a STOE Stadi P diffractometer equipped with a Dectris My-then 1k detector in transmission mode using Mo Kα1 radiation. Crystalline phases were identified according to the PDF–2 database using Bruker AXS EVA 10.0 software. Rietveld refinement[53] and Pawley fitting[54] was performed with Topas Academic V6 using the fundamental parameters approach.[55]

UV/Vis. UV/Vis measurements were conducted with an Agilent Cary 3500 and Cary 5G.

Zeta Potential. Zetapotentials were measured on a Malvern Zetasizer Nano using disposable capillary cells (DTS1070) and single-use polystyrene cuvettes. Data analysis was performed with Malvern Zetasizer Software 8.01.4906.

BET Surface Area. BET measurements were conducted with 3P Micro 300 gas adsorption instrument using nitrogen as the analysis gas at 77.4 K. The software 3P Surface Area & Pore Size Analyzer System 10.03.02 was used to analyze the recorded data.

Raman Spectroscopy. The Raman spectra were recorded with a Bruker Senterra Microscope and the *OPUS* software.

ATR-FTIR Spectroscopy. The attenuated total reflection (ATR) FTIR spectra were recorded on a TENSOR II spectrometer (Bruker) using a Platinum ATR unit.

ESR Spectroscopy. ESR measurements were carried out using an X-band MiniScope MS5000 CW spectrometer (Freiberg Instruments) with a field homogeneity of ±5 μT within the sample region, 0.2 mT field modulation and 100 kHz modulation frequency. The samples were filled in 200 μL capillaries and were irradiated at 10 mW RF power and 9.47 GHz frequency acquiring 20 scan for 1000 s at RT. The magnetic field B_0 range was chosen from 280 to 400 mT. The *g*-factors and other spin parameters for the selected samples were determined using the software package EasySpin 5.2.28.[40]

X-ray photoelectron spectroscopy (XPS). XPS measurements were carried out on an Axis Ultra DLD imaging photoelectron spectrometer. Measurements were carried out using the Hybrid mode with 10 mA and 15 kV at the Al anode. The analysis area was 700 μm × 300 μm (i.e., X-ray spot size). Survey spectra were measured at a pass energy of 80 eV and elemental spectra at 20 eV pass energy of the analyzer. All spectra were charge corrected to a binding energy of 284.8 eV for the C 1s line corresponding to adventitious aliphatic carbon. Measurements were analyzed using the CasaXPS software plotted with Origin 8.1.

4.5. Conclusions

We have demonstrated that the halogenation activity of CeO_2 can be enhanced strongly by Ln^{3+} substitution of Ce^{4+} in $Ce_{1-x}Ln_xO_{2-x/2}$. Non-agglomerated nanosized $Ce_{1-x}Ln_xO_{2-x/2}$ (Ln = Pr, Tb) was prepared in copious amounts *via* a $Na_4Ce_2(CO_3)_5$ reaction intermediate in a mechanochemical metathesis reaction of 2 $CeCl_3 \cdot 7\ H_2O$ + 5 Na_2CO_3 -> $Na_4Ce_2(CO_3)_5$ + 6 NaCl + 14 H_2O. Ceria nanocrystals with diameters < 10 nm were obtained after short calcination (5 h) of the as-milled powder at 400°C, washing with deionized water, and drying *in vacuo*. The NaCl byproduct of the mechanochemical metathesis reaction plays an important role for the formation of nanosized ceria by inhibiting agglomeration through matrix effects.

There is virtually no solubility limit for incorporating Tb^{3+} in the CeO_2 host in mechanochemical reactions. Doping with Pr^{3+} was obtained up to a precipitation rate of 70%. The ball-milling access and the low annealing temperature are good anchor points for upscaling the synthesis to pilot plant scale. ESR spectroscopy showed an increase in the number of paramagnetic defects induced by doping. The presence of Pr^{3+} and Tb^{3+} during the synthesis promoted the formation of Ce^{3+} and O_2^- defects at the CeO_2 nanocrystal surface.

Using vibrational spectroscopy we could unravel the surface chemistry of nanoceria and Ln-doped nanoceria. Although Ln-substituted nanoceria such as $Ce_{0.9}Pr_{0.1}O_{1.95}$ had a lower BET surface area than binary CeO_2 nanocrystals, their catalytic activity, calibrated through the oxidative bromination of phenol red, was much higher than that of unsubstituted CeO_2 nanocrystals because the ζ-potential increased from 15 mV (for CeO_2) to 30 mV (for $Ce_{0.9}Pr_{0.1}O_{1.95}$), which facilitated the adsorption of the bromide substrate from water. The combined effect (expressed through the product of surface area (S_{BET}) and ζ-potential) reaches an optimum value for $Ce_{0.9}Pr_{0.1}O_{1.95}$ and explains the high activity of the Ln-substituted CeO_2 nanocatalysts. The required concentrations of the substrates Br^- and H_2O_2 for the haloperoxidase-like reactions are as low as milli- and micromolar. These concentrations are comparable to bromide concentrations present in body fluids of animals and plants and to H_2O_2 concentrations generated in daylight.[51] This makes Ln-doped ceria a potent and "green" nanoparticle haloperoxidase mimic (e.g., for use in antifouling applications) because no chemicals other than ubiquitous bromide and H_2O_2 (generated in daylight) are required and no substances other than those generated in natural metabolic processes of plants are released into the environment. Therefore, Ln-doped nanoceria may

partially replace potent - but toxic - antifouling biocides. As ceria is a by-product of lanthanide production, the costs of bulk ceria (~1000 $ per ton) make only a small contribution to the total costs. Mechanochemical synthesis enables energy-saving and residue-free production of Ln-doped nanoceria in large industrial quantities. A biomimicry approach that allows the substitution of conventional biocides or costly enzymatic preservation systems by stable, non-toxic and highly abundant rare earth oxides would be a significant step towards a sustainable antifouling solution.

4.6. References

1. T. Montini, M. Melchionna, M. Monai, P. Fornasiero, Fundamentals and Catalytic Applications of CeO_2-Based Materials. *Chem. Rev.* 2016. **116**, 5987–6041.

2. A. Trovarelli, Catalytic Properties of Ceria and CeO2-Containing Materials. *Catal. Rev.* 1996. **38**, 439–520.

3. W. Wang, S. Wang, X. Ma, J. Gong, Recent advances in catalytic hydrogenation of carbon dioxide. *Chem. Soc. Rev.* 2011. **40**, 3703–3727.

4. A. Le Gal, S. Abanades, Dopant Incorporation in Ceria for Enhanced Water-Splitting Activity during Solar Thermochemical Hydrogen Generation. *J. Phys. Chem. C*. 2012. **116**, 13516–13523.

5. S. Park, J.M. Vohs, R. Gorte, Direct oxidation of hydrocarbons in a solid-oxide fuel cell. *Nature*. 2000. **404**, 265–267.

6. C. Walkey, S. Das, S. Seal, J. Erlichman, K. Heckman, L. Ghibelli, E. Traversa, J. F. McGinnis, W. T. Self, Catalytic properties and biomedical applications of cerium oxide nanoparticles. *Environ. Sci. Nano*. 2015. **2**, 33–53.

7. K. Korschelt, M. N. Tahir, W. Tremel, A Step into the Future: Applications of Nanoparticle Enzyme Mimics. *Chem. – A Eur. J.* 2018. **24**, 9703–9713.

8. K. Herget, P. Hubach, S. Pusch, P. Deglmann, H. Götz, T. E. Gorelik, I. A. Gural'skiy, F. Pfitzner, T. Link, S. Schenk, M. Panthöfer, V. Ksenofontov, U. Kolb, T. Opatz, R. André, W. Tremel, Haloperoxidase Mimicry by CeO_{2-x} Nanorods Combats Biofouling. *Adv. Mater*. 2017. **29**, 1603823.

9. F. Caputo, M. De Nicola, A. Sienkiewicz, A. Giovanetti, I. Bejarano, S. Licoccia, E. Traversa, L. Ghibelli, Cerium oxide nanoparticles, combining antioxidant and UV shielding properties, prevent UV-induced cell damage and mutagenesis. *Nanoscale*. 2015. **7**, 15643–15656.

10. E. Laubender, N. B. Tanvir, O. Yurchenko, G. Urban, Nanocrystalline CeO2 as Room Temperature Sensing Material for CO2 in Low Power Work Function Sensors. *Procedia Eng.* 2015. **120**, 1058–1062.

11. H.-C. Flemming, J. Wingender, U. Szewzyk, P. Steinberg, S. A. Rice, S. Kjelleberg, Biofilms: an emergent form of bacterial life. *Nat. Rev. Microbiol.* 2016. **14**, 563–575.

12. C. M. Waters, B. L. Bassler, Quorum sensing: cell-to-cell communication in bacteria. *Annu. Rev. Cell Dev. Biol.* 2005. **21**, 319–346.

13. R. Wever, M. A. van der Horst, The role of vanadium haloperoxidases in the formation of volatile brominated compounds and their impact on the environment. *Dalt. Trans.* 2013. **42**, 11778–11786.

14. V. Conte, B. Floris, Vanadium and molybdenum peroxides: synthesis and catalytic activity in oxidation reactions. *Dalt. Trans.* 2011. **40**, 1419–1436.

15. N. Madaan, N. R. Shiju, G. Rothenberg, Predicting the performance of oxidation catalysts using descriptor models. *Catal. Sci. Technol.* 2015. **6**, 125–133.

16. A. Butler, M. Sandy, Mechanistic considerations of halogenating enzymes. *Nature*. 2009. **460**, 848–854.

17. V. Agarwal, Z. D. Miles, J. M. Winter, A. S. Eustáquio, A. A. El Gamal, B. S. Moore, Enzymatic Halogenation and Dehalogenation Reactions: Pervasive and Mechanistically

Diverse. *Chem. Rev.* 2017. **117**, 5619–5674.

18. F. Natalio, R. André, A. F. Hartog, B. Stoll, K. P. Jochum, R. Wever, W. Tremel, Vanadium pentoxide nanoparticles mimic vanadium haloperoxidases and thwart biofilm formation. *Nat. Nanotechnol*. 2012. **7**, 530–535.

19. K. Herget, H. Frerichs, F. Pfitzner, M. N. Tahir, W. Tremel, Functional Enzyme Mimics for Oxidative Halogenation Reactions that Combat Biofilm Formation. *Adv. Mater.* 2018. **30**, 1707073.

20. A. Karakoti, S. Singh, J. M. Dowding, S. Seal, W. T. Self, Redox-active radical scavenging nanomaterials. *Chem. Soc. Rev.* 2010. **39**, 4422–4432.

21. H. Wei, E. Wang, Nanomaterials with enzyme-like characteristics (nanozymes): next-generation artificial enzymes. *Chem. Soc. Rev.* 2013. **42**, 6060–6093.

22. J. Wu, X. Wang, Q. Wang, Z. Lou, S. Li, Y. Zhu, L. Qin, H. Wei, Nanomaterials with enzyme-like characteristics (nanozymes): next-generation artificial enzymes (II). *Chem. Soc. Rev.* 2019. **48**, 1004–1076.

23. X. Yan, Ed., Nanozymology: Connecting Biology and Nanotechnology (Springer Singapore)

24. R. Schmitt, A. Nenning, O. Kraynis, R. Korobko, A. I. Frenkel, I. Lubomirsky, S. M. Haile, J. L. M. Rupp, A review of defect structure and chemistry in ceria and its solid solutions. *Chem. Soc. Rev.* 2020. **49**, 554–592.

25. V. Baldim, F. Bedioui, N. Mignet, I. Margaill, J.-F. Berret, The enzyme-like catalytic activity of cerium oxide nanoparticles and its dependency on Ce3+ surface area concentration. *Nanoscale*. 2018. **10**, 6971–6980.

26. H. Frerichs, E. Pütz, F. Pfitzner, T. Reich, A. Gazanis, M. Panthöfer, J. Hartmann, O. Jegel, R. Heermann, W. Tremel, Nanocomposite antimicrobials prevent bacterial growth through the enzyme-like activity of Bi-doped cerium dioxide ($Ce_{1-x}Bi_xO_{2-\delta}$). *Nanoscale*. 2020. **12**, 21344–21358

27. K. Korschelt, R. Schwidetzky, F. Pfitzner, J. Strugatchi, C. Schilling, M. Von Der Au, K. Kirchhoff, M. Panthöfer, I. Lieberwirth, M. N. Tahir, C. Hess, B. Meermann, W. Tremel, CeO2−x nanorods with intrinsic urease-like activity. *Nanoscale*. 2018. **10**, 13074–13082.

28. V. Šepelák, A. Düvel, M. Wilkening, K.-D. Becker, P. Heitjans, Mechanochemical reactions and syntheses of oxides. *Chem. Soc. Rev.* 2013. **42**, 7507.

29. Y. X. Li, W. F. Chen, X. Z. Zhou, Z. Y. Gu, C. M. Chen, Synthesis of CeO2 nanoparticles by mechanochemical processing and the inhibiting action of NaCl on particle agglomeration. *Mater. Lett.* 2005. **59**, 48–52.

30. C. C. Koch, The Synthesis of Non-Equilibrium Structures by Ball-Milling. *Mater. Sci. Forum*. 1992. **88-90**, 243–262.

31. E. Abi-Aad, J. Matta, R. Flouty, C. Decarne, S. Siffert, A. Aboukaïs, in *Magnetic Resonance in Colloid and Interface Science*, J. Fraissard, O. Lapina, Eds. (Springer Netherlands, Dordrecht), *NATO Science Series*, pp. 479–484.

32. Z. Qu, F. Yu, X. Zhang, Y. Wang, J. Gao, Support effects on the structure and catalytic activity of mesoporous Ag/CeO2 catalysts for CO oxidation. *Chem. Eng. J.* 2013. **229**, 522–532.

33. T. Vinodkumar, D. N. Durgasi, S. Maloth, B. M. Reddy, Tuning the structural and catalytic properties of ceria by doping with Zr4+, La3+ and Eu3+ cations. *J. Chem. Sci.* 2015. **127**,

1145–1153.

34. M. Skaf, S. Aouad, S. Hany, R. Cousin, E. Abi-Aad, A. Aboukaïs, Physicochemical characterization and catalytic performance of 10% Ag/CeO2 catalysts prepared by impregnation and deposition–precipitation. *J. Catal.* 2014. **320**, 137–146.

35. Y. Liu, C. Wen, Y. Guo, G. Lu, Y. Wang, Effects of surface area and oxygen vacancies on ceria in CO oxidation: Differences and relationships. *J. Mol. Catal. A Chem.* 2010. **316**, 59–64.

36. K. Kappis, C. Papadopoulos, J. Papavasiliou, J. Vakros, Y. Georgiou, Y. Deligiannakis, G. Avgouropoulos, Tuning the Catalytic Properties of Copper-Promoted Nanoceria via a Hydrothermal Method. *Catalysts*. 2019. **9**, 138.

37. D. Gamarra, A. L. Cámara, M. Monte, S. B. Rasmussen, L. E. Chinchilla, A. B. Hungría, G. Munuera, N. Gyorffy, Z. Schay, V. C. Corberán, J. C. Conesa, A. Martínez-Arias, Preferential oxidation of CO in excess H2 over CuO/CeO2 catalysts: Characterization and performance as a function of the exposed face present in the CeO2 support. *Appl. Catal. B Environ.* 2013. **130-131**, 224–238.

38. J. Xu, J. Harmer, G. Li, T. Chapman, P. Collier, S. Longworth, S. Chi Tsang, Size dependent oxygen buffering capacity of ceria nanocrystals. *Chem. Commun.* 2010. **46**, 1887–1889.

39. X. Liu, K. Zhou, L. Wang, B. Wang, Y. Li, Oxygen Vacancy Clusters Promoting Reducibility and Activity of Ceria Nanorods. *J. Am. Chem. Soc.* 2009. **131**, 3140–3141.

40. S. Stoll, A. Schweiger, EasySpin, a comprehensive software package for spectral simulation and analysis in EPR. *J. Magn. Reson.* 2006. **178**, 42–55.

41. E. Abi-aad, R. Bechara, J. Grimblot, A. Aboukais, Preparation and characterization of ceria under an oxidizing atmosphere. Thermal analysis, XPS, and EPR study. *Chem. Mater.* 1993. **5**, 793–797.

42. L. Mendelovich, H. Tzehoval, M. Steinberg, The adsorption of oxygen and nitrous oxide on platinum ceria catalyst. *Appl. Surf. Sci.* 1983. **17**, 175–188.

43. P. Lakshmanan, F. Averseng, N. Bion, L. Delannoy, J.-M. Tatibouët, C. Louis, Understanding of the oxygen activation on ceria- and ceria/alumina-supported gold catalysts: a study combining 18O/16O isotopic exchange and EPR spectroscopy. *Gold Bull.* 2013. **46**, 233–242.

44. M. Figaj, K. D. Becker, An electron paramagnetic resonance study of impurities in ceria, CeO2. *Solid State Ionics*. 2001. **141-142**, 507–512.

45. X. Zhao, M. D. Susman, J. D. Rimer, P. Bollini, Synthesis, Structure and Catalytic Properties of Faceted Oxide Crystals. *ChemCatChem*. 2021. **13**, 6–27.

46. J. R. McBride, K. C. Hass, B. D. Poindexter, W. H. Weber, Raman and x-ray studies of $Ce_{1-x}RE_xO_{2-y}$, where RE=La, Pr, Nd, Eu, Gd, and Tb. *J. Appl. Phys.* 1994. **76**, 2435–2441.

47. A. Nakajima, A. Yoshihara, M. Ishigame, Defect-induced Raman spectra in doped CeO 2. *Phys. Rev. B.* 1994. **50**, 13297–13307.

48. C. Schilling, A. Hofmann, C. Hess, M. Veron, Raman Spectra of Polycrystalline CeO2: A Density Functional Theory Study. *J. Phys. Chem. C.* 2017, **121**, 20834-20849.

49. O. Kraynis, I. Lubomirsky, T. Livneh, Resonant Raman Scattering in Undoped and Lanthanide-Doped CeO_2. *J. Phys. Chem. C.* 2019. **123**, 24111–24117.

50. S. Goutelle, M. Maurin, F. Rougier, X. Barbaut, L. Bourguignon, M. Ducher, P. Maire, The Hill equation: a review of its capabilities in pharmacological modelling. *Fundam. Clin. Pharmacol.* 2008. **22**, 633–648.

51. W. J. Cooper, R. G. Zika, R. G. Petasne, J. M. C. Plane, Photochemical formation of hydrogen peroxide in natural waters exposed to sunlight. *Environ. Sci. Technol.* 1988. **22**, 1156–1160.

52. G. A. O'Toole, Microtiter dish biofilm formation assay. *J. Vis. Exp.* . 2011, 2437.

53. H. M. Rietveld, A profile refinement method for nuclear and magnetic structures. *J. Appl. Crystallogr.* 1969. **2**, 65–71.

54. G. S. Pawley, Unit-cell refinement from powder diffraction scans. *J. Appl. Crystallogr.* 1981. **14**, 357–361.

55. A. A. Coelho, *TOPAS* and *TOPAS-Academic* : an optimization program integrating computer algebra and crystallographic objects written in C++. *J. Appl. Crystallogr.* 2018. **51**, 210–218.

4.7. Supporting Information

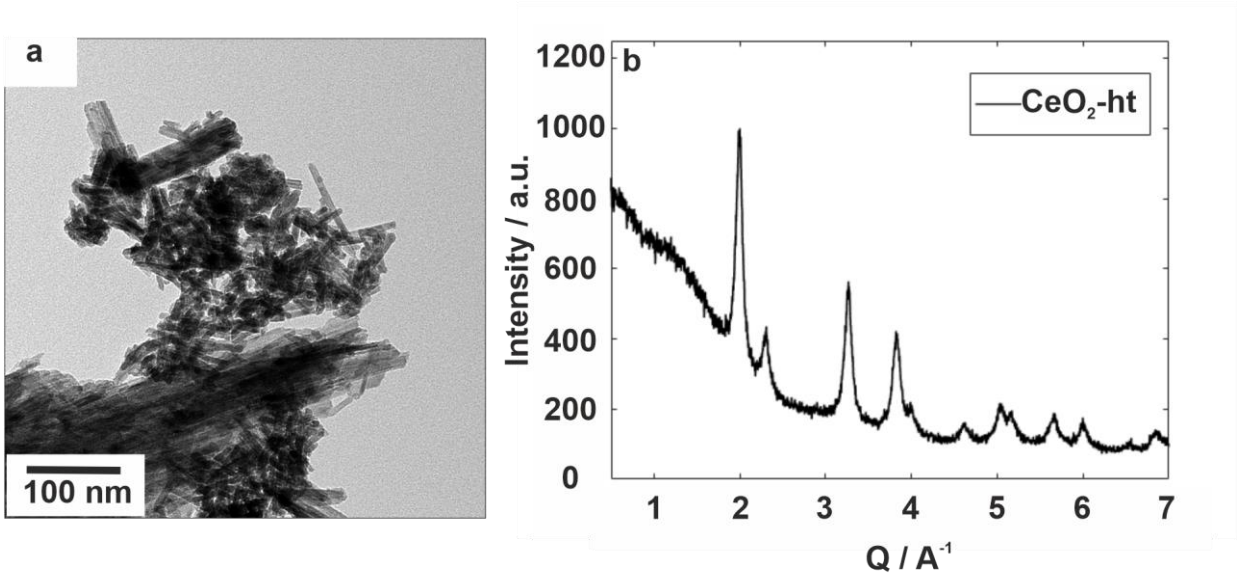

Figure S 4.1. a) TEM image and b) X-ray diffractogram of hydrothermally prepared CeO_2 nanocrystals.

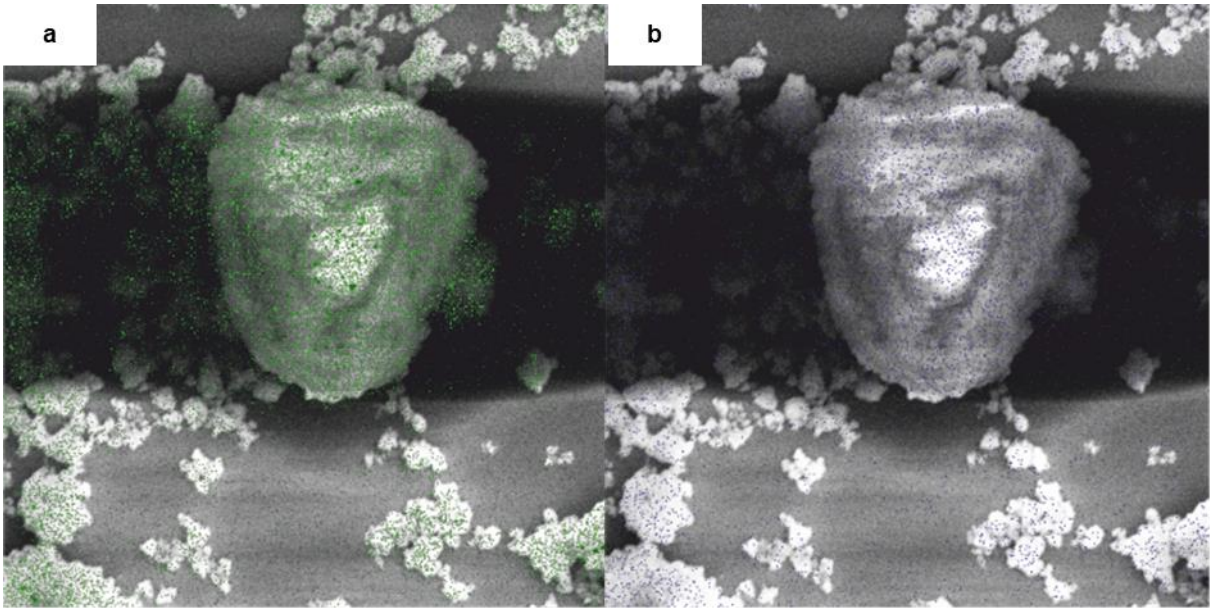

Figure S 4.2. SEM EDX mapping of Tb-doped CeO_2 nanocrystals. a) X-rays for the Ce L line b) X-rays for the Tb L line.

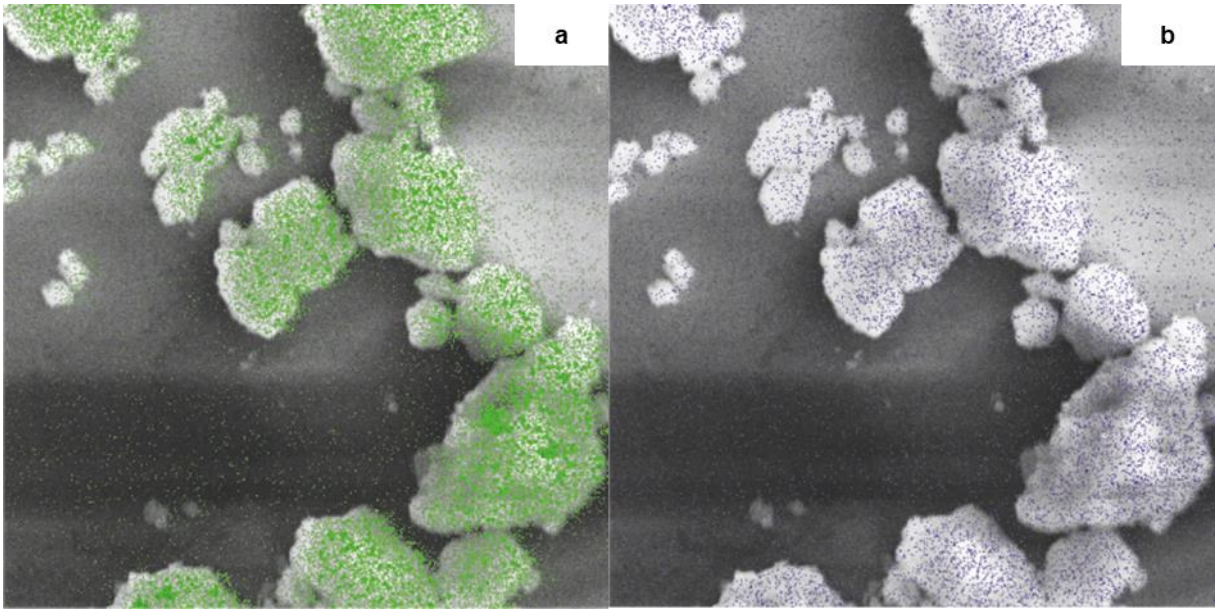

Figure S 4.3. SEM EDX mapping of the Pr-doped nanocrystals. a) X-rays for the Ce L line b) X-rays for the Pr L line.

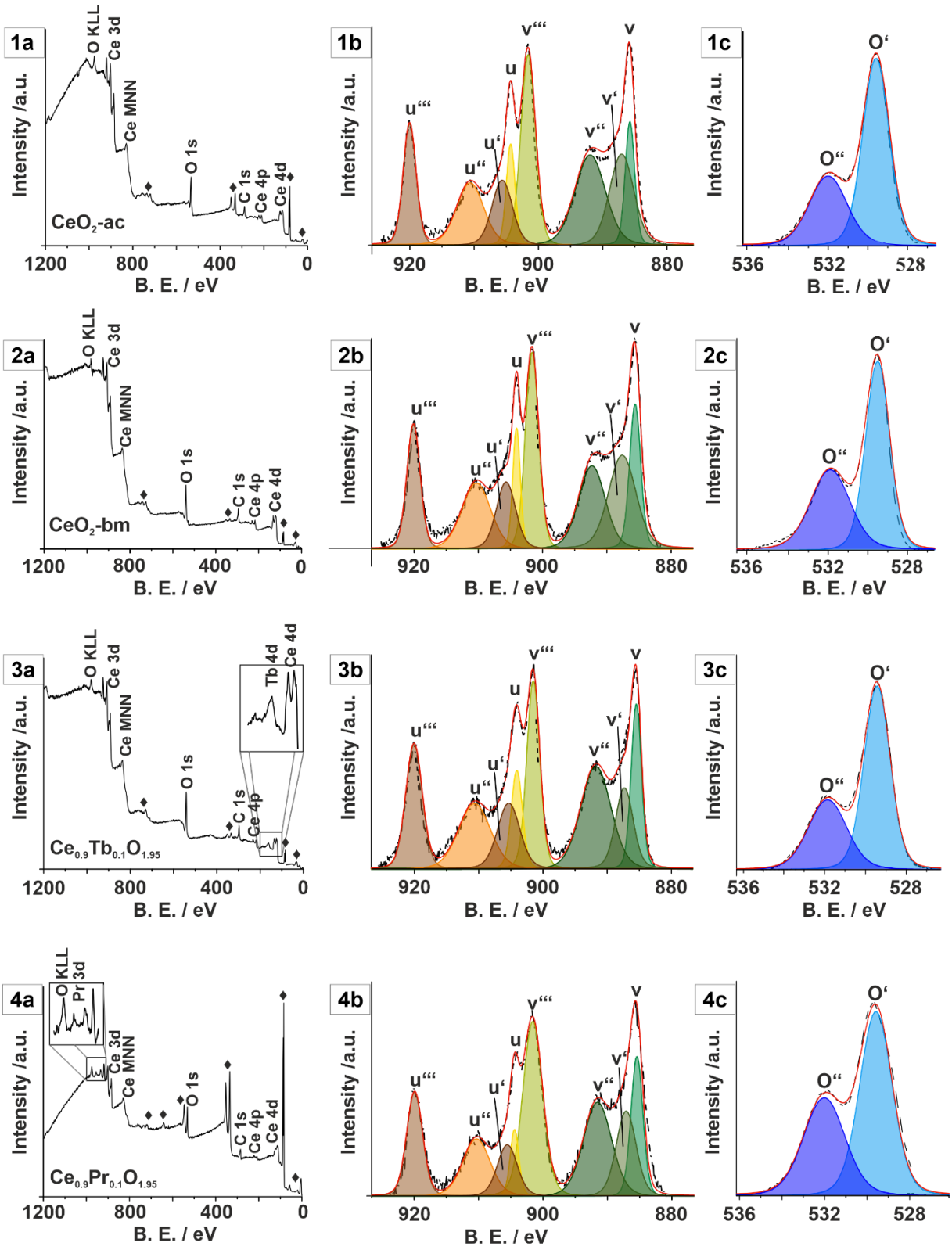

Figure S 4.4. X-ray photoelectron spectroscopy spectra of CeO_2-ac (1), CeO_2-bm (2), $Ce_{0.9}Tb_{0.1}O_{1.95}$ (3) and $Ce_{0.9}Pr_{0.1}O_{1.95}$ (4). a) shows the survey spectra of the samples. b) shows the Ce 3d and c) the O 1s region. [1–4]

Table S 4.1. Table of the signals in the XPS survey spectra in Figure S4.4. [1–4]

Peak Energy / eV	Element	Peak Assignment	Shortcut
40	Au 5p	-	♦
85	Au 4f		♦
88	Au 4f	-	♦
122	Ce 4d	Ce(IV) in CeO_2	-
125	Ce 4d	Ce(IV) in CeO_2	-
155	Tb 4d	-	-
285	C 1s	-	-
~340	Au 4d	-	♦
~355	Au 4d	-	♦
530	O 1s	Ce(IV)-O	O’
532	O 1s	Ce(III)-O and adsorbed $–CO_3^{2-}$ species	O’’
~560	Au 4p	-	♦
~650	Au 4p	-	♦
~770	Au 4s	-	♦
883	Ce $3d_{5/2}$	Ce(IV) in CeO_2	v
885	Ce $3d_{5/2}$	Ce(III) in CeO_{2-x}	v’
889	Ce $3d_{5/2}$	Ce(IV) in CeO_2	v’’
899	Ce $3d_{5/2}$	Ce(IV) in CeO_2	v’’’
901	Ce $3d_{3/2}$	Ce(IV) in CeO_2	u
904	Ce $3d_{3/2}$	Ce(III) in CeO_{2-x}	u’
908	Ce $3d_{3/2}$	Ce(IV) in CeO_2	u’’
917	Ce $3d_{3/2}$	Ce(IV) in CeO_2	u’’’
933	Pr $3d_{5/2}$	-	-
954	Pr $3d_{3/2}$	-	-

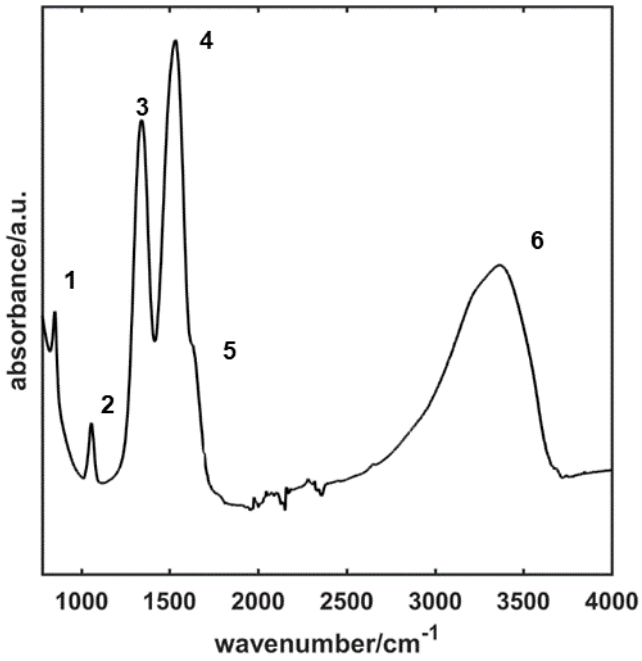

Figure S 4.5. FTIR spectrum of ball milled CeO_2. The bands marked with numbers are shown in Table S4.1.

Table S 4.2. Assignment of the FTIR vibrational bands. The first five bands are assigned to chemisorbed CO_2. The sixth broad band is assigned to OH groups of free and adsorbed water.

No. of FTIR band	Position(cm^{-1})	Assignments
1	851	Out of-plane vibration of the surface carbonate CO_3^{2-} group,
2	1058	unidentate CO_3^{2-}
3	1341	unidentate CO_3^{2-}
4	1534	bidentate CO_3^{2-}
5	1633	bending vibration of water
6	2800-3650	υ_{-OH} of free, adsorbed and chemisorbed water

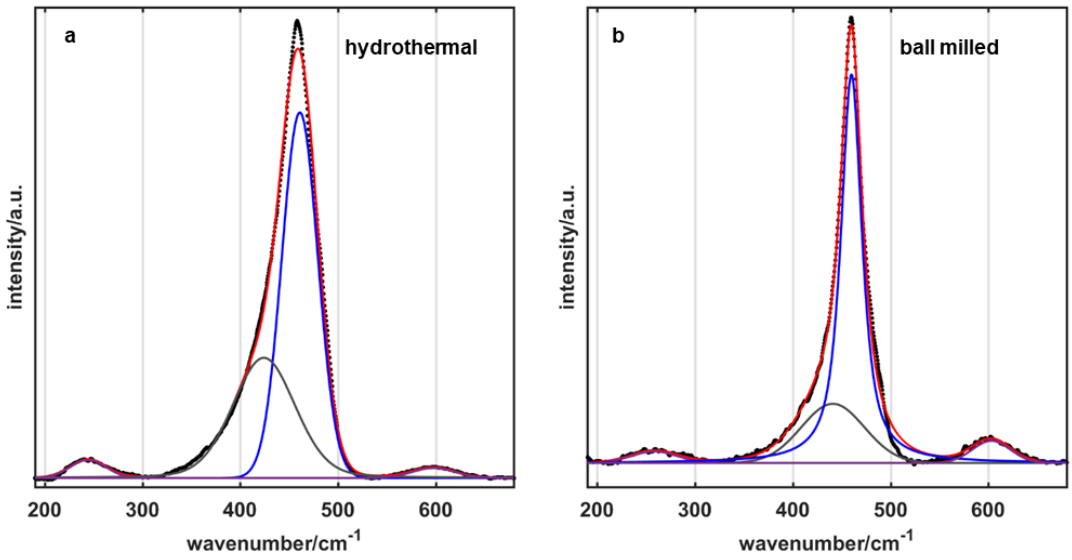

Figure S 4.6. Best Lorentz fit (red line) of the Raman spectra of CeO_2 nanocrystals synthesized (a) hydrothermally and (b) by ball milling. The full width at half maximum (fwhm) of the main band (43.3 cm^{-1}) of the hydrothermally prepared CeO_2 nanocrystals is significantly larger than the band (25.7 cm^{-1}) of the ball-milled nanocrystals. This indicates a higher disorder of hydrothermally prepared nanocrystals and is most probably explained by the anisotropic crystal morphology.

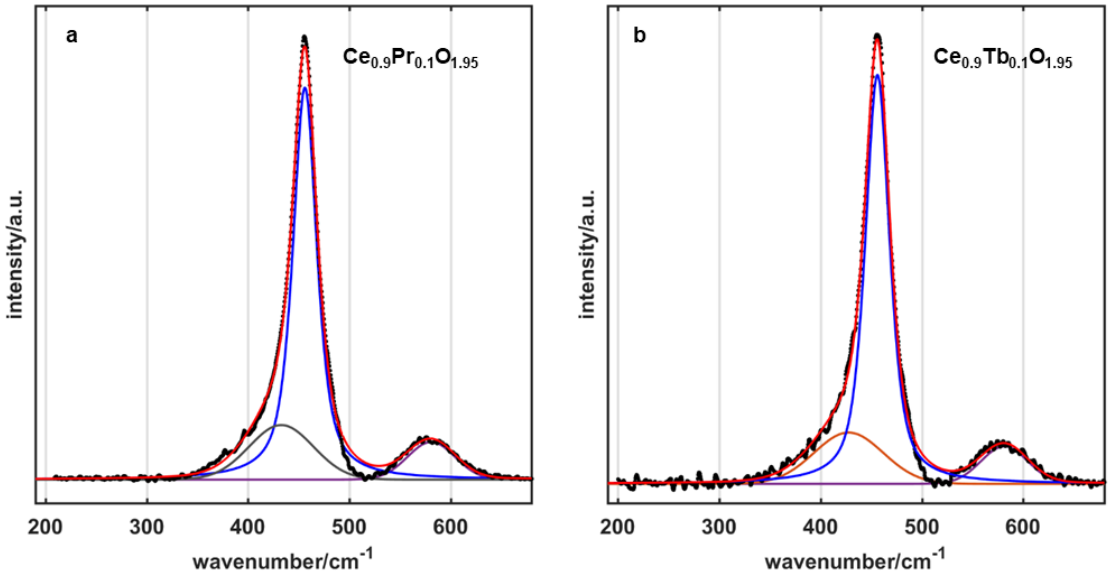

Figure S 4.7. Best Lorentz fit (red line) of the Raman spectra of the (a) Pr- and (b) Tb-doped CeO_2 nanocrystals.

Table S 4.3. Assignment of Raman spectra.

	Band 1 (cm^{-1})	Band 2 (cm^{-1})	Band 3(cm^{-1})	Band 4(cm^{-1})
CeO_2 hydrothermally prepared	244.2	424.2	461.0	598.0
CeO_2 ball milled	258.3	440.9	460.0	603.0
$Ce_{0.9}Pr_{0.1}O_{1.95}$	-	432.8	456.1	580.9
$Ce_{0.9}Tb_{0.1}O_{1.95}$	-	427.7	456.1	581.4
Assignments[4–7]	TA/TO	F_{2g}	F_{2g}	D_1

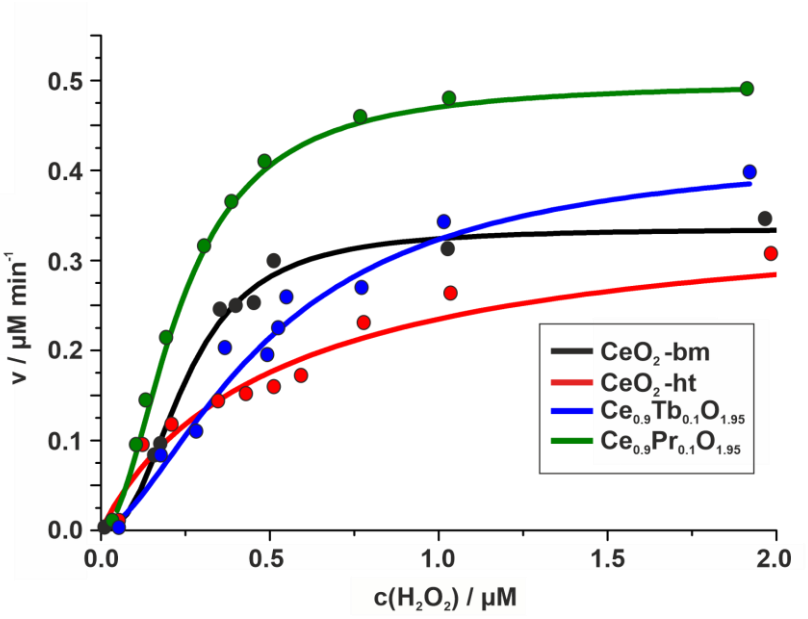

Figure S 4.8. Hill-Fit of undoped and Pr- and Tb-doped CeO_2 nanocrystals.

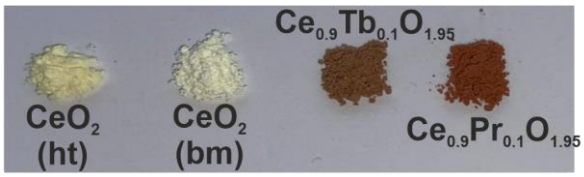

Figure S 4.9. Digital photographs of CeO_2 (bm & ht), $Ce_{0.9}Tb_{0.1}O_{1.95}$ and $Ce_{0.9}Pr_{0.1}O_{1.95}$ powders.

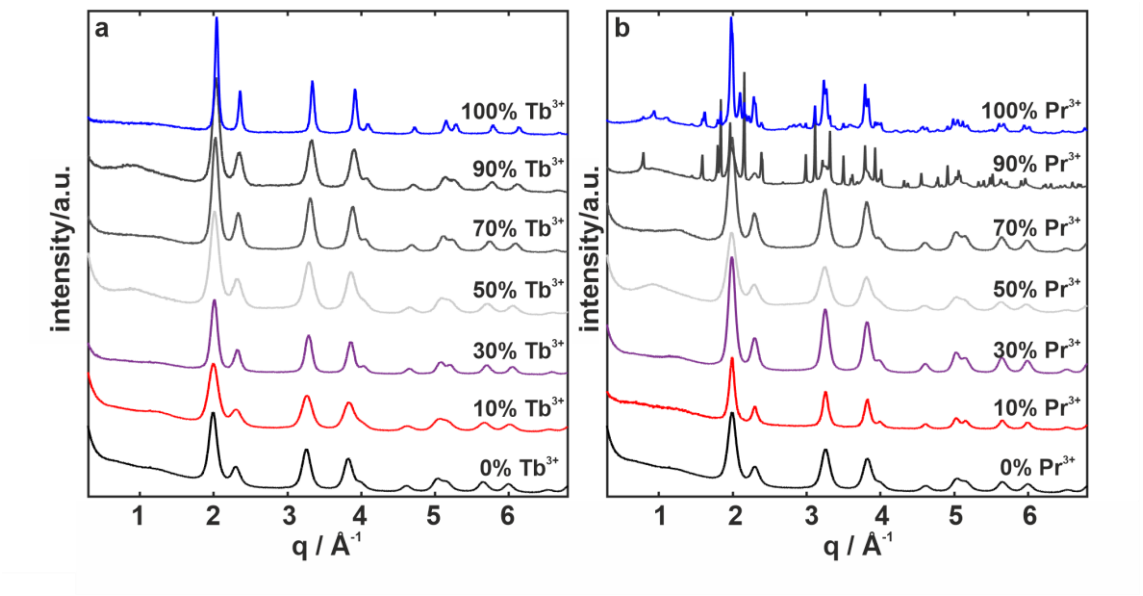

Figure S 4.10. X-ray powder diffractograms showing the miscibility of CeO_2 with a) (Tb^{3+}) and b) (Pr^{3+}).

Bacterial biofilm formation.

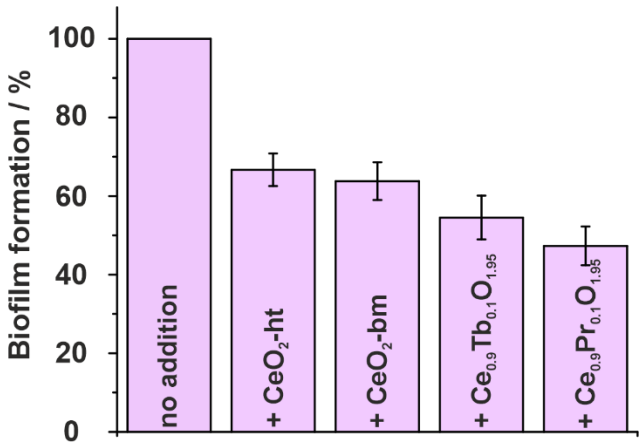

Figure S 4.11. Bacterial biofilm formation with no addition, CeO_2-ht, CeO_2-bm, $Ce_{0.9}Tb_{0.1}O_{1.95}$ and $Ce_{0.9}Pr_{0.1}O_{1.95}$ nanoparticles. Crystal violet staining assay of *Pseudomonas aeruginosa* grown in lysogeny broth.

Biofilm inhibition was verified using Gram-negative bacteria *Pseudomonas aeruginosa*. A crystal violet staining assay was performed to determine the amount of adherent cells. The results in Figure S4.11 show that the undoped particles achieve an inhibition of 35%. The Tb- and Pr- doped CeO_2 particles reduce growth by even 50%.

4.7.1. References

1. R. Valiokas, L. Malysheva, A. Onipko, H. H. Lee, Ž. Ružele, S. Svedhem, S. C. T. Svensson, U. Gelius, B. Liedberg, On the quality and structural characteristics of oligo(ethylene glycol) assemblies on gold: An experimental and theoretical study. *J. Electron Spectros. Relat. Phenomena*. 2009. **172**, 9–20.
2. Y. Sohn, Structural and spectroscopic characteristics of terbium hydroxide/oxide nanorods and plates. *Ceram. Int.* 2014. **40**, 13803–13811.
3. M. M. Natile, A. Glisenti, Nanostructured CeO 2 Powders by XPS . *Surf. Sci. Spectra*. 2006. **13**, 17–30.
4. M. Krawczyk, M. Pisarek, W. Lisowski, A. Jablonski, Surface studies of praseodymium by electron spectroscopies. *Appl. Surf. Sci.* 2016. **388**, 691–695.
5. C. Li, Y. Sakata, T. Arai, K. Domen, K. Maruya, T. Onishi, Carbon monoxide and carbon dioxide adsorption on cerium oxide studied by Fourier-transform infrared spectroscopy. Part 1.—Formation of carbonate species on dehydroxylated CeO2, at room temperature. *J. Chem. Soc. Faraday Trans. 1 Phys. Chem. Condens. Phases*. 1989. **85**, 929.
6. S. Chen, T. Cao, Y. Gao, D. Li, F. Xiong, W. Huang, Probing Surface Structures of CeO_2, TiO_2, and Cu_2O Nanocrystals with CO and CO_2 Chemisorption. *J. Phys. Chem. C*. 2016. **120**, 21472–21485.
7. G. N. Vayssilov, M. Mihaylov, P. St. Petkov, K. I. Hadjiivanov, K. M. Neyman, Reassignment of the Vibrational Spectra of Carbonates, Formates, and Related Surface Species on Ceria: A Combined Density Functional and Infrared Spectroscopy Investigation. *J. Phys. Chem. C*. 2011. **115**, 23435–23454.
8. W. H. Weber, K. C. Hass, J. R. McBride, Raman study of CeO 2 : Second-order scattering, lattice dynamics, and particle-size effects. *Phys. Rev. B*. 1993. **48**, 178–185.
9. C. Schilling, A. Hofmann, C. Hess, M. Veron, Raman Spectra of Polycrystalline CeO2: A Density Functional Theory Study. *J. Phys. Chem. C*. 2017, **121**, 20834-20849.
10. O. Kraynis, I. Lubomirsky, T. Livneh, Resonant Raman Scattering in Undoped and Lanthanide-Doped CeO_2. *J. Phys. Chem. C*. 2019. **123**, 24111–24117.
11. M. Gupta, A. Kumar, A. Sagdeo, P. R. Sagdeo, Doping-Induced Combined Fano and Phonon Confinement Effect in La-Doped CeO_2 : Raman Spectroscopy Analysis. *J. Phys. Chem. C*. 2021. **125**, 2648–2658.

5 Transparent Polycarbonate Coated with CeO_2 Nanozymes Repel *Pseudomonas aeruginosa* PA14 Biofilms

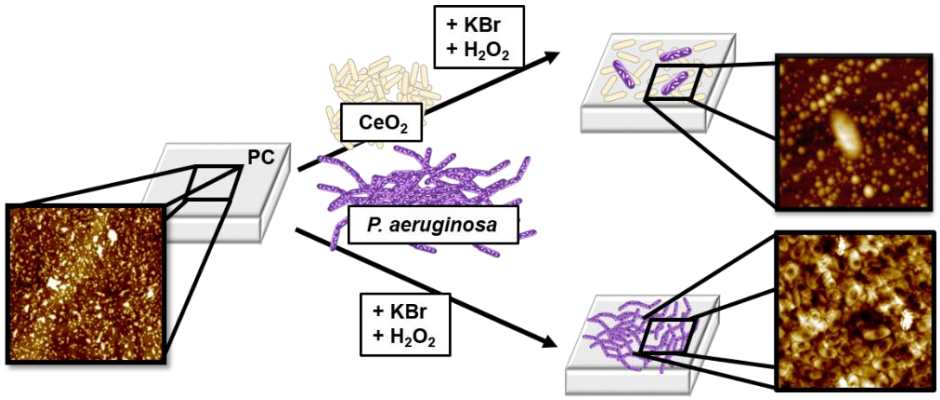

This chapter 5 was published in Nanoscale, 2022, 14, 86-98.
(DOI: doi.org/10.1039/D1NR03320D) and was used with minor variations.

Author Contributions:

Olga Jegel:	Concept development, establishing the production of composite, plasma treatment, contact angle measurement, SEM images, TLCMS measurement, manuscript preparation, figure preparation.
XXX:	Nanoparticle synthesis, haloperoxidase assay, TEM, BET surface area and ζ-potential measurement, manuscript preparation.
XXX:	biologic evaluation.
XXX:	HRTEM measurement.
XXX:	AFM measurement.
XXX:	ICPMS measurement.
XXX:	ICPMS measurement.
XXX:	cell viability assay.
XXX:	TLCMS measurement
XXX:	Manuscript correction.
XXX:	Manuscript correction and scientific supervision.

5.1. Summary

The last chapter of this thesis focused on an application of cerium oxide nanoparticles. The idea was utilizing that CeO_2 can mimic the enzyme vanadium haloperoxidase, which is able to oxidatively brominate molecules in the presence of H_2O_2 and Br^-. Since bacteria use signal molecules, also called autoinducers (AI), to communicate with each other (quorum sensing) and thus proliferate, the idea was to interrupt the communication between the bacteria by brominating the signal molecule using the catalyst and thus making it unrecognizable by other bacteria (quorum quenching).

The aim was to create a composite of polycarbonate plates and CeO_2 nanoparticles by dip-coating. The problem of nanoparticle coating is the nanoparticle dispersion must be very homogenized and should not contain agglomerates. This would provide an uneven coating and a rough surface. Therefore, a synthesis of cerium oxide nanoparticles was applied in which the particles were functionalized with the ligand nitrilotriacetic acid (NTA) and were well dispersible in aqueous solutions.

Since polycarbonate has a strongly hydrophobic surface and therefore does not wet well, the surface had to be modified. For this purpose, it was treated with oxygen plasma, whereby the formation of OH and COOH groups significantly rendered the surface more hydrophilic. The result was confirmed with the aid of contact angle measurements. After the surface of polycarbonate was modified and were well-dispersible nanoparticles were synthesized, the polycarbonate plates were wetted by dip coating and then dried in the oven.

Finally, bioassays were performed on the final composite. For this step, the plates were incubated with the Gram-negative bacterium *Pseudomonas Aeruginosa*, H_2O_2 and Br^-. After three days, the mass from the biofilm of the bacteria was quantified by a crystal violet staining assay. This demonstrated that the coated plates reduced biofilm formation by 75% compared to pristine polycarbonate. In addition, live and dead cells of the bacteria were stained with the dyes SYTO9 and propidium iodide (PI). This proved that CeO_2 has no biocidal effect and that the mechanism of biofilm inhibition is indeed due to the mechanism of quorum quenching.

Atomic force microscopy images of CeO_2 coated and pristine polycarbonate and of the bacterial films on coated and pristine polycarbonate were also obtained.

A CeO_2-polycarbonate composite was successfully fabricated and revealed the reduction of the biofilm formation by 75%. It was also shown that cerium oxide has no biocidal activity.

5.2. Introduction

Polycarbonate (PC) is an engineering plastic with a wide range of applications that is used as a substitute for glass [1] for large-area coverings and safety glazing, e.g. in the automotive industry, in greenhouses or for outdoor covers, as it is much softer and easily moldable to meet modern design and production requirements. However, low hardness, scratch resistance and low resistance to photo- or biocorrosion limit the use of PC for many industrial applications. It is therefore of interest to modify or improve the surface of the polymer without changing its bulk properties. PC is very transparent to visible light and has better light transmission properties than many types of silica glass. However, PC unfortunately has a low glass transition temperature of ~150 °C and gradually softens above this temperature and begins to flow above ~300 °C. To allow PC to be used in applications exposed to weathering or UV radiation, a special surface treatment is required. The surface properties of plastic surfaces can be specifically modified by coating. There are a variety of strategies to functionalize polymer surfaces for biomedical applications by plasma treatment, superhydrophobic surfaces, quaternary ammonium compounds, chitosan-containing surfaces or embedded nanoparticles (NPs).[2-7]

Coating polymer surfaces with metal oxide nanoparticles allows potentially interesting commercial applications such as self-cleaning or antibacterial properties.[8] Polymer surfaces coated with TiO_2 nanoparticles are more scratch resistant and have antibacterial properties due to the photocatalytic properties of TiO_2, but a recent classification of nano-TiO_2 as a "suspected carcinogen" by the EU may lead to restrictions or even a ban on their chemical use in consumer products.[9] Coating with ZnO/TiO_2 NPs may lead to self-cleaning, coating with nano-Ag or carbon nanotubes to antibacterial properties.[10] A common problem with silver nanoparticles or antibiotics is the decrease of the antibacterial activity due to leaching of the active compound with time, leading to materials with a limited life span and metal (Cu, Ag) nanoparticles that are harmful to the environment.[11] Tailored surfaces to which bacteria and cells cannot adhere represent an alternative approach to combat bioadhesion.[12] Surfaces coated with poly(ethylene oxide) or polymers with zwitterionic groups are known to suppress nonspecific protein adsorption and bacterial adhesion.[13,14] Superhydrophobic antibacterial coatings with polycarbonate have been proposed for catheters to prevent infections.[15]

Antibiotics are the most important tools in the fight against bacteria. However, bacteria are adaptable and can build up resistance to antibiotics.[16] For this reason, research is constantly

being conducted to find other ways of combating. One of these antibiotic-resistant bacteria is the gram-negative bacterium *Pseudomonas aeruginosa (P. Aeruginasa)*. It is among the most common causes of respiratory pneumonia, wound infections and urinary tract infections worldwide.[17]

Our approach to manufacturing biofilm-inhibiting surfaces of such bactaria is non-toxic and inspired by nature: Using oxidizing halogenating enzymes (haloperoxidases, HPOs), seaweeds catalyze the oxidation of halides (Cl^- and Br^-) with hydrogen peroxide (H_2O_2) to form hypohalous acids (HOCl and HOBr).[18,19,20] In the presence of ubiquitous Br^- ions and H_2O_2, generated in sunlight, CeO_2 is – by virtue of its catalytic activity – a functional substitute for haloperoxidases, which can also brominate AHL signal molecules so that communication between bacteria is disrupted (*quorum quenching*) and biofilm formation is inhibited in a non-biocidal way.[21] Metal complexes,[22-24] V_2O_5 [25] and CuO[26] or ceria[21,27] nanoparticles have been reported act as "nanozymes" (inorganic nanoparticle-based artificial enzymes) by mimicking HPO activity.[28,29] Ceria nanoparticles are readily and inexpensively available, non-toxic,[30] highly insoluble (pK_L = 60),[31] stable over a wide pH range[32] and therefore environmentally safe. Thus, they are ideally suited for real-world applications.[22,33-35]

Important problems in the coating of polymer surfaces are the low temperature stability and the low surface energy of the polymer. This leads to poor surface wetting, which results in weak adhesion.[36] Polymer surfaces can be coated with metal oxides in various ways to achieve potentially interesting commercial applications such as self-cleaning or antibacterial properties.[37] Different low-temperature techniques such as pulsed laser deposition (PLD),[38] magnetron sputtering,[39] spray pyrolysis,[40] and metal organic chemical vapor deposition (MOCVD) [41] are available to prepare surface-active CeO_2 films at low temperature. However, most physical vapor deposition processes have problems in depositing large area films, require complex optimization of deposition conditions, and the substrates are silicon or transition metals. Wet chemical deposition is suitable for producing thin layers on large surfaces, but drying metal oxide films on heat-sensitive polymer substrates is problematic[42] leads to thin films with low surface area and low catalytic activity. A quick and simple method to increase surface energy and adhesion is plasma treatment with oxygen (O_2) or argon (Ar).[33,41] As a result, oxygen-containing groups such as hydroxyl, carbonyl and carboxyl groups are incorporated on the surface, increasing the polarity.[42]

Last but not least, CeO_2 nanoparticles for surface coatings must be available in sufficiently large quantities and be well dispersible to achieve homogeneous coatings, as agglomerates otherwise impair the optical appearance and deteriorate the surface roughness of the material. Since nanoparticles are only reactive when exposed at the surface, coating approaches are much more material efficient and effective than embedding particles in a bulk polymer.[21] We present (i) a large scale synthesis of CeO_2 nanorods along with (ii) a polycarbonate coating approach that allows easily scalable process parameters and thus potential mass production. (iii) We demonstrate by scanning electron microscopy and scanning probe techniques the bacterial repellancy of the film and (iv) show the quorum quenching mechanism through the production of the virulence factor pyocyanin in response to the haloperoxidase-like activity of the CeO_2 coating. The proven non-toxicity of the coating makes polycarbonate surfaces promising for resisting biofilm formation in daily use where H_2O_2 is present in humid environments such as greenhouses or plastic containers for rainwater (H_2O_2 production in ground water,[43] the atmosphere,[44] or in natural water exposed to sunlight).[45]

5.3. Results and Discussion

Particle Preparation and Analysis. A freshly prepared cerium(III) hydroxide dispersion was used for the synthesis of ceria nanoparticles in aqueous media with hydrogen peroxide as oxidant and nitrilotriacetic acid (NTA) as capping agent. The capping agent ensured the formation of a stable suspension without inhibiting the haloperoxidase activity of the CeO_2 nanoparticles by forming surface complexes. In addition, the capping agent can be used to produce a stable suspension that is used for polycarbonate coating. The reaction can be easily scaled up to the 100 g scale in batch operation for coating large surface areas.

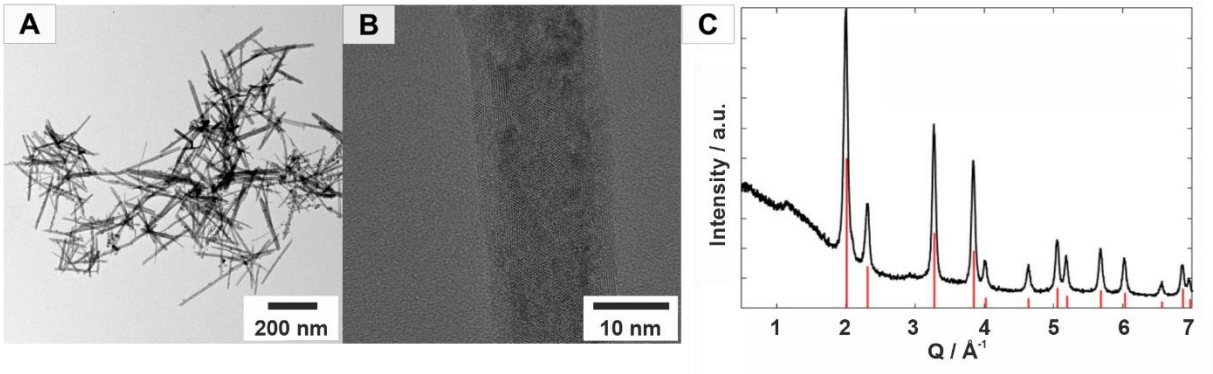

Figure 5.1. (A,B) TEM image of CeO_2 nanorods and (C) X-ray powder diffraction pattern of a CeO_2 sample. Red ticks indicate the calculated reflection positions for CeO_2 based on structural data from the JCPDS data bank (JCPDS# 00-034-0394).

Figure 5.1A displays a TEM micrograph of a sample obtained after centrifugation from an aqueous nanoparticle dispersion. The reaction yielded nanorods with a length of 100-200 nm and a width of 10-15 nm, suitable for a transparent coating of surfaces. The X-ray powder diffraction pattern confirmed the formation of single phase CeO_2 (Figure 5.1C) in the bulk sample. The nanoparticles were carefully washed three times by centrifugation at 9000 rpm for 30 min. We avoided irreversible agglomeration by preventing complete solvent evaporation. NTA is well suited as a ligand for CeO_2 because the carboxylate groups are hard donors for ionic bonding to Cer^{4+} ions. NTA is thought to form a complex with cerium surface atoms in which the three carboxylate groups are bound by ionic interactions and the N atom of NTA ligand by dative interactions.[46] Light scattering experiments revealed an average hydrodynamic radius of 115 ± 79 nm for CeO_2 nanoparticles with NTA surface ligands.

Haloperoxidase Activity. The haloperoxidase-like activity of CeO_2 nanorods was demonstrated with a phenol red bromination assay. In this assay, a phenol sulfonphtalein indicator (phenol red, PR) is brominated in aqueous solution in the presence of Br^- and H_2O_2

to bromophenol blue (3‘,3‘‘,5‘,5‘‘-tetrabromophenolsulfonphtalein, Br_4PR). The reaction can be monitored spectrophotometrically, because the educt and product have different distinct absorption maxima at $\lambda_{max,PR}$=430 nm, and λ_{max,Br_4PR}=590 nm. Michaelis-Menten enzyme kinetics were assumed because haloperoxidase-like activity was dependent on H_2O_2 concentration. The kinetics were measured for different concentrations of H_2O_2 and fitted with a Hill equation (Equation 5.1) (Figure 5.2).[47]

$$\mathbf{v} = \frac{\mathbf{v_{max}} \cdot [S]_o}{\mathbf{K_m} \cdot [S]_o} \tag{5.1}$$

The Michaelis constant K_m is a measure of the affinity of the enzyme, in this case CeO_2, for the H_2O_2 substrate with the concentration $[S]_o$. The value K_m has a reciprocal relationship with the affinity, i.e., the higher the constant, the weaker the binding strength between enzyme and substrate. For CeO_2, the constant is 0.85 mM and which indicated a high affinity for H_2O_2. The maximum rate of the reaction is described by the v_{max} value, which is 0.021 µM min^{-1} for the CeO_2 nanorods.

The bromination rate depends on (i) the surface charge, (ii) BET surface area, and (iii) the presence or nature of surface ligands. The CeO_2 particles have a ζ-potential of -22.5 ± 0.9 mV and a BET surface of 81.606 m^2/g. They were functionalized with nitrilotriacetic acid (NTA) to achieve better dispersibility in aqueous solution. This is an important prerequisite for achieving a homogeneous surface coating.

$$\mathbf{TOF} = \frac{\mathbf{v_{max}}}{\mathbf{[Cat]_0}} \xrightarrow{\mathbf{[Cat]_0 \rightarrow S_{BET} \cdot \beta(Cat)}} \mathbf{ROR} = \frac{\mathbf{v_{max}}}{\mathbf{S_{BET} \cdot \beta(Cat)}} \tag{5.2}$$

CeO_2 nanoparticles catalyze the oxidative bromination of N-(3-oxo-acyl)homoserine lactones (AHLs) at the activated C2 atom forming mono- and dibromo-3-oxo-dodecanoylhomoserine lactones. The bromination is complete after approx. 60 min. The brominated AHLs are hydrolyzed in a subsequent step, the hydrolysis being complete after approx. 5 h, as demonstrated by inductively couple plasma mass spectrometry (ICP-MS). *Pseudomonas Aeroginosa* bacteria use 3-oxo-dodecanoylhomoserine lactone to communicate with each other and to determine their cell count (quorum sensing, QS), [20] where biofilm formation is under control of QS through the production of the virulence factor pyocyanin in response to the haloperoxidase-like activity (Figure S5.6, *vide infra* and Supporting Information).

The rate of reaction (ROR) was determined to relate the conversion rate to the available surface area (Equation 5.2).[48] The maximum rate v_{max} = 0.021 µM min^{-1} and the specific surface gave a reaction of ROR(CeO_2) = 0.0087 µmol m^{-2} min^{-1}.

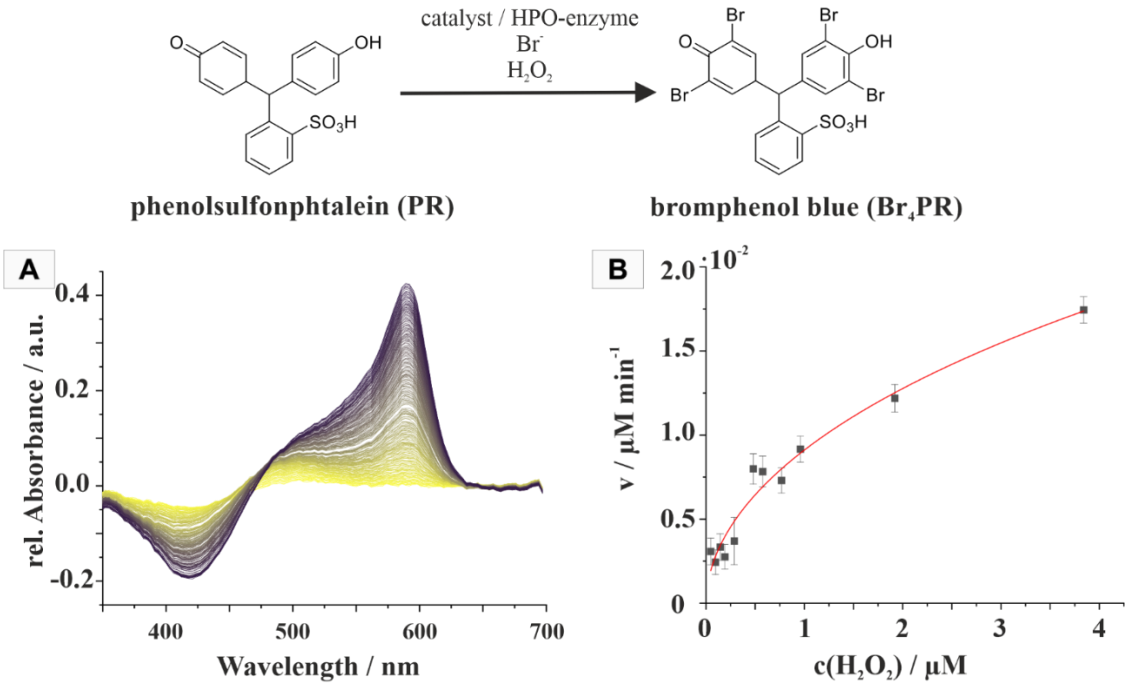

Figure 5.2. Haloperoxidase-like activity of CeO_2 nanoparticles determined with a phenol red bromination assay. (A) Time-dependent UV-vis spectra indicate the change of the oxidative bromination from phenol red (PR) to bromophenol blue (Br_4PR). (B) shows the Michaelis-Menten kinetics for the substrate H_2O_2 using the CeO_2 enzyme mimic.

Coating Polycarbonate with Ceria Nanoparticles. Polycarbonate has a hydrophobic surface, which leads to a small surface energy. The surface was treated in an oxygen plasma. Figure 5.3 shows the contact angle of untreated and oxygen plasma-treated polycarbonate. The contact angle of a pristine polycarbonate surface was 86.75° and decreased to 26.88° after a 20-minute oxygen plasma treatment, i.e., the surface became significantly more hydrophilic. Hofrichter et al.[49] showed by XPS spectroscopy that plasma treatment increases the oxygen content and decreases the carbon content by generating oxygen-containing groups such as –(C-O)-, -(C=O)- and –(O-C=O)- on the polycarbonate surface. Binding of ceria nanoparticles to polycarbonate occurs by ester condensation of their surface hydroxyl groups with carboxylate surface groups or by hydrogen bonding between polar groups on the polymer surface and ceria particles.[50,51]

The smaller contact angle of 26.88° shows a significantly higher hydrophilic surface, which facilitates the contact of the suspension with the surface of the polycarbonate and thus enables the coating with ceria nanoparticles. For the dip coating process, oxygen plasma treated polycarbonate slides were treated in aqueous ceria suspensions and slowly pulled out of the dispersion to obtain a homogeneous coating. After dip coating, the plates were annealed at 110 °C for 16 hours. Excess CeO_2 was carefully washed off before further

testing. Due to the hydrophilicity of the ceria on the surface, the contact angle after the coating process showed a 12.74° lower value than the untreated polycarbonate sample, i.e., the coating with CeO_2 nanorods increased the hydrophilicity of the polycarbonate surface. The ceria content at the surface was determined by ICPMS (1.6 µg/cm²). Leaching tests showed no trace of ceria in the water supernatant after 7 days. Figure 5.3 demonstrate an image of untreated, plasma-treated and CeO_2-coated PC where there is no visual difference. Additionally, this assumption is proven by a spectroscopic investigation using UV/Vis spectroscopy (Figure S5.9). The polycarbonate absorbs light in the UV range for all three samples.

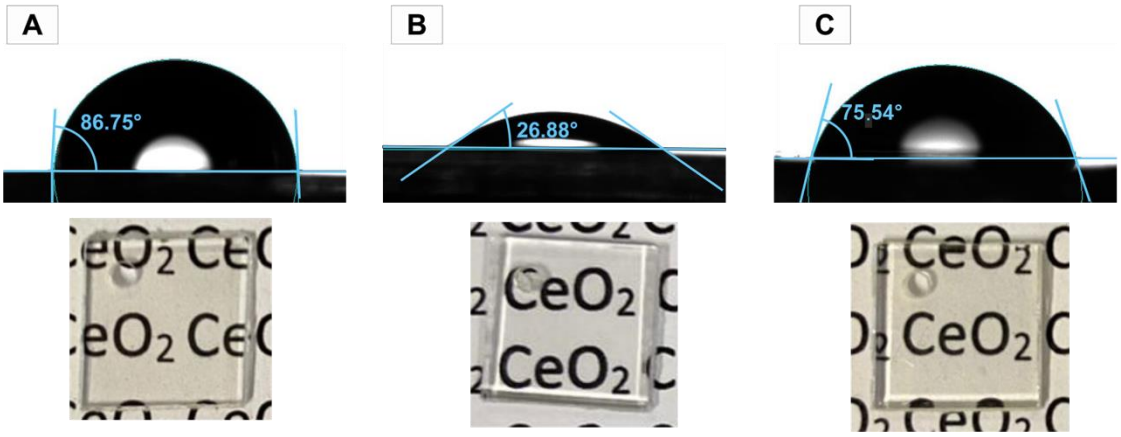

Figure 5.3. Contact angle of a water drop on (A) untreated (B) O_2 plasma-treated and (C) CeO_2 coated polycarbonate with an optical microscopy image of the polycarbonate plates (1x1 cm).

The surface morphology of the untreated and CeO_2 coated polycarbonate was characterized after 10 days of storage at 7°C by atomic force microscopy (Park System NX10, Figure 5.4). When comparing the height images, the untreated polycarbonate showed a smooth topography with low surface roughness of Rq = 1.5 nm, the polycarbonate surface coated with cerium oxide nanorods exhibited a slightly higher roughness of Rq = 5.8 nm.

The size of the particles can be inferred from the individual profiles.[52] With a typical length of 80-200 nm (Figure S5.4, Supporting Information) and an apparent typical thickness of 27-47 nm (see Figure S5.3 red arrows), the CeO_2 nanorods appear to have a lower aspect ratio compared to the TEM images (Figure 5.1). However, this difference originating from tip convolution effects is bypassed when comparing the measured z-heights. Typical thicknesses of 6.2-12.7 nm (see green arrows, Figure S5.3) well fit with the observed aspect ratio. The CeO_2 nanoparticles show a distinct contrast to the polycarbonate substrate in phase (Figure 5.4 C and D). The phase image of the CeO_2 coated polycarbonate plates shows a

homogeneous distribution of the nanorods (Figure 5.4B-D) compared to the uncoated polycarbonate slides.

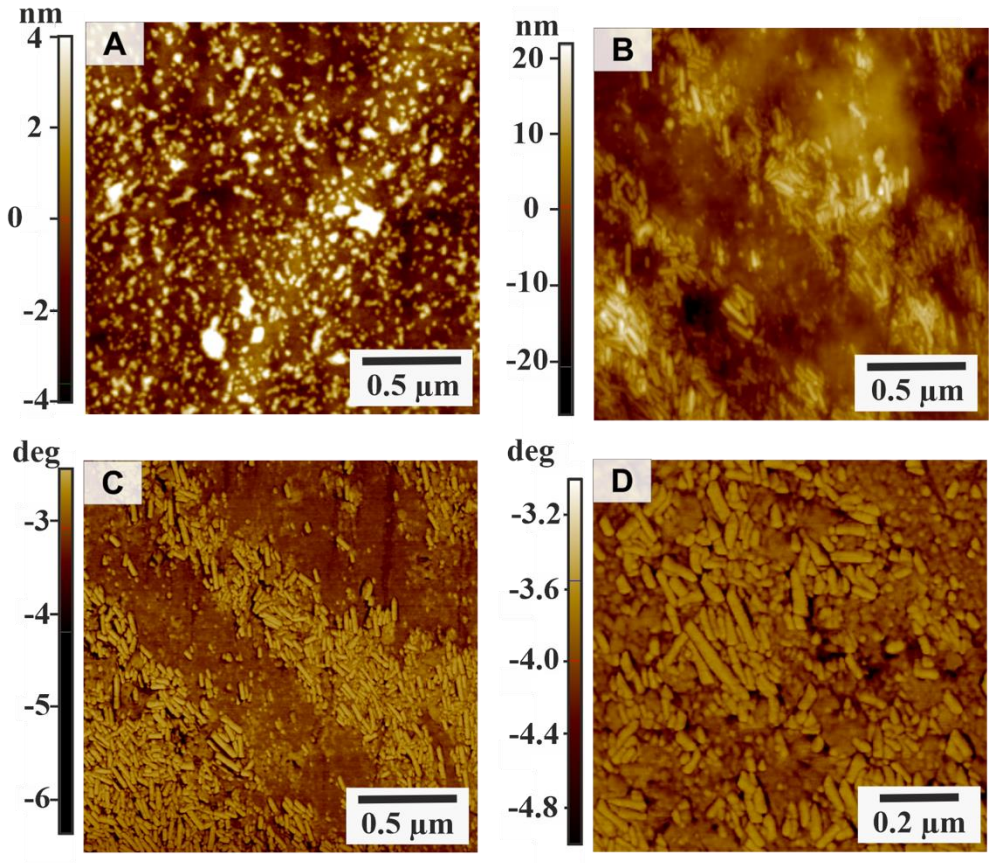

Figure 5.4. Surface morphology analyzed by AFM. Height images of (A) untreated polycarbonate slides, (B) polycarbonate slides coated with CeO_2 nanorods and (C + D) phase images of CeO_2-coated polycarbonate slides.

The surface was also examined by scanning electron microscopy (SEM) (Figure S5.1). EDX mapping was conducted to analyze the elemental distribution and verify the presence of CeO_2. The surface was sputtered with a 1 nm gold layer to achieve a better contrast. As reported by literature, Ce has a characteristic peak in the X-ray emission spectrum of L_α :4.839 keV, which is reflected by the signal at 4.9 eV in the recorded EDX spectrum.[53] The low signal can be explained by the low concentration of CeO_2 on the surface. Also visible is the characteristic M_α signal of gold at 2.12 keV, which is attributed to the sputtered gold layer on the surface. Moreover, the signals of oxygen (O) at 0.53 keV (K_α) and carbon (C) at 0.28 keV (K_α) can be recognized.

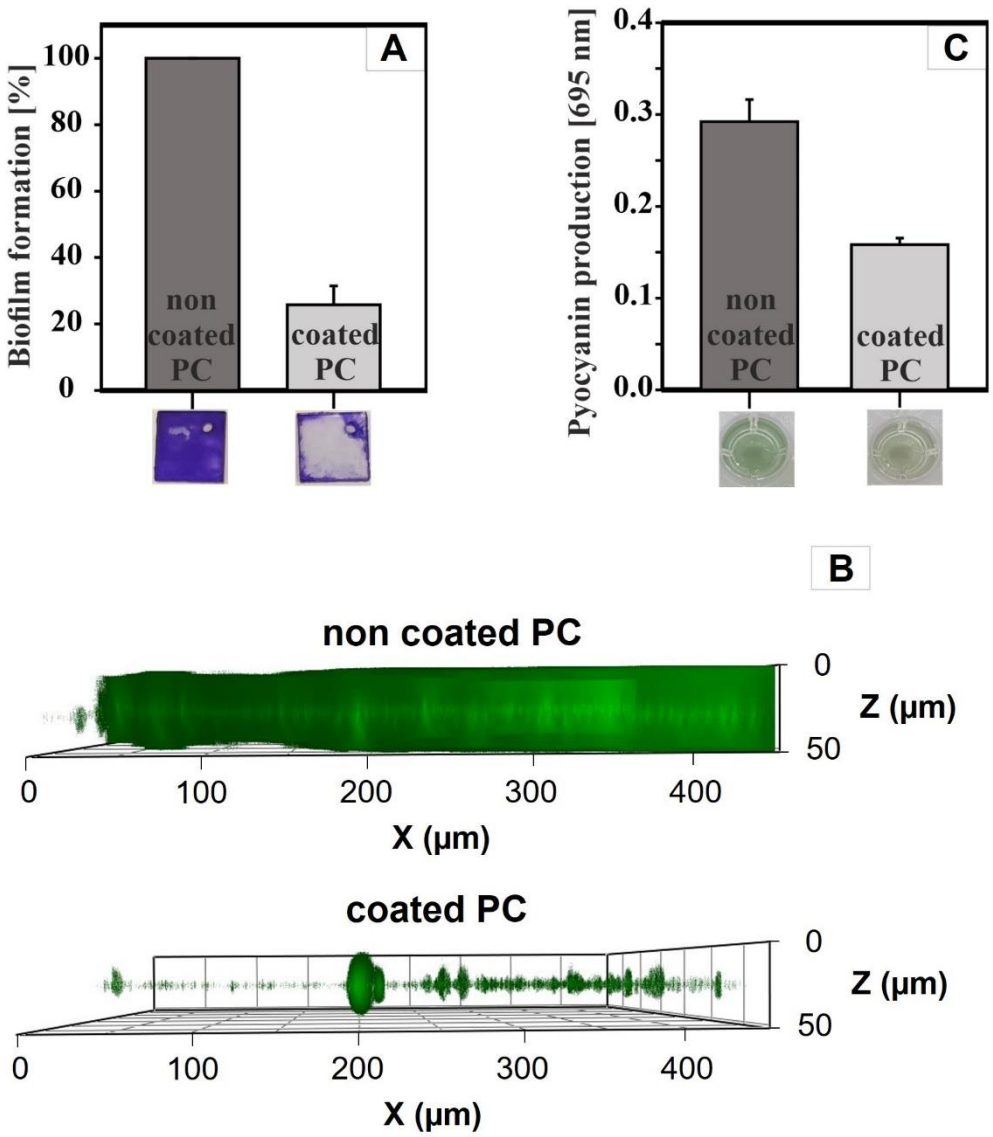

Figure 5.5. (A) Bacterial biofilm formation on non-coated and CeO_2-coated polycarbonate plates. Crystal violet staining assay of *P. aeruginosa* grown in lysogeny broth. The stained plates are shown in the lower part of the plots (B) Confocal laser scanning microscopy of *P. aeruginosa* biofilm on coated and non-coated surfaces. The non-coated plate served as positive control. The planktonic cells were removed, and the remaining bacteria attached to the surfaces were stained with SYTO 9 and propidium iodide for 30 minutes at 30 °C. The effect of the CeO_2 coated plates on the cell attachment was then visualized. (C) Effect of CeO_2-coated polycarbonate surfaces versus non coated plates on pyocyanin production in *P. aeruginosa*. Error bars represent the standard deviation of three independent experiments.

CeO_2-Coated Polycarbonate Inhibits Biofilm Formation. The coated plates were tested regarding their potential to inhibit the biofilm formation of *P. aeruginosa*, a prominent Gram-negative bacterium which is responsible for up to 10% of all healthcare-associated infections (HAI) in Germany as well as spoiling drinking water through its occurrence in drink water pipes.[54] Due to its strong biofilm-forming behavior simple surface cleaning with disinfectants is often not sufficient and gives rise to strains resistant to antibiotics.

To understand the effect of CeO_2 nanoparticles on biofilm formation of *P. aeruginosa* a crystal violet staining assay was performed to determine the amount of adherent cells (Figure 5.5A). After culturing the bacteria on polycarbonate for 72 h, the attached cells were stained with crystal violet solution. Biofilm formation was reduced by ~75% on the coated PC surfaces. The thickness of the biofilms on the PC surfaces was quantified by confocal laser scanning microscopy (Figure 5.5B). For that purpose, the bacterial biofilms were cultivated for 72 h at 30° C on different PC samples placed in 24-well plates. The attached cells were then stained with SYTO9 and propidium iodide, two specific dyes staining the total cell count in the biofilm. The CeO_2-coated plates showed a significant reduction in biofilm thickness to ~20 µm compared to uncoated PC surfaces, where the biofilm thickness was more than 50 µm. In addition, the biofilm on the coated plates grows in microcolonies and is not evenly distributed over the entire surface as it is on the uncoated plates.

We analyzed whether the biofilm inhibiting effect of CeO_2 is mediated by blocking bacterial quorum sensing, a process designated as quorum quenching. In P. aeruginosa, biosynthesis of pyocyanin, another virulence factor besides biofilm formation, is under control of quorum sensing. Therefore, we analyzed pyocyanin production on CeO_2 coated and non-coated PC surfaces (Figure 5.5C). For that purpose, the bacteria were grown for 72 h at 30°C on uncoated and coated polycarbonate plates. The plates were then removed, and the remaining culture fluid was analyzed for pyocyanin. The CeO_2-coated polycarbonate plates reduced the pyocyanin formation of the biofilm grown on the surface by 54% compared to the uncoated plate. This indicates that quorum sensing-dependent pyocyanin formation is reduced by CeO_2 nanoparticles and lends support to the idea that CeO2 also inhibit bacterial biofilm formation by quorum quenching. The remaining pyocyanin synthesis might be due to pelagic bacteria in the well, which are not directly exposed to the CeO_2 nanoparticles.

Assay for Bacterial Viability. To understand the process of biofilm colonization, it is important to analyze whether biofilm formation is reduced by killing the bacteria or by suppressing group behavior.

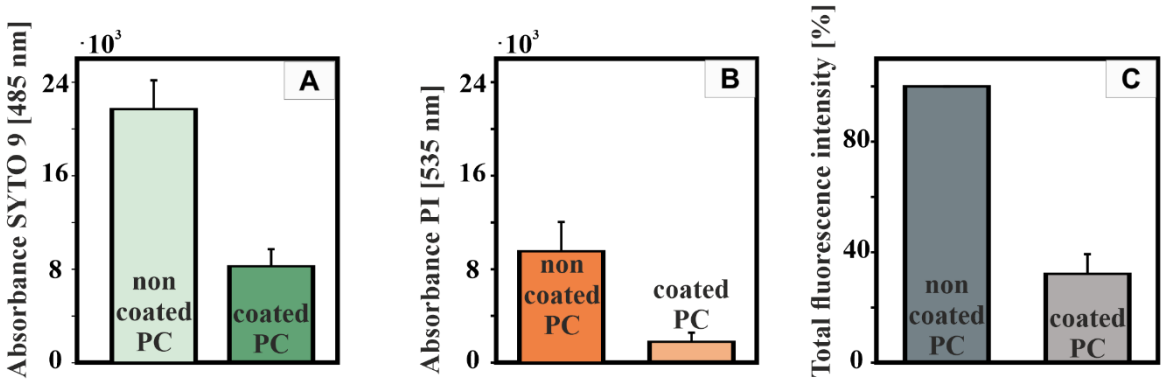

Figure 5.6. Quantification of *P. aeruginosa* biofilm formation on non-coated and CeO_2-coated polycarbonate plates. Blank plates served as positive control. The planktonic cells were removed, and the remaining bacteria attached to the plates were stained with SYTO 9 (A) and propidium iodide (PI) (B). (C) Finally, the effect of the incorporated CeO_2 nanorods on bacterial biofilm formation was quantified by measuring the absorption at 485 nm for SYTO9 and 535 nm for propidium iodide, respectively. Error bars represent the standard deviation of three independent experiments.

Live/dead fluorescence assays were performed using SYTO 9 and propidium iodide (PI) dye. SYTO 9 stains only live cells, while PI penetrates only dead or damaged cells.[55] In this way, the number of the living and dead cells present in the biofilm can be analyzed. Figure 5.6 shows that the live/dead ratio does not change significantly for the CeO_2/polycarbonate plates and the uncoated reference, while the total amount of bacteria decreases.[55] In addition, the biofim-inhibiting activity of the CeO_2 nanorods was investigated using atomic force microscopy (AFM) and scanning electron microscopy (SEM) (Figure S5.10) for a *P. aeruginosa* cell culture.

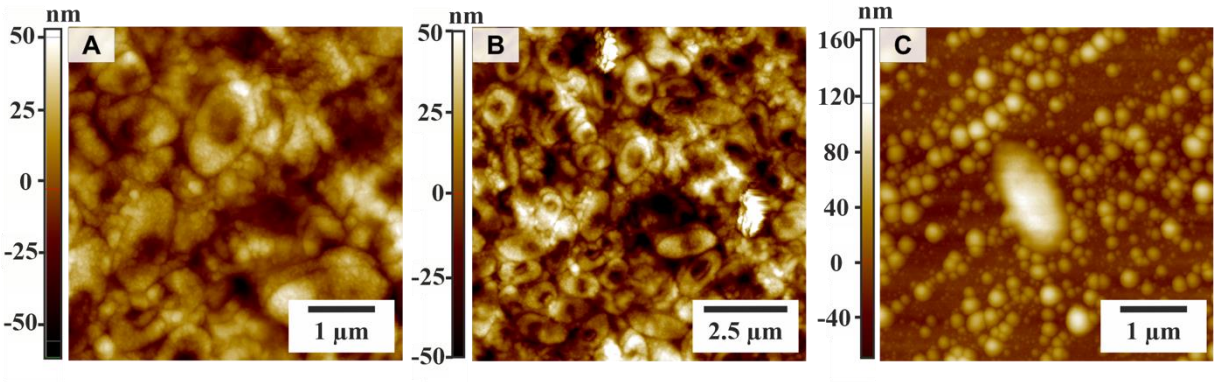

Figure 5.7. Atomic force microscope (AFM) images of non-coated (A+B) and CeO_2-coated polycarbonate (C) with a P. aeruginosa culture.

Bacteria were cultured on CeO_2-coated and uncoated polycarbonate substrates in the presence of halide and H_2O_2. Figure 5.7 A+B show a homogeneous coating of bacteria with

a size of 1-1.5 µm (Figure S5.6) on an uncoated polycarbonate substrate. Due to non-interrupted communication (QS) between the bacteria, they were able to generate an extracellular polymeric substance (EPS) matrix, subsequently form a confluent biofilm and proliferate. In contrast, Figure 5.7 C shows a single isolated bacterium on the surface of a CeO_2-coated substrate. Here, the bacteria were brought to the surface with the LB medium, but the interrupted QS prevented proliferation and inhibited biofilm formation, because the AHLs used for interbacterial communication were modified and therefore inactivated by the CeO_2 nanozyme in the presence of the halide Br^- and H_2O_2 by oxidative bromination.[22]

Cytotoxicity of CeO_2 nanorods. A cell viability assay was made to determine the ability of cells to maintain a state of survival in the presence of the CeO_2 nanorods. The cytotoxicity of CeO_2 nanorods was examined in HeLa and RAW 264.7 cells using a luminescence cell viability assay. The CeO_2 particles showed no cytotoxicity after 24 hours of incubation, even for concentrations up to 300 µg/mL.

The viability of HeLa cells is constant at 100% after 2 and 24 hours, even at high concentrations (Figure 5.8). Similarly, the viability of RAW 264.7 cells remains constant at 100% with increasing particle concentration. Thus, we have shown that CeO_2 coating is a non-cytotoxic approach to prevent the adhesion of bacteria to a polymer surface.

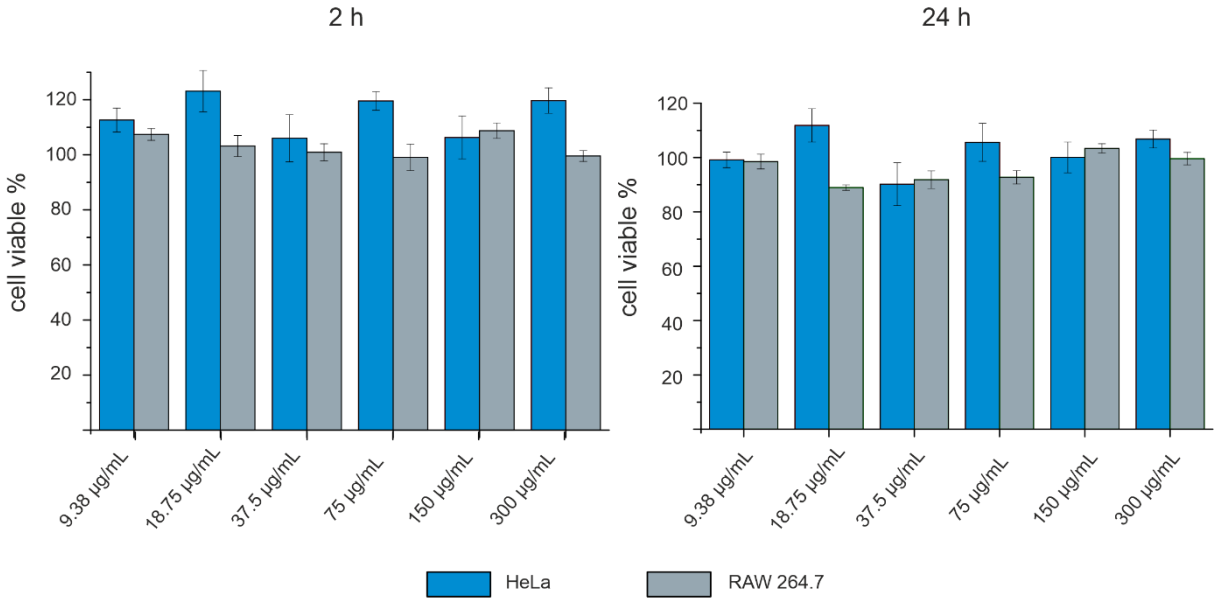

Figure 5.8. Effect of CeO_2-NTA on the cell viability of HeLa and RAW 264.7 cells after 2 h and 24 h at different nanoparticle concentrations.

5.4. Conclusions

We have fabricated highly transparent CeO_2-coated polycarbonate plates with high wettability, and high catalytic haloperoxidase activity to prevent bacterial adhesion. Multigram quantities of highly dispersible CeO_2 nanorods with diameters of 10-15 nm and lengths of 100-200 nm were synthesized from aqueous dispersions of cerium(III) hydroxide by oxidation with hydrogen peroxide in the presence of nitrilotriacetic acid (NTA) as capping agent.

Transparent CeO_2-coated polycarbonate panels were prepared by oxygen plasma treatment of the polycarbonate plates followed by dip coating with CeO_2/NTA dispersions. Low concentrations (as low as 1.6 μg/cm^2, corresponding to a monolayer coating of CeO_2 nanorods, analyzed by atomic force microscopy) were able to reduce *P. aeruginosa* biofilm formation on polycarbonate by at least 75%. Using cytotoxicity assays and live/dead assays, we demonstrated that the cerium oxide coating prevents bacterial adhesion following a non-toxic mode of action. Only very low (milli/micromolar) concentrations of the substrates Br^- and H_2O_2 are required for haloperoxidase-like reactions to occur. These concentrations are comparable to bromide concentrations found in animal and plant body fluids and to H_2O_2 concentrations produced in daylight.[45] This makes CeO_2 nanorods a potent and "green" catalyst for antibacterial applications,[33] since no chemicals are released into the environment other than those that occur anyway in natural metabolic processes of plants. Evidence for quorum quenching and therefore a non-biocidal mode of action was provided by analysis of the QS-dependent virulence factor pyocyanin. Microbial biofilms are ubiquitous on domestic, industrial and other surfaces. Conventional biocides (strong oxidants, antibiotics, etc.) are increasingly problematic due to lack of efficacy, non-targeted environmental effects, or development of resistance by microorganisms.

5.5. Experimental Section

MATERIALS AND SYNTHESIS

Cerium (III) nitrate hexahydrate, nitrilotriacetic acid (99%), and sodium nitrilotriacetate (99+%) were purchased from Acros Organics. Hydrogen peroxide (35%) was purchased from Carl Roth. Ammonium hydroxide solution (25%) was obtained from VWR. All chemicals were used without further purification. Ultrapure water (18.2 MΩ cm-1) was used for all experiments. Polycarbonate (1 mm thickness, 15x15 cm plates) was obtained from GoodFellow.

Synthesis of cerium dioxide nanorods. The synthesis was adapted from ref. 56 and modified for upscaling to multigram amounts of monodisperse CeO_2 nanorods. In two centrifuge tubes, a total 10 g of $Ce(NO_3)_3 \cdot 6H_2O$ were dissolved in 80 mL of H_2O. Subsequently, 8 mL of NH_4OH solution was added. After gentle shaking, the $Ce(OH)_3$ precipitate was centrifuged (3000 rmp, 10 min) to remove excess water. The colorless powder was redispersed in 500 mL of water, preheated to 60 °C under magnetic and Ultra-Turrax® stirring (15000 rpm with S 25 EC-T-C-18G ST homogenizer). After the suspension had turned homogenous 1.4 g NTA and 0.7 g Na_3NTA were added. After further 15 minutes of continuous stirring, the grey-white suspension turned red after adding slowly 3 mL of H_2O_2 (35%). The temperature was slowly to 72°C under ultra-Turrax®-stirring for 45 min. The reaction was allowed to cool to room temperature under magnetic stirring. To remove NH_4NO_3, the suspension was washed three times with H_2O (9000 rmp, 20 min).

Phenol Red Assay. The intrinsic haloperoxidase activity was determined using the phenol red assay. In this assay, tetrabromophenol blue (Br_4PR) is formed *via* reaction of phenol red (PR) in the presence of a bromide source (KBr) and H_2O_2 in the presence of an active catalyst (CeO_2 nanorods). The reaction was monitored using an Agilent Cary 3500 spectrophotometer in the wavelength range of 350 to 700 nm at 25°C. The baseline was measured at constant temperature in a stirred (800 rpm) mixture of CeO_2 nanorods (36.3 µmol), KBr (50 µmol), and PR (0.1 µmol) in 2 mL ultrapure water (18.2 MΩ cm^{-1}) before the addition of H_2O_2 (6 µmol).

Lactone bromination. The degradation of the quorum sensing molecule 3-oxo-C_{12}-HSL by oxidative bromination was followed by time dependent reverse high performance liquid chromatography coupled with electrospray ionisation-mass spectrometry. Several reaction mixtures (1 mL total volume) containing 900 µM 3-Oxo-HL, 20 mM KBr, 20 mM H_2O_2 and CeO_2 nanoparticles (200 µg·mL^{-1}) were analyzed over a period of 5h. The reactions were

terminated by removing the catalyst by centrifugation and the supernatant was analyzed by mass spectrometry

Michaelis Menten Kinetics. For the Michaelis Menten kinetics, the amount of H_2O_2 was varied. The kinetic was performed at λ =592 nm, the absorbance maximum of Br_4PR. For each measurement, the same stock solution of PR (50µM) mixed with KBr (25mM) was used. After the addition of 62.5µL of nanoparticle suspension (1mg/mL), the reaction was left stirring (800 rpm) for 2 min for temperature equilibration (25°C). Prior to H_2O_2 addition the absorbance was set to zero. The kinetics were measured for 10 minutes. All data points were linearly fitted in the period of 2-8 minutes. The concentration was calculated via the Lambert-Beer law. The extinction coefficient was determined by measuring the absorbance of five different Br_4PR solutions (2 µM, 6 µM, 10 µM, 14 µM, 18 µM) in a quartz cuvette (d=1 cm). Using the Lambert-Beer law, an extinction coefficient of 32740 $Lmol^{-1}cm^{-1}$ was determined for BR_4PR (free acid) in ultra-pure water with an Agilent Cary 3500 UV-VIS spectrophotometer.

CeO_2 Coating. Polycarbonate plates (1 mm thickness) with a size of 1x1 cm were washed with MQ water and ethanol to remove surface contamination. To activate the surface, the plates were treated in oxygen plasma for 20 min (290 W, 0.1 mbar). The plasma treated polycarbonate plates were dip-coated in a CeO_2 dispersion (9.5 ± 0.1 mg/mL) in MQ water with a dipping speed of 60 mm/min, held for 60 sec in the dispersion, and pulled out with the same speed. The CeO_2-coated polycarbonate plate was dried in air at 110°C for 16 h. Finally, the plates were washed with MQ water to remove excess CeO_2 from the surface.

Bacterial Strains and Growth Conditions. *P. aeruginosa* PA14 was obtained from the lab of Dr. Max Schobert (Technische Universität Braunschweig, Germany). *P. aeruginosa* was aerobically in LB medium [1% (w/v) NaCl; 1% (w/v) tryptone; 0.5% (w/v) yeast extract] at 30 °C. For preparation of agar plates, 1.5% (w/v) agar was added to the medium.

Biofilm Assays. For quantification of bacterial biofilm production, a modified method of previously published protocols was used.[57] Briefly, *P. aeruginosa* was aerobically in LB medium overnight at 30°C. The cultures were then diluted in LB in a volume of 1 mL per well of a 24-well polystyrene microtiter plate (Sarstedt, Nürnbrecht) at a final Optical Density at 600 nm (OD_{600}) of 0.5. Additionally, KBr (Roth, Karlsruhe, Germany) and H_2O_2 (Roth, Karlsruhe, Germany) at a final concentration of 32 mM and 0.8 mM, respectively, were added to the wells. Then, the blank plates and CeO_2/polycarbonate composites were subjected. Subsequently, the microtiter plate was incubated for 72 h under gentle shaking

(150 rpm) at 30°C. H_2O_2 was added stepwise at a final concentration of 0.8 mM every 24 h. Then, the plates were rinsed with water to remove the planktonic cells. After drying for 5 min, 1 mL of 1% (w/v) crystal violet (Merck, Darmstadt) was added to the wells containing the plates. After 30 min incubation at room temperature, unbound crystal violet was removed by gently submerging the plates two times in water. The plate was then air-dried over-night at room temperature. For quantification, 1 mL of 30% (v/v) acetic acid (Roth, Karlsruhe) was added to the plates to solubilize the crystal violet from the biofilm. After 15 min of incubation at room temperature, absorbance was quantified in a plate reader (Tecan, Salzburg) at 575 nm.

Fluorescence Quantification of Bacterial Biofilm. *P. aeruginosa* was cultivated in LB medium over-night at 30 °C. The cultures were then diluted in LB, in a volume of 1 mL per well of a 24-well polystyrene microtiter plate (Sarstedt, Nürnbrecht) at a final OD_{600} of 0.5. Additionally, KBr (Roth, Karlsruhe, Germany) and H_2O_2 (Roth, Karlsruhe, Germany) at a final concentration of 32 mM and 0.8 mM, respectively, were added to the wells. Next, the non-coated plates and CeO_2/polycarbonate slides were added to the wells. The microtiter plate was incubated for 72 h under gentle shaking (150 rpm) at 30 °C. H_2O_2 was added stepwise at a final concentration of 0.8 mM every 24 h. Then, the plates were rinsed with water to remove the planktonic cells. Subsequently, the plates were placed in 1 mL of a combined SYTO 9 and propidium iodide solution (Thermo Fisher, Pittsburgh, USA) and incubated for 30 minutes at 30 °C. Then, the plates were rinsed again with water and placed inside the well of a 24-well polystyrene microtiter plate. Finally, biofilm fluorescence was then quantified in a plate reader (Tecan, Salzburg) using a wavelength of 485 nm and 535 nm for the fluorophores SYTO 9 and PI, respectively.

Confocal laser scanning microscopy. *P. aeruginosa* was cultivated in LB medium over night at 30 °C. The cultures were then diluted in LB, in a volume of 1 ml per well of a 24-well poly-styrene microtiter plate (Sarstedt, Nürnbrecht) at a final OD_{600} of 0.5. Additionally, KBr (Roth, Karlsruhe, Germany) and H_2O_2 (Roth, Karlsruhe, Germany) at a final concentration of 32 mM and 0.8 mM, respectively, were added to the wells. The non-coated and CeO_2-coated plates were then added to the wells, respectively. The microtiter plate was then incubated for 72 h under gentle shaking (150 rpm) at 30 °C. Every 24 h H_2O_2 was added at a final concentration of 0.8 mM. The plates were then rinsed with water to remove the planktonic cells. Afterwards, the plates were placed in 1 ml of a combined SYTO 9 and propidium iodide 1:1000 dilution (Thermo Fisher, Pittsburgh, USA) and incubated for 30

minutes at 30 °C. The plates were then again rinsed with water and put on microscopy cover slides. The samples were examined on an Axio Imager 2 (Carl Zeiss, Jena, Germany). The fluorophore SYTO 9 was visualized with an excitation of 470 nm while propidium iodide was visualized with an excitation of 558 nm. The images and the biofilm thickness were then processed and quantified using the ZEN 3.3 blue software.

Pyocyanin Analyses. For pyocyanin production, an alternate method of already published protocols was used.[58] For that purpose, *P. aeruginosa* was cultivated in LB medium over night at 30°C. The cultures were then diluted in LB, in a volume of 1 mL per well of a 24-well polystyrene microtiter plate (Sarstedt, Nürnbrecht) at a final OD_{600} of 0.5. Additionally, KBr (Roth, Karlsruhe, Germany) and H_2O_2 (Roth, Karlsruhe, Germany) at a final concentration of 32 mM and 0.8 mM respectively were added to the wells. The non-coated plates and CeO_2/polycarbonate slides were then added to the wells, respectively. The microtiter plate was then incubated for 72 h under shaking conditions (350 rpm) at 37 °C. Every 24 h, H_2O_2 was added stepwise at a final concentration of 0.8 mM. Afterwards, the composites were removed from the wells and the remaining supernatant was collected in a microreaction tube (Eppendorf, Germany). Cells were separated from culture fluids via centrifugation at 16 × 1000 g for 15 min. Then, the supernatant was passed through 0.22 µm filters (Merck, Darmstadt). Finally, the cell-free culture fluids were analyzed for absorption at 695 nm and therefore quantified in a plate reader (Tecan, Salzburg) for pyocyanin.

Cell Culture. RAW 264.7 cells and Human cervix carcinoma cells (HeLa) were cultured in Dulbecco's modified eagle medium (DMEM) supplemented with 10% FBS, 100 U mL^{-1} penicillin, 100 mg mL^{-1} streptomycin and 2 mM glutamine. Cells were grown in a humidified incubator at 37 °C and 5% CO_2. Cell passaging and harvesting were performed using 0,25% Trypsin-EDTA for 5 min at 37°C, 5% CO_2 (all reagents from Thermo Fisher, Germany). Cell viability and cell count were determined by using trypan blue and measuring by an automated cell counter (TC10, Bio-Rad, Germany).

Cell Viability. Cell viability was determined using CellTiter-Glo® Luminescent Assay according to the manufacturer's manual (Promega, USA). After cell harvesting, HeLa or RAW264.7 cells were seeded in 96 well plates (Item No.: 655083, Greiner BioOne, Austria) with a cell number of 5,000 cells per well. Cells were incubated over-night at 37°C and 5% CO_2 to enable cell detachment and afterwards the medium was removed. Nanoparticle solutions were prepared in FBS supplemented DMEM and added to the cells. After incubation for either 2 h or 24 h the same volume of CellTiter-Glo® Reagent was added and

the luminescent signal was measured with an Inifinite M1000 plate reader (Tecan, Switzerland). Cell viability was displayed as the percentage of cell viability compared to untreated cells.

CHARACTERIZATION

Electron Microscopy. Samples for transmission electron microscopy (TEM) were prepared by placing a drop of dilute NP dispersion in ethanol on a carbon-coated copper grid. TEM images were obtained with a FEI Tecnai 12 TWIN LaB6 at 120 kV together with a Gatan US1000 CCD-camera (16-bit, 2048 x 2048 pixels) using the Gatan Digital Micrograph software.

Samples for scanning electron microscopy (SEM) were prepared with carbon film pads on aluminum holders. A silicon wafer was used for the sample preparation and fixed on the carbon pad. A polycarbonate plate was fixed on the carbon pad and sputtered with gold (Thickness 1 nm). SEM images were obtained using a FEI Nova NanoSEM 630 equipped with an EDAX-Pegasus X4M unit for the EDX measurements. The acceleration voltage was set to 5 kV. The elemental composition was calculated using the EDAX Genesis Software Suite.

Powder X-ray Diffraction. X-ray diffraction patterns were recorded on a STOE Stadi P diffractometer equipped with a Dectris My-then 1k detector in transmission mode using Mo Kα1 radiation. Crystalline phases were identified according to the PDF–2 database using Bruker AXS EVA 10.0 software.

Zeta Potentials. Zetapotentials and hydrodynamic radii were measured on a Malvern Zetasizer Nano using disposable capillary cells (DTS1070) and single-use polystyrene cuvettes. Data analysis was performed with Malvern Zetasizer Software 8.01.4906.

BET Surface Area. BET measurements were conducted with 3P Micro 300 gas adsorption instrument using nitrogen as the analysis gas at 77.4 K. The software 3P Surface Area & Pore Size Analyzer System 10.03.02 was used to analyze the recorded data.

Inductively Coupled Plasma Mass Spectrometry (ICPMS). To determine the ceria content of the coated polycarbonate plates, the plates were dissolved in $CHCl_3$, then dried at 45°C and incinerated at 600°C. The ash was dissolved with sub-boiled HNO_3 (65%) and diluted with ultra-pure water and measured with iCAP™ RQ ICP-MS (Thermo Scientific™).

Atomic Force Microscopy. AFM measurements were conducted with an Park Systems NX10, using True Non-Contact™ mode and tapping mode. OMCL-AC160TS cantilever

(k=26 N/m, f≈ 300 kHz) were used to image polycarbonate substrates and CeO_2 coating. For bacteria imaging, SD-R30-FM cantilevers (k=2.8 N/m, f≈ 75 kHz) were applied. The Park Systems XEI Software was used for analysis. All measurements were conducted at ambient conditions.

UV/Vis. UV/Vis measurements were conducted with an Agilent Cary 3500.

Plasma Treatment. The plates were treated with oxygen plasma in a Plasmaprozessor 200G from TePla Technics Plasma GmbH at 0.1 mbar and 290 W for 20 min.

Contact angle Measurements. The contact angle was measured with the contact angle measurement system OCA35 and the water drop was deposited by a Hamilton syringe (100 µL) with a hydrophobic needle.

5.6. References

1. U. Schulz, Kunststoffoptiken mit Antireflex- und Antibeschlageigenschaften durch Plasmaätzen und Beschichtung. *Vak. Forsch. und Prax.* 2014, **26**, 26-31.
2. W. Sun, W. Liu, Z. Wu, H. Chen, Chemical Surface Modification of Polymeric Biomaterials for Biomedical Applications. *Macromol. Rapid Commun.* 2020, **41**, e1900430.
3. F. Theinkom, L. Singer, F. Cieplik, S. Cantzler, H. Weilemann, M. Cantzler, K. A. Hiller, T. Maisch, J. L. Zimmermann, Antibacterial efficacy of cold atmospheric plasma against *Enterococcus faecalis* planktonic cultures and biofilms *in vitro*. *PLoS One* 2019, **14**, e0223925.
4. T. Suryaprabha, M. G. Sethuraman, Fabrication of copper-based superhydrophobic self-cleaning antibacterial coating over cotton fabric. *Cellulose* 2017, **24**, 395-407.
5. D. Druvari, N. D. Koromilas, V. Bekiari, G. Bokias, J. K. Kallitsis, Polymeric Antimicrobial Coatings Based on Quaternary Ammonium Compounds. *Coatings* 2018, **8**, 8.
6. A. Nastulyavichus, S. Kudryashov, N. Smirnov, I. Saraeva, A. Rudenko, E. Tolordava, A. Ionin, Y. Romanova, D. Zayarny, Antibacterial coatings of Se and Si nanoparticles. *Appl. Surf. Sci.* 2019, **469**, 220-225.
7. B. S. Necula, I. Apachitei, F. D. Tichelaar, L. E. Fratila-Apachitei, J. Duszczyk, An electron microscopical study on the growth of TiO_2-Ag antibacterial coatings on Ti6Al7Nb biomedical alloy. *Acta Biomater.* 2011, **7**, 2751-2757.
8. R. André, F. Natalio, M. N. Tahir, W. Tremel, Self-cleaning antimicrobial surfaces by bio-enabled growth of SnO_2 coatings on glass. *Nanoscale* 2013, **5**, 3447-3456.
9. "Toxic lobbying: the titanium dioxide label debate continues," can be found under https://corporateeurope.org/en/2019/06/toxic-lobbying-titanium-dioxide-label-debate-continues, **2019**.
10. Y. C. Ching, T. M. S. U. Gunathilake, K. Y. Ching, C. H. Chuah, V. Sandu, R. Singh, N.-S. Fiou, in *Durab. Life Predict. Biocomposites, Fibre-Reinforced Compos. Hybrid Compos.* (Eds.: M. Jawaid, M. Thariq, N. Saba), Woodhead Publishing, **2019**, pp. 407–426.
11. J. Zhang, W. Guo, Q. Li, Z. Wang, S. Liu, The effects and the potential mechanism of environmental transformation of metal nanoparticles on their toxicity in organisms. *Environ. Sci. Nano* 2018, **5**, 2482-2499.
12. S. Krishnan, C. J. Weinman, C. K. Ober, Advances in polymers for anti-biofouling surfaces. *J. Mater. Chem.* 2008, **18**, 3405-3413.
13. W. Yang, H. S. Sundaram, J. R. Ella, N. He, S. Jiang, Low fouling electrospun PLLA films modified with zwitterionic poly(sulfobetaine methacrylate)-catechol conjugates. *Acta Biomater.* 2016, **40**, 92-99.
14. S. Ozcan, P. Kaner, D. Thomas, P. Cebe, A. Asatekin, Hydrophobic Antifouling Electrospun Mats from Zwitterionic Amphiphilic Copolymers. *ACS Appl. Mater. Interfaces* 2018, **10**, 18300-18309.
15. A. Borghesi, M. Stronati, Strategies for the prevention of hospital-acquired infections in the neonatal intensive care unit. *J. Hosp. Infect.* 2008, **68**, 293-300.
16. S. Mathur, R. Singh, Antibiotic resistance in food lactic acid bacteria--a review. *Int. J. Food Microbiol*. 2005, **105**, 281-295.

17. K. Page, M. Wilson, I. P. Parkin, Antimicrobial surfaces and their potential in reducing the role of the inanimate environment in the incidence of hospital-acquired infections. *J. Mater. Chem.* 2009, **19,** 3818-3831.

18. J. B. Kristensen, R. L. Meyer, B. S. Laursen, S. Shipovskov, F. Besenbacher, C. H. Poulsen, Antifouling enzymes and the biochemistry of marine settlement. *Biotechnol. Adv.* 2008, **26**, 471-481.

19. M. Sandy, J. N. Carter-Franklin, J. D. Martin, A. Butler, Vanadiumbromoperoxidase from *Delisea pulchra*: enzyme-catalyzed formation of bromofuranone and attendant disruption of quorum sensing. *Chem. Commun.* 2011, **47**, 12086-12088.

20. M. B. Miller, B. L. Bassler, Quorum sensing in bacteria. *Annu. Rev. Microbiol.* 2001, **55**, 165-199.

21. K. Herget, P. Hubach, S. Pusch, P. Deglmann, H. Götz, T. E. Gorelik, I.A. Gural'skiy, F. Pfitzner, T. Link, S. Schenk, M. Panthöfer, V. Ksenofontov, U. Kolb, T. Opatz, R. André, W. Tremel, Haloperoxidase Mimicry by CeO_{2-x} Nanorods Combats Biofouling. *Adv. Mater.* 2017, **29**, 1603823.

22. B. Sels, D. De Vos, M. Buntinx, F. Plerard, A. Kirsch-De Mesmaeker, P. Jacobs, Layered double hydroxides exchanged with tungstate as biomimetic catalysts for mild oxidative bromination**.** *Nature* 1999, **400**, 855-857.

23. V. Conte, B. Floris, Vanadium and molybdenum peroxides: synthesis and catalytic activity in oxidation reactions. *Dalton Trans.* 2011, **40**, 1419-1436.

24. R. Wever, M. A. van der Horst, The role of vanadium haloperoxidases in the formation of volatile brominated compounds and their impact on the environment. *Dalton Trans.* 2013, **42**, 11778-11786.

25. F. Natalio, R. André, A. F. Hartog, B. Stoll, K. P. Jochum, R. Wever, W. Tremel, Vanadium pentoxide nanoparticles mimic vanadium haloperoxidases and thwart biofilm formation. *Nature Nanotechnol*. 2012, **7**, 530-535.

26. L. Wang, J. Hou, S. Liu, A. J. Carrier, T. Guo,Q. Liang, D. Oakley, X. Zhang, CuO nanoparticles as haloperoxidase mimics: Chloride-accelerated heterogeneous Cu-Fenton chemistry for H_2O_2 and glucose sensing. *Sens. Actuators B Chem.* 2019, **287**, 180-184.

27. A. Filippi, F. Liu, J. Wilson, S. Lelieveld, K. Korschelt, T. Wang, T. Reich, Y. Wang, U. Pöschl, W. Tremel, H. Tong, Antioxidant activity of cerium dioxide nanoparticles and nanorods in scavenging hydroxyl radicals. *RSC Adv*. **2019**, 9, 11077–11081.

28. H. Wei, E. Wang, Nanomaterials with enzyme-like characteristics (nanozymes): next-generation artificial enzymes. *Chem. Soc. Rev.* 2013, **42**, 6060-6093.

29. K. Korschelt, M. N. Tahir, W. Tremel, A Step into the Future: Applications of Nanoparticle Enzyme Mimics. *Chem.Eur. J.* 2018, **24**, 9703-9713.

30. C. K. Kim, T. Kim, I.-Y. Choi, M. Soh, D. Kim, Y.-J. Kim, H. Jang, H.-S. Yang, J. Y. Kim, K.-K. Park, S. P. Park, S. Park, T. Yu, B. W. Yoon, S.-H. Lee, T. Hyeon, Ceria Nanoparticles that can Protect against Ischemic Stroke. *Angew. Chem. Int. Ed.* 2012, **51**, 11039 –11043.

31. T. V. Plakhova, A. Y. Romanchuk, S. N. Yakunin, T. Dumas, S. Demir, S. Wang, S. G. Minasian, D. K. Shuh, T. Tyliszczak, A. A. Shiryaev, A. V. Egorov, V. K. Ivanov, S. N. Kalmykov, Solubility of Nanocrystalline Cerium Dioxide: Experimental Data and

Thermodynamic Modeling. *J. Phys. Chem. C* 2016, **120**, 22615-22626.

32. N. N. Greenwood, A. Earnshaw, *Chemistry of the Elements*, 2nd ed., Elsevier Science, 2012.

33. K. Herget, H. Frerichs, F. Pfitzner, M. N. Tahir, W. Tremel, Functional Enzyme Mimics for Oxidative Halogenation Reactions that Combat Biofilm Formation. *Adv. Mater.* 2018, **30**, 1707073.

34. A. Qureshi, S. Shah, S. Pelagade, N. L. Singh, S. Mukherjee, A. Tripathi, U. P. Despande, T. Shripathi, Surface modification of polycarbonate by plasma treatment. *J. Phys. Conf. Ser.* 2010, **208**, 012108.

35. H. Yaghoubi, N. Taghavinia, E. K. Alamdari, Self cleaning TiO_2 coating on polycarbonate: Surface treatment, photocatalytic and nanomechanical properties. *Surf. Coatings Technol.* 2010, **204**, 1562-1568.

36. R. M. Thurston, J. D. Clay, M. D. Schulte, Effect of Atmospheric Plasma Treatment On Polymer Surface Energy and Adhesion. *J. Plast. Film Sheeting* 2007, **23,** 63-78.

37. M. Lorenzetti, I. Dogša, T. Stošicki, D. Stopar, M. Kalin, S. Kobe, S. Novak, The Influence of Surface Modification on Bacterial Adhesion toTitanium-Based Substrates. *ACS Appl. Mater. Interfaces.* 2015, **7**, 1644–1651.

38. G. Balakrishnan, S. Tripura Sundari, P. Kuppusamia, P. Chandra Mohan, M.P. Srinivasan, E. Mohandas, V. Ganesan, D. Sastikumar, A study of microstructural and optical properties of nanocrystalline ceria thin films prepared by pulsed laser deposition. Thin Solid Films 2011, **519**, 2520-2526.

39. H. A. Miran, Z.-T. Jiang, M. Altarawneh, J.-P. Veder, Z.-F. Zhou, M. M. Rahman, Z. N. Jaf, B. Z. Dlugogorski, Influence of DC magnetron sputtering reaction gas on structural and optical characteristics of Ce-oxide thin films. *Ceram. Int.* 2018, **44**, 16450-16458.

40. I. Z. Dubé, J. M. García Rangel, J. Roque, I. C. Romero-Ibarra, M. F. García Sánchez, Strong texture tuning along different crystalline directions in glass-supported CeO_2 thin films by ultrasonic spray pyrolysis. Sci. Rep. 2021, **11**, 2006.

41. R. Lo Nigro, G. Malandrino, I. L. Fragalà, Metal−Organic Chemical Vapor Deposition of CeO_2 〈100〉 Oriented Films on No-Rolled Hastelloy C276. *Chem. Mater.* 2001, **13**, 4402–4404.

42. M. Dronova, V. Lair, P. Vermaut, A. Ringuedé, V. An, Study of ceria thin films prepared via electrochemical deposition: Role of selected electrochemical parameters on growth kinetics. *Thin Solid Films* 2020, **693**, 137674.

43. X. Yuan, P. S. Nico, X. Huang, T. Liu, C. Ulrich, K. H. Williams, J. A. Davis, Production of Hydrogen Peroxide in Groundwater at Rifle, Colorado. *Environ. Sci. Technol.* 2017, **51**, 7881–7891.

44. H. Sakugawa, I. R.Kaplan, W. Tsai, Y. Cohen, Atmospheric hydrogen peroxide. *Environ. Sci. Technol.* 1990, **24**, 1452–1462.

45. W. J. Cooper, R. G. Zlka, R. G.Petasne, J. M. C. Plane. Photochemical Formation of H_2O_2 in Natural Waters Exposed to Sunlight. *Environ. Sci. Technol.* 1988, **22**, 1156–1160.

46. E. J. Salazar-Sandoval, M. K. G. Johansson, A. Ahniyaz, Aminopolycarboxylic acids as a versatile tool to stabilize ceria nanoparticles – a fundamental model experimentally demonstrated *RSC Adv.* 2014, **4**, 9048-9055.

47. S. Goutelle, M. Maurin, F. Rougier, X. Barbaut, L. Bourguignon, M. Ducher, P. Maire, The

Hill equation: a review of its capabilities in pharmacological modelling. *Fundam. Clin. Pharmacol.* 2008, **22**, 633-648.

48. S. Kozuch, J. M. L. Martin, "Turning Over" Definitions in Catalytic Cycles. *ACS Catal.* 2012, **2**, 2787-2794.

49. A. Hofrichter, P. Bulkin, B. Drévillon, Plasma treatment of polycarbonate for improved adhesion. *J. Vac. Sci. Technol. A* 2002, **20**, 245.

50. U. Schubert, Polymers Reinforced by Covalently Bonded Inorganic Clusters. *Chem. Mater.* 2001, **13**, 3487–3494.

51. U. Schubert, Neue Materialien. Wo sich Materialwissenschaften und Chemie treffen.. *Chem. Unserer Zeit* 2021, **55**, 14–24.

52. J. Dagata, P. Kavuri, A. Vladar, K. Ehara, N. Farkas, C.-L. Wu, H. Itoh, Method for measuring the diameter of polystyrene latex reference spheres by atomic force microscopy. *Natl. Inst. Stand. Technol.* 2016, 1-26.

53. C. J. Boehlert, J. D. Farr, R. K. Schulze, R. A. Pereyra, J. A. Archuleta, Initial electron back-scattered diffraction observations of cerium. *Philos. Mag.* 2003, **83**, 1735-1744.

54. M. Exner, W. Nissing, K. Behringer, S. Engelhart, S. Pleischl, C. Koch, M. Trautmann, A. Kramer, P. Walger, H. Martiny, L. Jatzwauk, Bedeutung von Wasser und gramnegativen Keimen in der Hygiene. *Hyg Med* 2016, **41**, 3-32.

55. Y. Deng, L. Wang, Y. Chen, Y. Long, Optimization of staining with SYTO 9/propidium iodide: interplay, kinetics and impact on *Brevibacillus brevis. Biotechniques* 2020, **69**, 89-98.

56. W. J. Cooper, R. G. Zika, R. G. Petasne, J. M. C. Plane, Photochemical formation of hydrogen peroxide in natural waters exposed to sunlight. *Environ. Sci. Technol.* 1988, **22**, 1156-1160.

56. M. Aguirre, E. Johansson Salazar-Sandoval, M. Johansson, A. Ahniyaz, M. Paulis, J. R. Leiza, Hybrid acrylic/CeO_2 nanocomposites using hydrophilic, spherical and high aspect ratio CeO_2 nanoparticles. *J. Mater. Chem. A* 2014, **2**, 20280-20287.

57. G. A. O'Toole, Microtiter dish biofilm formation assay. *J. Vis. Exp.* 2010, **10**, 2437.

58. C. T. O'Loughlin, L. C. Miller, A. Siryaporn, K. Drescher, M. F. Semmelhack, B. L. Bassler, A quorum-sensing inhibitor blocks Pseudomonas aeruginosa virulence and biofilm formation. *Proc. Natl. Acad. Sci. U. S. A.* 2013, **110**, 17981-17986.

5.7. Supporting Information

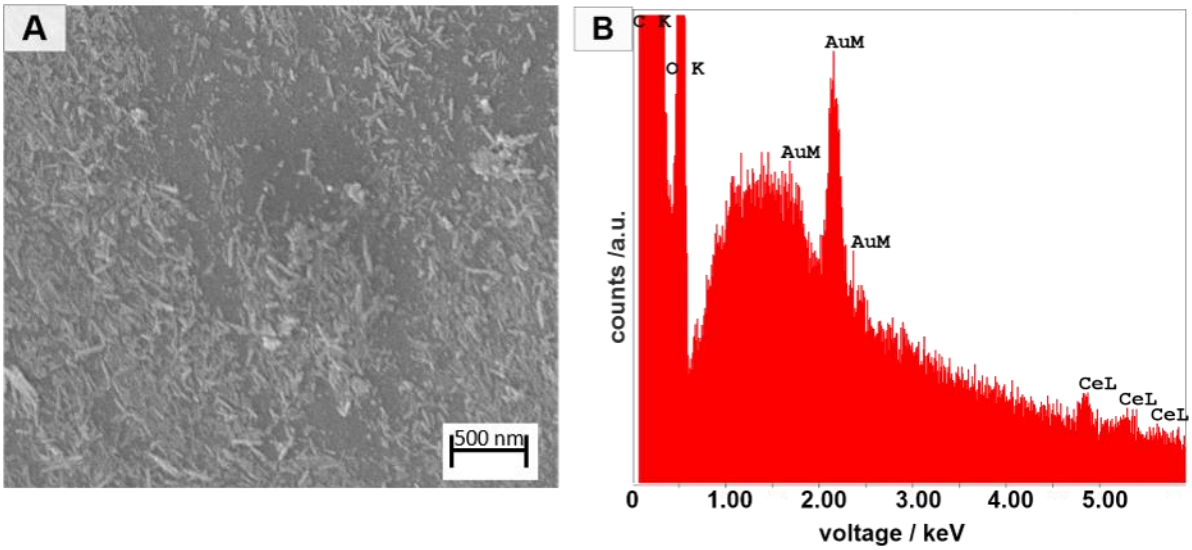

Figure S 5.1. Scanning electron microscope (SEM) image (A) and energy-dispersive X-ray (EDX) spectrum (B) of a CeO_2 coated polycarbonate surface.

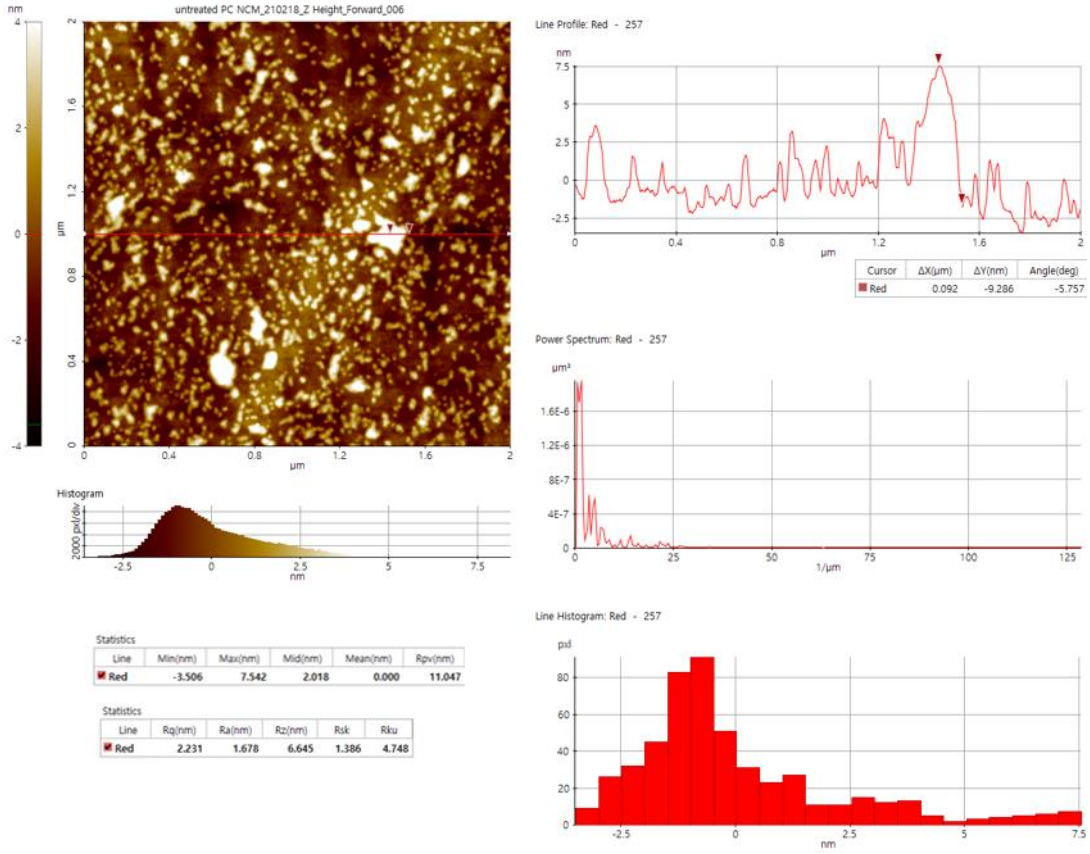

Figure S 5.2. AFM analysis of a non-coated polycarbonate plate.

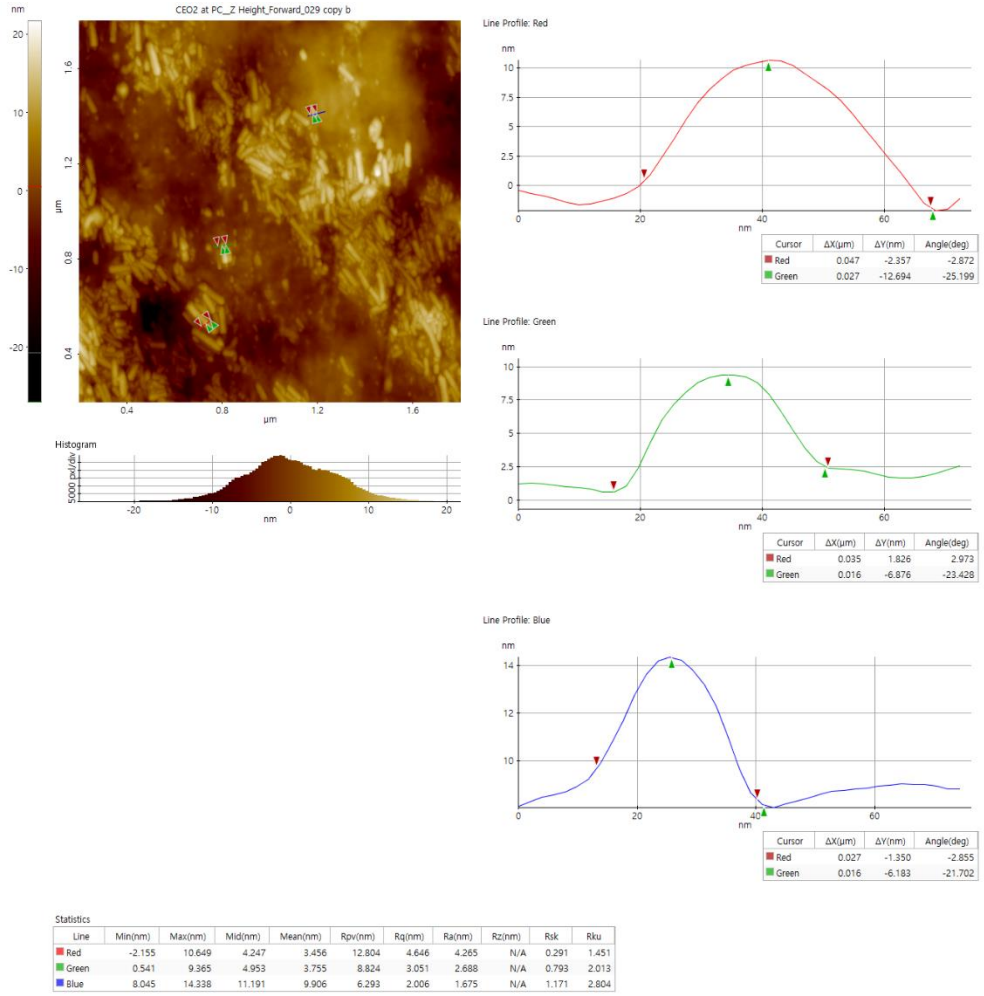

Statistics

Line	Min(nm)	Max(nm)	Mid(nm)	Mean(nm)	Rpv(nm)	Rq(nm)	Ra(nm)	Rz(nm)	Rsk	Rku
Red	-2.155	10.649	4.247	3.456	12.804	4.646	4.265	N/A	0.291	1.451
Green	0.541	9.365	4.953	3.755	8.824	3.051	2.688	N/A	0.793	2.013
Blue	8.045	14.338	11.191	9.906	6.293	2.006	1.675	N/A	1.171	2.804

Figure S 5.3. AFM analysis of a CeO_2-coated polycarbonate plate.

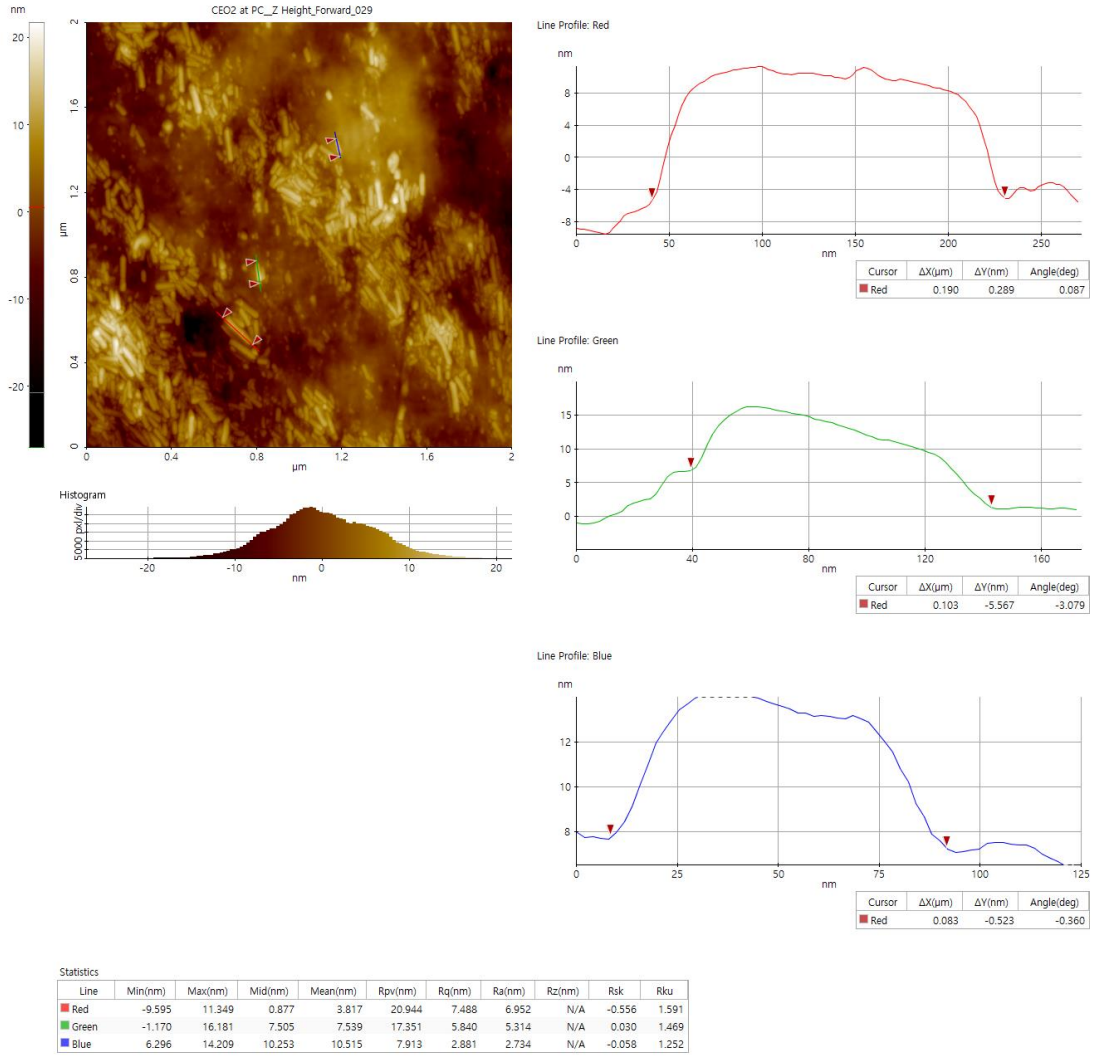

Statistics

Line	Min(nm)	Max(nm)	Mid(nm)	Mean(nm)	Rpv(nm)	Rq(nm)	Ra(nm)	Rz(nm)	Rsk	Rku
Red	-9.595	11.349	0.877	3.817	20.944	7.488	6.952	N/A	-0.556	1.591
Green	-1.170	16.181	7.505	7.539	17.351	5.840	5.314	N/A	0.030	1.469
Blue	6.296	14.209	10.253	10.515	7.913	2.881	2.734	N/A	-0.058	1.252

Figure S 5.4. AFM nanoparticle size analysis of a CeO_2-coated polycarbonate plate.

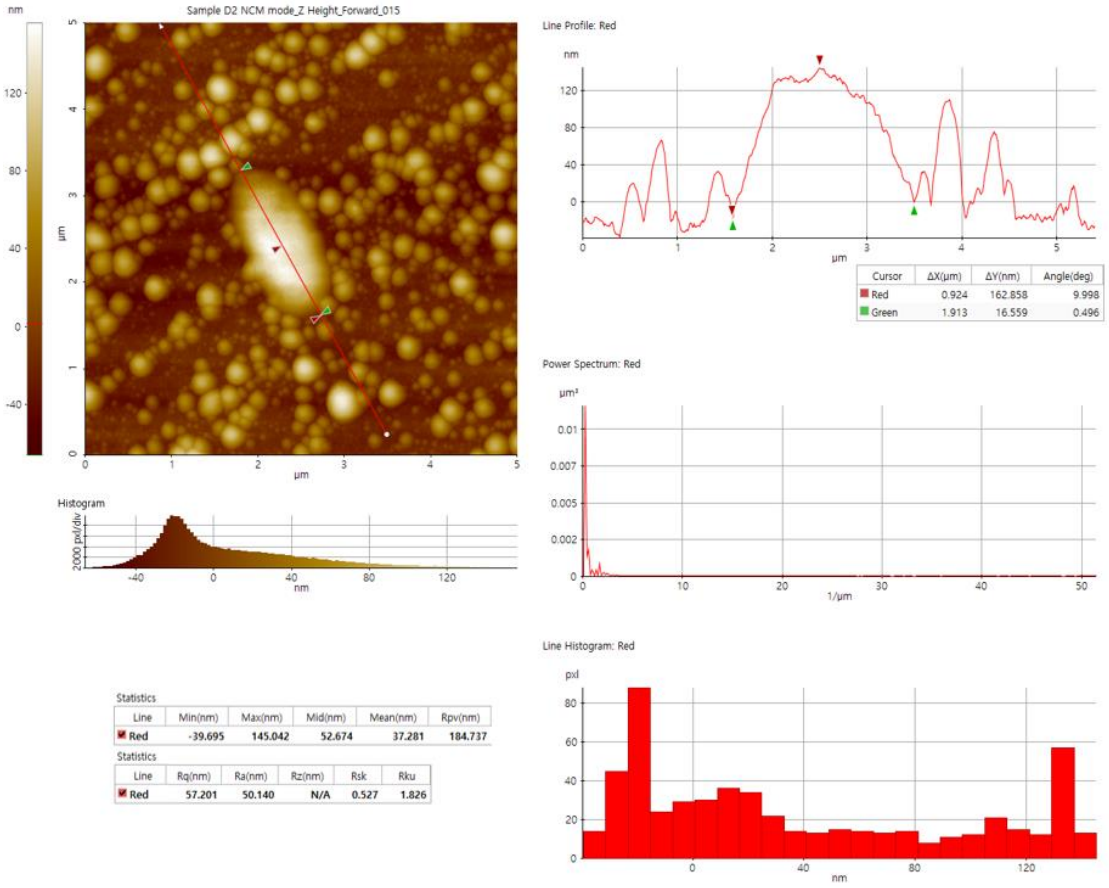

Figure S 5.5. AFM analysis of a CeO_2-coated polycarbonate plate with *P. aeruginosa*.

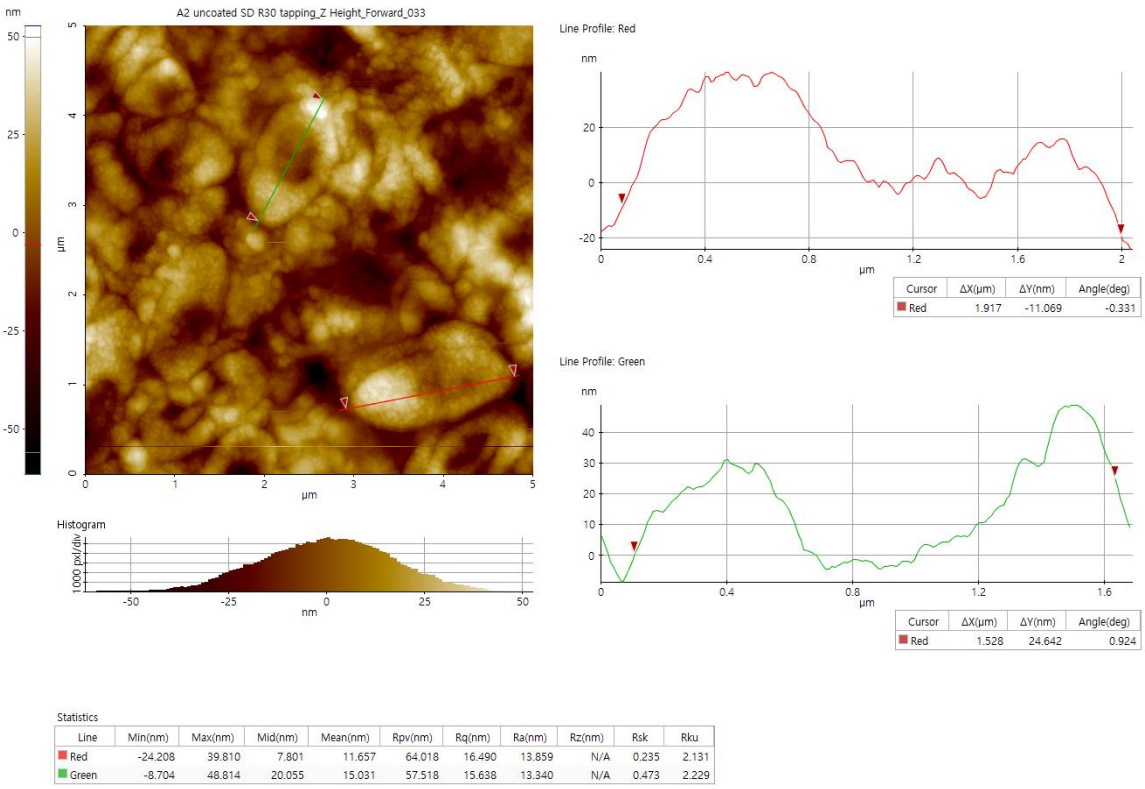

Statistics

Line	Min(nm)	Max(nm)	Mid(nm)	Mean(nm)	Rpv(nm)	Rq(nm)	Ra(nm)	Rz(nm)	Rsk	Rku
Red	-24.208	39.810	7.801	11.657	64.018	16.490	13.859	N/A	0.235	2.131
Green	-8.704	48.814	20.055	15.031	57.518	15.638	13.340	N/A	0.473	2.229

Figure S 5.6. AFM analysis of a non-coated polycarbonate plate with a P. aeruginosa biofilm.

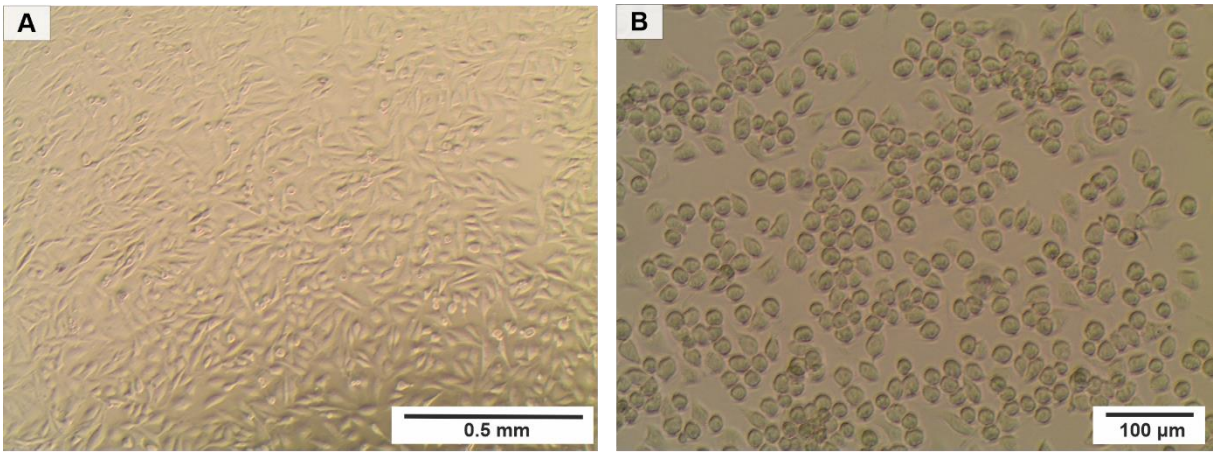

Figure S 5.7. Optical microscopy image of HeLa (A) and RAW (B) cells on the surface of a CeO_2 coated polycarbonate plate.

Figure S 5.8. Aqueous suspension of NTA-functionalized CeO_2 nanorods.

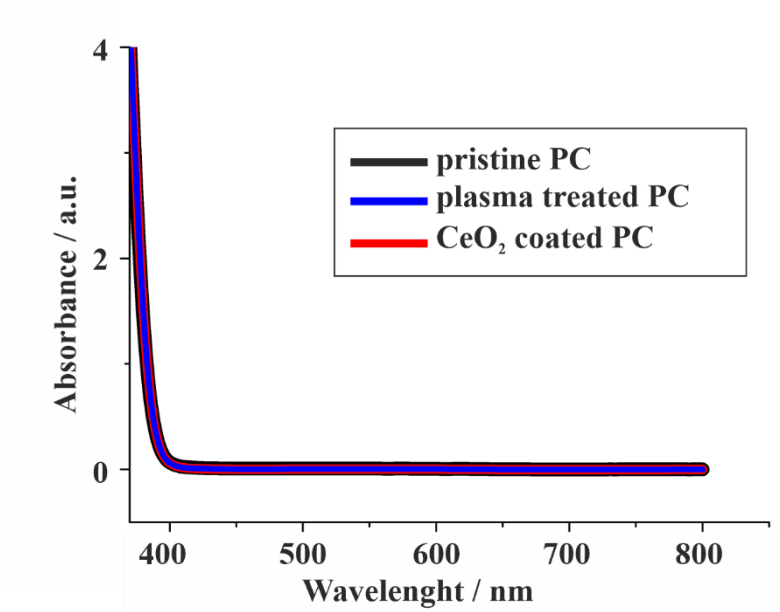

Figure S 5.9. UV/Vis spectra of pristine, plasma-treated and CeO_2-coated polycarbonate plates.

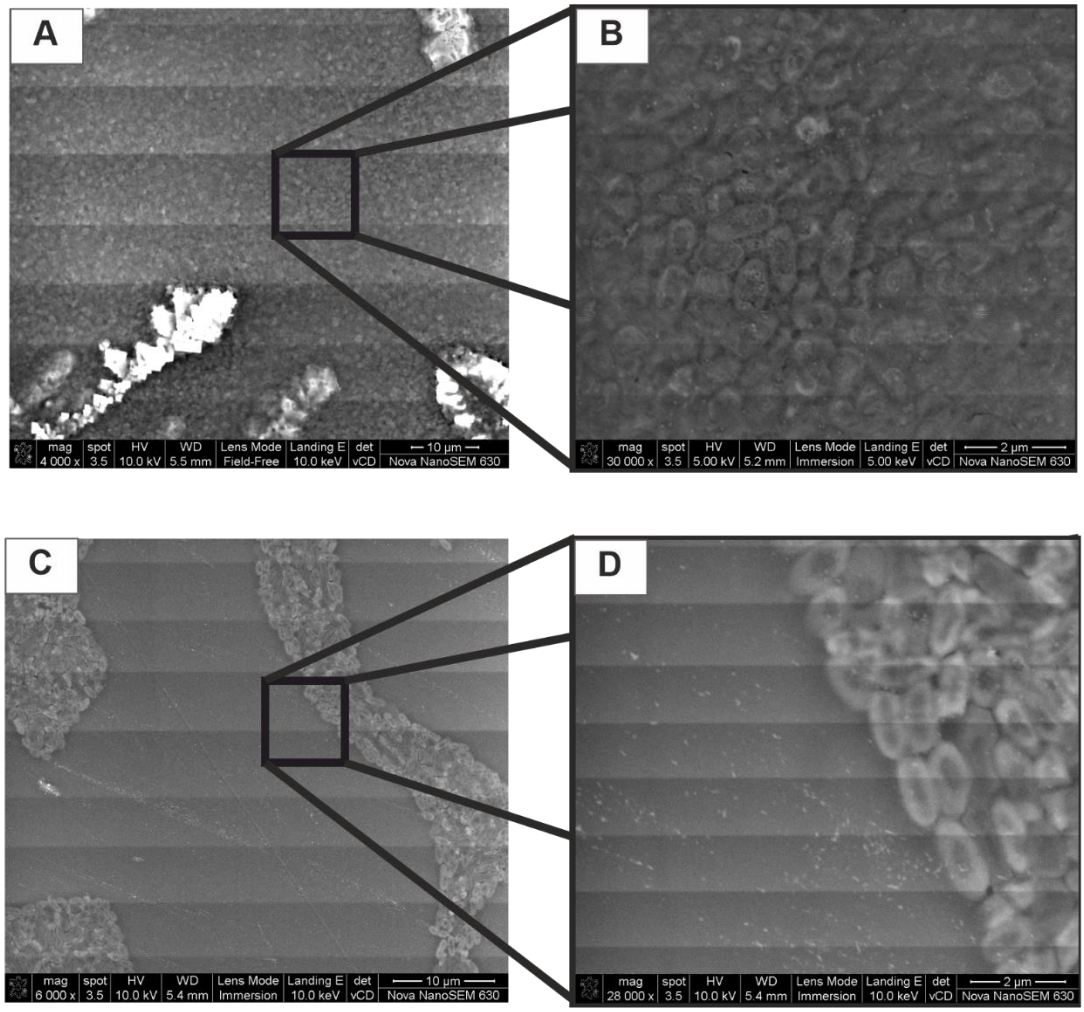

Figure S 5.10. Scanning electron microscope (SEM) images of P. aeruginosa PA14 biofilms on a+b) non coated and c+d) with CeO_2-coated polycarbonate.

Bromination of the quorum sensing signaling molecule *N*-(3-Oxododecanoyl)-L-homoserine lactone of *P. aeruginosa*:

N-(3-Oxododecanoyl)-L-homoserine lactone (3-oxo-C12-HSL) is a quorum sensing signaling molecule of *P. aeruginosa*. To confirm the hypothesis of oxidative bromination of the signal molecule, a reaction mixture was mixed with 3-oxo-C12-HSL (0.012 mmol), KBr (0.024 mmol), CeO_2 nanoparticles (2 mg) and H_2O_2 35% (16 µL) in methanol and was stirred for an hour.

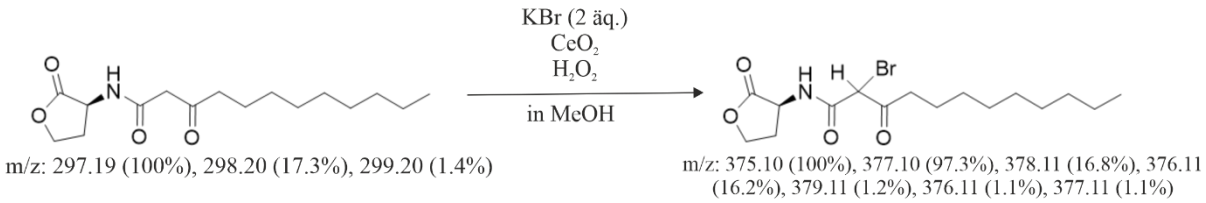

m/z: 297.19 (100%), 298.20 (17.3%), 299.20 (1.4%)

m/z: 375.10 (100%), 377.10 (97.3%), 378.11 (16.8%), 376.11 (16.2%), 379.11 (1.2%), 376.11 (1.1%), 377.11 (1.1%)

The reaction mixture was placed on a thin layer chromatography (TLC) plate and was put in a glass beaker with the eluent ethyl acetate:cyclohexane (5:1). The spots were examined by mass spectrometry (TLC MS). The results from the mass spectra are displayed in Figure S5.11.

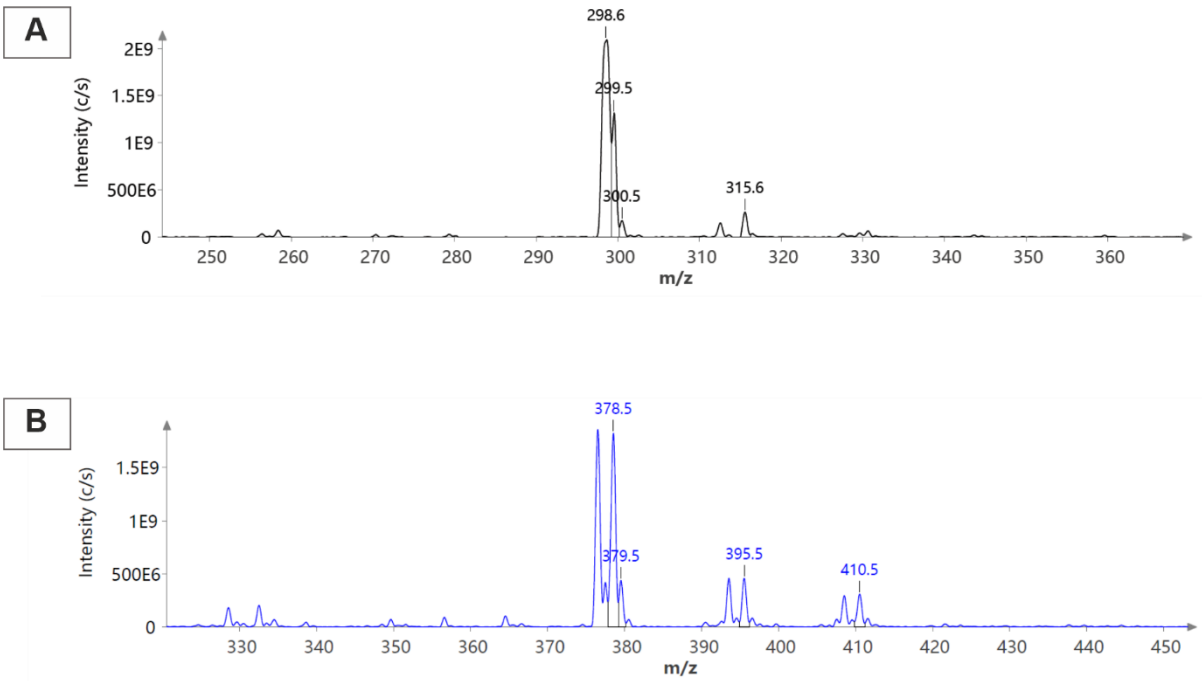

Figure S 5.11. Positive-ionization mode mass spectra of a) 3-oxo-C12-HSL and b) monobrominated 3-oxo-C12-HSL.

6 Conclusions

The scientific goal of this work was to identify which characteristics of CeO_2 nanoparticles influence and improve the catalytic activity as a haloperoxidase mimetic. Subsequently, a composite of the polymer polycarbonate and CeO_2 nanoparticles was prepared.

To view which factors influence the catalytic activity of CeO_2 nanoparticles, different morphologies of the nanoparticles were synthesized: nanorods, nanospheres and nanocubes. The catalytic activity with respect to oxidative bromination of thymol (2-isopropyl-5-methylphenol) was investigated using ^{1}H-NMR spectroscopy. It has been revealed that for different morphologies, the surface are of the particles differs in the factors such as BET surface area, ζ-potential, Lewis acidity and defect density. The highest catalytic rate was obtained for nanorods and the lowest for nanocubes. It was demonstrated that the highest possible BET surface area, high positive ζ-potential, and the most possible acidic surface area promoted oxidative bromination. Also, it was observed that defect density plays an important role in catalysis: a higher ratio of Ce^{3+}-ratio in CeO_2 increase the catalysis rate.

The second project investigated how the catalytic rate of the CeO_2 nanoparticles can be increased. For this purpose, the nanoparticles were doped with the lanthanide terbium (Tb) and praseodymium (Pr) by a mechanochemical synthesis, and the rate of the oxidative bromination was determined through a haloperoxidase assay. It was concluded when doping with terbium, the catalytic rate was doubled, and when doped with praseodymium, the catalytic rate was increased by a factor of 3.5. Here as well, BET surface area and ζ-potential were investigated in more detail, and it was evident that the maximum possible BET surface area and the most positive ζ-potential increase the catalytic activity. A difference between the carbonate vibration modes by FTIR measurements of the doped and undoped CeO_2 nanoparticles was obtained. In doped nanoparticles, the intensity of chemisorbed CO_2 was lower than in undoped ones, suggesting that less chemisorbed CO_2 on the surface, the more positive the ζ-potential becomes. Additionally, ESR spectroscopy showed an increase in the number of paramagnetic defects induced by doping. The presence of Pr^{3+} and Tb^{3+} during the synthesis promoted the formation of Ce^{3+} and O_2^- defects at the CeO_2 nanocrystal surface.

In the last project, a composite of polycarbonate and CeO_2 nanoparticles was prepared and its surface was subsequently tested for biofilm inhibition in presence of H_2O_2 and the halide

Br^-. First, well dispersible CeO_2 nanoparticles were prepared in aqueous solution. For this process, the particles were functionalized with the ligand NTA (nitrilotriacetic acid). Since the surface of polycarbonate is very hydrophobic and the wetting of the surface was therefore problematic, it was treated with oxygen plasma to increase the hydrophilicity. The polycarbonate plates were coated using a dip-coating process. The benefit of this technique was that only 1.6 µg/cm² of nanoparticles were needed for coating the surface to produce a high inhibitory effect against bacterial growth. The coated surface was tested for biofilm growth formation. Therefore, the biofilm on the coated and uncoated polycarbonate plates was measured by crystal violet staining assay. It was revealed that CeO_2 nanoparticles on the surface reduced biofilm formation by 75%. It was also shown that CeO_2 has no biocidal effect. AFM and SEM images of the bacterial film of uncoated and coated polycarbonate plates were obtained, which also demonstrated a clear difference in biofilm growth.

In summary, it was presented that CeO_2 is potentially able to inhibit biofilm formation in the presence of H_2O_2 and Br^- and which factors need to be considered to reach the maximum catalytic rate of oxidative bromination.

7 Appendix

7.1. List of Figures

7.2. List of Tables

7.3.List of Abbreviations

AHL	Acylated homoserine lactone
AI	Autoinducer
a.u.	Arbitrary unit
β	Mass concentration
B	Magnetic field
B.E.	Binding energy
BET	Brunauer-Emmet-Teller method for surface analysis
Br_4PR	Bromphenol blue
c	Concentration
C_{max}	Critical concentration
C_{min}	Minimum concentration
COSY	Homonuclear correlation spectroscopy
C_S	Saturation concentration
Δ	Chemical shift
DNA	Deoxyribonucleis acid
E_0	Potential
EDX	Energy dispersive X-ray
EPS	Extracellular polymeric substances
ESR	Electron Spin Resonance
EU	Europe
FFT	Fourier transform
FTIR	Fourier-transform infrared
g	Landé Faktor
ΔG°	Gibbs energy change
HOX	Hypohalous acid
HRTEM	High resolution transmission electron microscopy
ICPMS	Inductively cpouple plasma mass spectroscopy
J	Number of returns/Coupling constant
k_a	Rate constant of a
K_m	Michaelis constant
λ	Wavelenght
λ_{max}	Absorption maximum

LMCT	Ligand to metal charge transfer
Ln	Lanthanoide
n	Cooperative effect
NMR	Nuclear Magnetic Resonance
NTA	Nitrilotriacetic acid
PC	Polycarbonate
PR	Phenolred
PXRD	Powder X-ray diffraction
Q	Scattering vector
QQ	Quorum quenching
QS	Quorum sensing
ROR	Rate of reaction
ROS	Reactive oxygen species
RT	Room temperature
RV	Rietveld
[S]	Concentration of substrate
S_{BET}	BET surface area
SEM	Scanning electron microscopy
SOFC	Solid oxide fuel cells
TBT	Tributyltin
TEM	Transmission electron microscopy
THMF	Tetrahydroxytetrahydrofurane
TLC	Thin layer chromotography
TMP	Trimethylphosphine
TOF	Turn over frequency
TWC	Three way catalyst
V-BPO	Vanadium-bromoperoxidase
V-CPO	Vanadium-chloroperoxidase
V-HPO	Vanadium-haloperoxidase
V-IPO	Vanadium-iodoperoxidase
v_{max}	Maximum rate
% v/v	Volume percent
w/v	Weight per volume

υ	Vibration mode
XPS	X-ray photoelectron spectroscopy